UNIVERSITÉ DU QUÉBEC

MÉMOIRE PRÉSENTÉ À
L'UNIVERSITÉ DU QUÉBEC À CHICOUTIMI
COMME EXIGENCE PARTIELLE
DE LA MAÎTRISE EN INGÉNIERIE

PAR

MEHRAN MATBOU RIAHI

NUMERICAL AND EXPERIMENTAL STUDIES OF THE MECHANICAL BEHAVIOUR AT THE ICE / ALUMINIUM INTERFACE

ÉTUDES NUMÉRIQUE ET EXPÉRIMENTALE DU COMPORTEMENT MÉCANIQUE À L'INTERFACE GLACE / ALUMINIUM

FÉVRIER 2007

Bibliothèque Paul-Émile-Boulet

UQAC Université du Québec à Chicoutimi

Mise en garde/Advice

Afin de rendre accessible au plus grand nombre le résultat des travaux de recherche menés par ses étudiants gradués et dans l'esprit des règles qui régissent le dépôt et la diffusion des mémoires et thèses produits dans cette Institution, **l'Université du Québec à Chicoutimi (UQAC)** est fière de rendre accessible une version complète et gratuite de cette œuvre.

Motivated by a desire to make the results of its graduate students' research accessible to all, and in accordance with the rules governing the acceptation and diffusion of dissertations and theses in this Institution, the **Université du Québec à Chicoutimi (UQAC)** is proud to make a complete version of this work available at no cost to the reader.

L'auteur conserve néanmoins la propriété du droit d'auteur qui protège ce mémoire ou cette thèse. Ni le mémoire ou la thèse ni des extraits substantiels de ceux-ci ne peuvent être imprimés ou autrement reproduits sans son autorisation.

The author retains ownership of the copyright of this dissertation or thesis. Neither the dissertation or thesis, nor substantial extracts from it, may be printed or otherwise reproduced without the author's permission.

Dedicated with love to all of my family.

Abstract

The presence of ice on mechanical structures generally causes many serious problems. In recent years, several fatal aircraft accidents have been caused by the accumulation of ice on aircraft wings and helicopter blades. In northern regions, ice accumulation on power lines often causes breakage and loss of power during the winter months. In the context of eliminating the problems of ice formation on structural components, an understanding of the mechanical properties of ice-substrate interfaces is essential in order to develop de-icing techniques.

The proposed approach consists of developing a numerical tool that predicts the de-icing of mechanical structures from which certain parameters characteristic of the material of ice-substrate interface are defined based on experimental results. In this research, de-icing of ice on an aluminium plate under the tension of the aforementioned plate was examined. This experiment shows that the energy induced in the composite system (ice-aluminium) at high strain rate ($10^{-3}s^{-1}$) has appeared by the de-icing (ice removal) or by the cracking of the ice (ice fracture), according to the thickness of ice coated on the plate at a temperature of -10°C.

Then, a numerical model was developed using ABAQUS software in order to simulate the experimental test adequately. The aluminium plate is considered elastic to take into account the potential presence of geometrical non-linearity. The constitutive law for ice is considered similar to classic concrete. Accordingly, a «brittle cracking» constitutive law is proved to be a judicious choice. The required parameters of this law were fixed based on the tensile test of an ice sample. The interface, as its name implies, was modeled using the cohesive material constitutive law. The required parameters of this law, which predicts the initiation as well as evolution of damage to the interface, were fixed on the performed tensile test. Results from the numerical simulations make it possible to accurately corroborate the de-icing of ice/aluminium specimens studied in laboratory.

Résumé

La présence de glace sur les structures mécaniques sont généralement à l'origine de nombreux problèmes récurrents. L'accumulation de glace sur les ailes d'un avion ou sur les pales d'hélicoptère, sont, chaque année, à l'origine de nombreux accidents mortels. Dans les régions nordiques, la surcharge occasionnée par la présense de glace sur les lignes de transport provoque des pannes de courant de longues durées durant les périodes froides. Dans ce contexte, il devient essentiel d'établir une meilleure compréhension du comportement à l'interface glace-substrat et ce, afin d'améliorer les techniques de dégivrage et de déglaçage des structures mécaniques.

L'approche proposée consiste à développer un outil numérique prédictif du déglaçage des structures mécaniques dont certains paramètres caractéristiques des matériaux en cause et de l'interface glace-substrat auront été calés sur des résultats expérimentaux. Dans cette étude, le déglaçage d'une lamelle en aluminium par la mise en tension de cette dernière a été examiné. Entre autres, ces résultats expérimentaux ont démontré que l'énergie induite dans le système composite (aluminium-glace) à haut taux de déformation (10^{-3} s^{-1}) se traduit soit par le déglaçage ou encore par la fissuration de la glace et ce, en fonction de l'épaisseur de glace produite sur la lamelle à une température de -10°C.

Parallèlement, un modèle numérique a été développé à l'aide du logiciel ABAQUS afin de simuler adéquatement l'essai expérimental. La lamelle d'aluminium est considérée élastique tout en prenant en compte la présence potentielle des non-linéarités géométriques. La loi de comportement de la glace est considérée similaire à celle d'un béton classique. Dans cette optique, une loi de comportement du type « brittle cracking » s'est avéré un choix judicieux. Les paramètres de cette loi ont été calés sur un essai de traction sur un échantillon de glace. L'interface, quant à elle, a été modélisée à l'aide d'une loi d'adhésion. Les paramètres de cette loi qui permettent, entre autres, la prédiction du début ainsi que de l'évolution de l'endommagement à l'interface, ont été calés sur l'essai de traction réalisé. Les résultats numériques obtenus permettent de corroborer fidèlement le déglaçage de la lamelle étudiée en laboratoire.

Acknowledgments

First of all, I would like to express my deepest sense of gratitude to my director of studies, Prof. D. Marceau, for being an excellent advisor. His patient guidance, support, encouragement and invaluable advice made this work successful. Special thanks to my co-director, Prof, J. Perron, for his support, gentle supervision and encouragement in the project. I am very grateful for all of your time and help during this research.

I would like to express my sincere appreciation to my comrades and collaborators at the University research centre in aluminum (CURAL) and the Anti-icing Material International Laboratory (AMIL) at the University of Quebec in Chicoutimi. I would especially like to name Hatem Mrad, Étienne Lafrenière, Simon Pilote and Caroline Laforte for their help during the simulation, experiments, and discussion. I would also like to thank Mme E. Mitchell for her efforts in editing my thesis.

I am also indebted to my friends Changiz Tavakoli and Hossein Hemmetjou, for their generous assistance and valuable advice. Very special thanks to both of them.

I am deeply and forever indebted to my parents for their moral support, patience and encouragement throughout my entire life. I am also very grateful to my brothers and sisters.

Table of Contents

List of Figures

List of Tables

List of Abbreviations and Symbols

Symbol	Description
AMIL	Anti-icing Materials International Laboratory
FEM	Finite element method
LEFM	The linear elastic fracture mechanics approach
UQAC	University of quebec in chicoutimi
A	Cross-sectional area
b	Width
C	Cracking conditions for a particular crack, the undamaged constitutive matrix
D	A diagonal matrix representing the damage accumulated at the interface, the material tangent stiffness
D_{nt}^{II}	crack opening
d	The highest mixed-mode relative displacement , grain diameter
d_c	Critical grain size
e	Porosity
e_{nn}^{ck}	Crack opening strain
E	Young's modulus
F^B	Body forces
F^i	Concentrated forces
f_{int}^e	Internal force vector
F^S	Surface traction
f_t	Tensile strength
G	Shear modulus, stress energy release rate
G_c	Post-cracking shear modulus
G_F	Fracture energy
$G_{IC}, G_{IIC}, G_{IIIC}$	Relative critical energies released at failure for Mode I, II or III
h	Height
I	Moment of inertia, the identity matrix
K	Stress intensity factor
K_{elem}	Element stiffness
K_{Ic}	Fracture toughness
K	Bulk modulus
K_P	Penalty stiffness
K_t^e	Tangent stiffness matrix
M	Bending moment
m	Weibull modulus
n	Balance coefficient

n, s, t	Crack normal directions
N_k	Standard lagrangian shape functions
N_n	Shape function corresponding to the n-th degree of freedom
P	Probability of fracture, force
q	Nodal displacement vector
$q_{1j}^{\pm}$, $q_{2j}^{\pm}$, $q_{3j}^{\pm}$	Three translational degrees of freedom for node j
S	Elastic section modulus of the beam
S, N	Interlaminar shear strength in mode II and III
S_{coh}	Cohesive surfaces
$S_e^{\pm}$	Upper and lower surface of element
t	Stress in the local cracking system
T	Interlaminar tensile strength in mode I
t_{coh}, t_{ext}	Tractions across the cohesive surfaces and on the external surfaces
U_f	Required energy to fracture the ice
U	Total potential energy of system
U_0	Elastic energy of the un-cracked plate
U_a	Decrease in the elastic energy
U_n	Crack normal displacement
$\overline{U}$	Virtual displacements
u	Displacement field
u_i^+, u_i^-	Components of the displacements of the top and bottom surfaces
u_{ki}^+, u_{ki}^-	Displacements in i direction of k top and bottom nodes of the element
U^T	Displacements of the body
U_γ	Increase in the elastic-surface energy
V	Shear force
V	Ice volume
W_{int}, W_{ext}, W_{cnt}	Virtual work of internal, external and contact
$W(u)$	Virtual work
y	Distance from the neutral axis

Greak symboles

Symbol	Description
δ	Displacement
Δ	Displacement vector
υ	Poisson's ratio
λ	Lame's constant
ρ	Density of pure ice

ρ'	Density of the ice
θ	Temperature
σ	Yield tensile strength
σ_c	Compressive strength
$\dot{\varepsilon}$	Strain rate
σ_y	Yield stress
σ_i	A measure of the crystal lattice's frictional resistance to slip
υ	Stressed volume
σ_f	Mechanical resistance of the ice
σ_x	Normal stress
τ	Shear stress
ψ	Phase angle
δ_c	Critical separation distance
σ_{tf}	Maximum tensile strength
σ_t^I	Failure stress
$\alpha(e_{nn}^{ck}, e_{tt}^{ck})$	Shear retention factor dependence on crack opening
ρ	Shear retention factor
σ	Traction
δ^f	Displacement at failure
σ_z	Normal traction
δ_{II}	Total tangential displacement
δ_m	Total mixed-mode displacement
δ_z	Opening displacement in mode I
β	Mode mixity
ε^T	Strain
τ^T	Stress
$\bar{\varepsilon}$	Virtual strains
σ	Cauchy stress tensor
θ_{si}	Transformation tensor
$\delta\Delta$	Virtual relative displacement vector
η_1, η_2	Natural coordinate system
τ_{xz}, τ_{yz}	Transverse shears
δ_x, δ_y	Two orthogonal tangential displacements
δ_I^f, δ_{II}^f	Ultimate opening and tangential displacements
δ_I^0, δ_{II}^0, δ_{III}^0	Onset displacements in mode II and III
δ_I^f, δ_{II}^f, δ_{III}^f	Final relative displacements for Mode I, II or III

CHAPTER 1

INTRODUCTION

CHAPTER 1

INTRODUCTION

1.1 General

In cold-climate regions (which include about a third of the continental United States, Canada, Alaska, northern Europe, and part of Asia), ice causes many serious problems. For example, ice on aircraft wings and helicopter blades endangers passengers (see Figure 1.1). In recent years, several fatal aircraft accidents have been caused by ice accumulation on aircraft structure. An example is the US Air Flight 405, which crashed during takeoff from La Guardia Airport on 22 March 1992, New York, as a consequence of icing on the aircraft [11]. Ice on ship hulls, which requires additional power to navigate through water and ice, creates navigational problems, and certain unsafe situations. Finally, icing of power lines and communication towers often causes them to break and lose power. In short, ice and snow adhere to power lines and add so much weight that the power lines break. Such power outages can significantly impact human life for extended periods. Further, repairing power outages is extremely costly. One recent example is the great Canadian ice storm of 1998, in which damage to transmission lines has been estimated at about C$2 billion [68].

Ice/material interfaces is a subject of great interest in such problems as icing of electrical transmission cables, highways and bridges, constructions, off-shore structures,

aircrafts and helicopters. To eliminate the problems of ice formation and build-up on the structural components, improving the mechanical parameters, anti-icing and de-icing methods should be taken into consideration. In developing anti-icing methods, a good knowledge of adherence properties of ice is required, and the bulk characteristics of ice are also of interest. A review of the literature shows that few studies have been done to developing de-icing techniques and icing processes. Therefore, the exigency of the de-icing and anti-icing research filed seemed necessary and, consequently, the main research filed in the Anti-icing Materials International Laboratory (AMIL) at the University of Quebec at Chicoutimi is the study of de/anti-icing fluids which are used in aviation to remove and prevent aircraft contamination through frozen deposits on the ground [48].

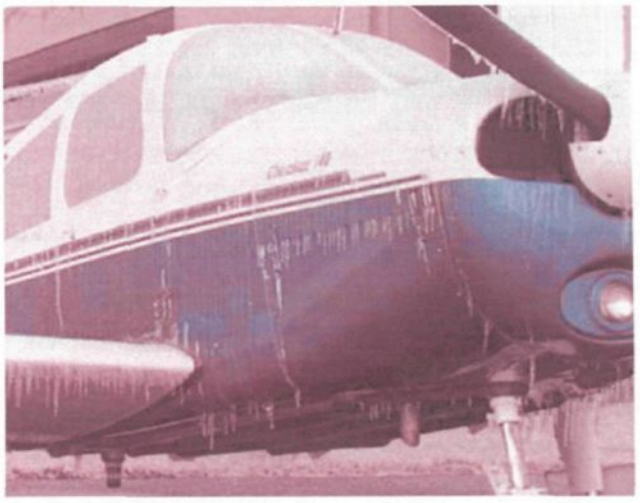

Figure 1.1: Effect of ice on helicopter wings [1].

[1] http://www.aopa.org/asf/publications/sa22.pdf

1.2 Problem overview

The mechanical interactions of the interface between ice and solids have long been of interest in fields ranging from windshield icing to aircrafts. An understanding of the mechanical properties of ice/material interfaces is essential in the development of de-icing techniques. When ice accumulates on solid bodies, it is very difficult to remove it and this problem generally derives from the propensity of ice to form and stick onto surfaces. In other words, this is related to interfacial forces between ice and substrate like the adhesive and cohesive strengths of ice. For many years, various methods have been developed for de-icing to obtain the maximum reliability of infrastructure service [61]. However, of all the proposed methods [58], some of the methods have been developed to present difficulties of the application according to the type of substrate. Unfortunately, the application of various de-icing techniques which have been developed to date is quite difficult for different types of surfaces and generally requires a considerable energy contribution as well as complex and expensive installations for testing and simulating the ice problem. Therefore, preventing ice buildup on substrates has long been a technological challenge. Some de-icing methods have been developed by taking the concept of mechanical or thermal energy into consideration [60]; also, numerous materials, coatings, and paints having low friction properties (icephobic materials) are used to eliminate or reduce of ice accumulation. These methods are efficient but none of them are ideal, because some de-icing substances can have significant negative environmental impacts, and, although this icephobic material attempts to prevent the formation of ice on a surface, but many of these are temporary. Ideally, these materials would also be reliable, durable, and inexpensive [59]. In order to develop new techniques

for de-icing and anti-icing, and optimize existing methods, we need to make an effort to improve our knowledge of the mechanical phenomena at the ice/solid interfaces.

The object of this project has been in development by C. Laforte since autumn 2002 [62]. One subject of this project is to study the mechanical behaviour of some freezing substrates under traction in order to simulate the effect of ice on the different substrates. However, the current results do not make it possible to adequately determine the mechanisms and parameters characteristic of the delamination of ice layer on the substrate. While the mechanical properties of the interface between ice and solids have long been of interest in fields from airplane design to glaciology, as a step toward understanding mechanical interactions between ice and substrates, to improve mechanical ice removal and de-icing techniques, this research has focused on understanding the interactions between an ice surface and an aluminium plate.

A satisfactory ice model for use in recognizing the interfacial forces between ice and substrate is not yet readily available, despite the fact that considerable studies on icing phenomena have been performed by researchers in this domain. The reason for this lack is due to the fact that researchers have usually been interested by research in the icing phenomena with experimental knowledge alone when simulating this process embodies a vast field of abstract knowledge.

It is widely recognized that significant ambiguities exist in the ice models in use today, but nearly improved software engineering and developed computing technology accompanied by new experimental methods make it possible to quantify the uncertainties in ice models and to develop new ice removal techniques (de-icing) and load prediction models for the safe and economical design of structures. The necessity of modeling ice

fields arises from such important practical problems as testing models of icebreakers under laboratory conditions and investigating the interaction of ice on structures.

It is absolutely clear that the correct design of experiments may be of considerable help in solving these problems without wasting effort, means, and time. However, performing such tests requires skill in preparing ice with the necessary properties. Certainly, as our understanding of principal mechanisms of ice failure and processing becomes better and better, ice models will become more and more accurate. Difficulties in ice modeling arise primarily from several sources.

1) Incomplete modeling of the mechanical behaviour of ice, including temperature and fracture effects. The study of ice fracture is complicated by the fact that ice properties are rate-sensitive, *e.g.*, stress–strain relationships are a strong function of the rate of deformation. In consequence, it has been difficult to separate rate-dependent effects from pure elastic behavior, and the ice literature is replete with conflicting data regarding the energy of fracture, which is a critical quantity in any fracture-based analysis.
2) Problems with testing to investigate the mechanical parameters of ice. Many researches have investigated the mechanical properties of ice. However the data obtained from similar tests often either differ greatly, or are contradictory. This difference is because practically every laboratory and ice research group has its own testing method to investigate the mechanical properties of ice. The different features of ice, like anisotropic and viscoelastic behavior, must be considered together with different test conditions during studies of ice properties, because neglecting these

parameters can cause results to differ from test to test. Therefore, the mechanical properties of ice are a function of test conditions.

3) The nature and the complexity of ice behavior. Ice is a material which is very sensitive to loading rate, temperature, and other factors such as grain size, porosity and crystalline orientation.
4) Inadequate modeling of the interfacial loads and contact forces at the ice-structure interface.
5) The finiteness of environmental and other forces driving the ice features.

In order to quantify these difficulties and to better predict ice loads, numerical models are necessary for the computer simulation of ice-structure interaction processes. In comparison to analytical methods, such models must be able to simulate the mechanical behaviour of ice practically for multiple modes of failure in ice. An important aspect of the development of constitutive models is the need for accurate and consistent experimental data on ice, especially to characterize its behaviour relating to tensile loading, multiaxial loading, nucleation, propagation and interaction of cracks, material anisotropy, and fracture toughness. Numerical simulations can help to establish the significance of more extensive testing in quantifying the ice-structure interaction process.

1.3 Literature review

1.3.1 Introduction

Over the past decade alone, more than 10,000 papers on ice have been published in the scientific and engineering literature. Nowadays, knowledge of the mechanical behaviour of ice has certainly increased to the point where some basic constitutive laws

can be formulated and scaled down for physical models in order to investigate engineering problems caused by ice. Significant efforts have been made to develop models for predicting the mechanical behaviour of ice under various loading and to measure the forces caused by the impact of ice on structures.

The first such models were made just after World War II in Canada, with paraffin to model the ice [33], and in the U.S.S.R. with weakened ice and paraffin [90]. Since the 1980s, plenty of research has focused on the modeling of ice accretion on different objects: icing on road surfaces [89], transmission line icing [38, 41, 54, 69 and 75], non-rotating cylinders [67 and 70], and other objects [93].

Two basic categories of the various models that have been developed based on the different backgrounds and physical properties of different icing phenomenon are physical and empirical models. Physical icing models are quite detailed and require specific definitions of meteorological parameters including droplet size, water or vapor content in air, wind speeds, and temperature. Detailed models are computationally requiring and have therefore been improved alongside the technological improvements of computers. The second category consists of empirical and statistical models that are based on historical data from meteorological stations. Although empirical models can provide useful information for predicting material behaviour, their development beyond the specified limits is usually unreliable. The physical models should be used as a forecasting tool for much wider limits.

A number of studies have been done on the strength of ice/solid interfaces [4, 63, 71 and 92]. In these studies, the adhesive strength of ice on various solid surfaces has been tested in terms of tensile, shear, and impact strength, and it has been found that

mechanism of ice adhesion has strongly sensibility on the testing technique conditions and the testing employed. Because the testing methods and specimen geometries used in these studies were quite different, a comparison of the results obtained by the researchers is difficult. Moreover, some testing methods are not suitable for the study of ice/solid interfaces [71]. Most investigations related to de-icing has been focused on mechanical ice removal strategies because of practical considerations, and very little has been directed towards a fundamental understanding of the ice adhesion process. The first attempts to understand basic adhesion dates back to the 1850s, when Faraday [31] studied the adhesion between two spheres of ice brought into contact. He correctly explained this adhesion by assuming that there is a thin ''liquid- like'' layer (a film of water on ice) at the surface of ice which seemed to persist to temperatures as low as -30°C. Basic adhesion is an intrinsic property of the interface and it can be determined only by the atomic structure and chemistry of the interfacial region. It can be characterized by either the intrinsic tensile strength σ_i or the intrinsic toughness G_i of the interface; both of these parameters are related to each other via the fundamental interface stress-separation curve [40].The energy consumed in propagating a unit area of a crack along an ice/substrate interface or the total toughness of the interface as may occur during any ice removal process depends upon many external parameters such as the temperature, specimen geometry, loading rate, substrate roughness, absorbed impurities, interface flaw density, and the ratio of the tensile to shear stress ratio separating the interface [9].

The ice literature includes some studies that have measured the total interface toughness directly or indirectly. Jellinek [52] examined the adhesive properties of snow-ice sandwiched between various materials such as stainless steel, various polymers and

block copolymers applied to aluminium substrates under both tensile and shear loading. The overall interface shear strength was found to depend upon the loading rate, degree of surface roughness, temperature and type of the substrate material being tested [52]. Landy and Freiberger [63] worked on the adhesion of ice to various plastics using a shear apparatus similar to that used by Jellinek. They attempted to obtain a relationship between the adhesion strengths to physical and chemical properties such as critical surface tension of wetting, contact angle, coefficient of thermal conductivity and thermal expansion, porosity, dielectric constant, and flexural modulus. They were not successful in this attempt, probably because such tests are unable to make a distinction between the effects of different variables separately. In fact, shortly after Jellinek carried out many of his studies on ice adhesion, progress in interfacial fracture mechanics was made by Rice and Sih [78]. They found that when a crack exists within the interface between unlike substances, the local stress state is a combination of shear and tension, even when the interfacial crack is loaded under uniaxial tension mode (Mode I) or shear mode (Mode II). The exact ratio of the tensile to shear stresses depends upon the mismatch in the elastic properties of the two materials. As an example, for the steel-ice interface, under pure Mode I loading, a shear stress is about 15% of the tensile. So, without knowing the real local stress state which is responsible for either the cohesive, adhesive, or mixed failure, the conclusions drawn by Jellinek assuming the locus of failure caused by either pure applied tension or shear, remain questionable.

Because the successful development of physically-based models depends on our understanding of the mechanical properties of ice, the mechanical properties of freshwater ice is briefly reviewed below before methodologies to simulate de-icing

aluminium structure are given. Ice is a unique material; it can creep with very little applied stress or is extremely brittle, one of the most brittle materials on earth, and can fracture catastrophically given a high strain rate.

1.3.2 Mechanical properties of ice

In the following section, a short review of the mechanical properties of ice from several literatures is presented and the emphasis will be on freshwater ice. This review is essential in order to determine the ice material parameters in a numerical model.

1.3.2.1 Ice crystal structure

Ice exists in a large number of different crystalline structures, more than any other known material. Ice possesses 12 different crystal structures in total, as well as two amorphous states. At ordinary (low) pressures the stable phase is termed ice I. Ice I has two variants. Hexagonal ice Ih, whose crystal symmetry is reflected in the shape of snowflakes, has hexagonal symmetry and is obtained by the freezing of water at ambient pressure. Cubic ice Ic has a crystal structure similar to diamond and is formed by vapor deposition at very low temperatures (below -130°C). Amorphous ice can be formed by depositing water vapor onto a substrate at still lower temperatures and by compressing ice Ih at liquid nitrogen temperature [83].

1.3.2.2 Ice elastic modulus

There are two methods to determine the elastic modulus of materials: the static method using Hook's law and the dynamic method by measuring the propagation velocity of longitudinal and transverse elastic waves. The latter method provides the most accurate value of the elastic constants. The elastic behaviour of homogenous and isotropic material is described by two independent elastic constants: Young's modulus (E), and Poisson's ratio (υ). Many more constants are in use, such as bulk modulus (K), the shear modulus (G), and Lame's constant (λ), so it is possible to calculate each of these from the two others. These elastic constants are only defined for isotropic materials. Ice is only isotopic if the orientations of the c-axes of the ice crystals are random. If the distribution is not random, it is difficult to describe the elastic behaviour completely. The elastic modulus and Poisson's ratio of polycrystalline ice has been measured by subjecting plates of ice to biaxial bending [35]. Ice deformation includes elastic and creep processes, and the large-scale modulus is usually discussed in terms of an "effective modulus" that incorporates these processes. This modulus is a strong function of loading rate, temperature, and grain size and type. The values of Young's modulus range from approximately 2 GPa (2.9×10^5 psi) at low frequency loading to a high frequency value of 9 GPa (1.3×10^6 psi) [91] and Poisson's ratio has a range of $0.29 - 0.32$.

1.3.2.3 Ice tensile and compressive strength

The tensile and compressive strength of ice has been measured by a relatively small number of researchers [23, 28, 43, 46, 64, 83, and 104]. Tensile strength can be associated with either ductile or brittle mode of failure. In the range of brittle behaviour,

strength appears to be a function primarily of grain size and to a lesser extent, of temperature. For tensile strength in the brittle range, Michel proposed the following equation [72]:

$$\sigma = 7.94\times10^{4}\left[\left(1-\frac{e}{0.285}\right)\frac{\left(1-0.9\times10^{-3}\theta\right)}{d}\right]^{\frac{1}{2}} \text{Pa} \qquad (1.1)$$

where e is the porosity $(1-\rho'/\rho)$, ρ is density of pure ice (917 kg/m^3), ρ' is density of the ice (kg/m^3), θ = temperature (°C), d = grain diameter (m). In the range of ductile behaviour, the yield tensile strength is reported as being the same as the compressive strength up to a transition strain rate. That rate is a function of temperature and grain size. There is a relatively wide range of ice tensile strength, from 0.7 MPa to 3.1 MPa. The average tensile strength of ice from published investigations is 1.43 MPa in the temperature range −10 to −20°C. Over this temperature range, values of the uni-axial compressive strength of ice range between 5 – 25 MPa [43]. Analyses of strength measurements exhibit that strength increases with strain rate, up to a rate of $10^{-3}s^{-1}$, and generally decreases at higher strain rates because of the brittle fractures to which ice is prone. In the lower strain rate range below $10^{-3}s^{-1}$, the compressive strength of freshwater ice at -10 °C (263 K) is given by [91]:

$$\sigma_c = 212\,\dot{\varepsilon}^{0.34}\left(3.07\times10^{4}\,\dot{\varepsilon}^{0.34}\right) \qquad (1.2)$$

where σ_c is in MPa and $\dot{\varepsilon}$ is in s^{-1}.

Ice tensile and compressive strength depends on the variables of strain rate, temperature, tested volume, and ice grain size. These dependencies will now be discussed:

1) Effects of temperature:

Generally, the tensile and compressive strength of ice increases with decreasing temperature, as shown in Figure1.2. This temperature effect on strength is more noticeable in compression than in tension. Haynes reported [43] that the compressive strength of ice increases by approximately a factor of 4 from 0°C to −40°C, while the tensile strength of ice increases by a factor of only 1.3 over the same temperature range. Schulson has suggested that dependence of compressive strength of ice to temperature is related to ice dislocation and grain boundary sliding phenomena that is caused a temperature-dependent of damage accumulation [83]. The low temperature dependence of tensile strength is related to the localization of stress-accommodating mechanisms at the tips of tensile cracks [74].

2) Effects of strain rate:

As Figure 1.3 shows, the effect of strain rate on the tensile strength of ice is very small compared to its effect on the compressive strength [83]. It is obvious that the compressive strength is strain-rate sensitive, while the tensile strength is strain-rate insensitive, over the range of strain rates examined. Tensile stress-strain curves of ice exhibit that at low rates of deformation, cracks do not form, and the material is ductile, but at high strain rates, cracks do initiate, and the material is brittle. Compressive stress-strain curves show ductile behaviour at low and intermediate strain rates, but brittle behaviour at high strain rates. [83].

3) Effects of grain size:

As shown in Figure 1.4, the tensile strength of ice decreases with increasing ice grain diameter. These data are well described by a Hall-Petch relationship:

$$\sigma_y = \sigma_i + k d^n \tag{1.3}$$

where σ_y = yield stress, σ_i = a measure of the crystal lattice's frictional resistance to slip, k = a constant reflecting the extent at which grain boundaries impede slip propagation, d = average grain diameter and the exponent n = −1/2. This $d^{-1/2}$ dependence implies that the tensile strength of ice is controlled by a stress concentration process. [23].

4) Effects of volume:

With increasing test specimen volume, the tensile strength of ice decreases as shown in Figure 1.5 [25]. Effects of volume on the strength of brittle materials are usually described by a Weibull statistical distribution approach [102]. In the Weibull theory, the probability of fracture is given by:

$$P = 1 - \exp(-\upsilon \left(\frac{\sigma}{\sigma_0} \right)^m) \tag{1.4}$$

where P = probability of fracture, σ = applied tensile stress (which is assumed to be uniform over the stressed volume of the material), σ_0 = a constant, υ = stressed volume, and m = Weibull modulus. The volume dependence of the strength of brittle materials is given by:

$$\frac{\sigma_2}{\sigma_1} = \left(\frac{\upsilon_1}{\upsilon_2}\right)^{\frac{1}{m}} \tag{1.5}$$

From the strength-volume data in Figure 1.5, the Weibull modulus of ice is estimated to have a value of approximately 5 [74].

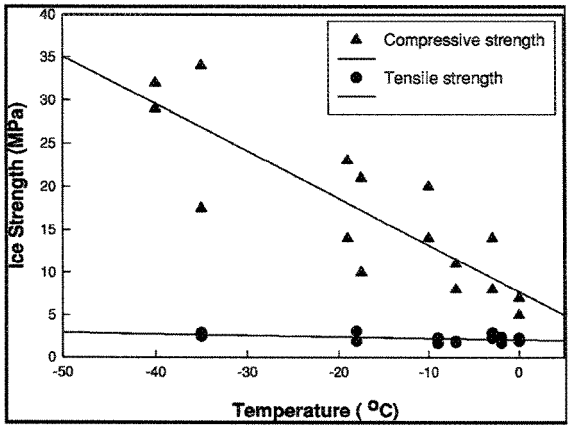

Figure 1.2: Tensile and compressive strength of ice as a function of temperature [8].

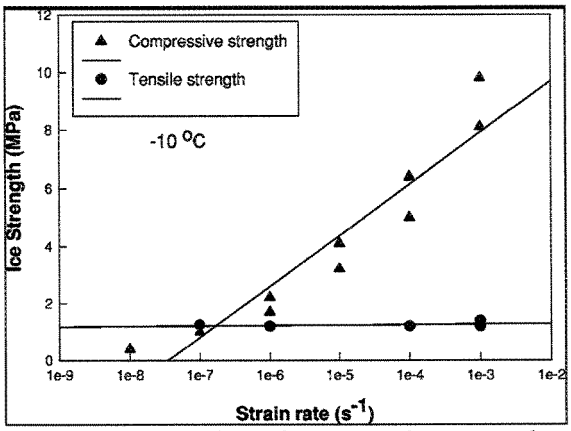

Figure 1.3: Tensile and compressive strength of ice as a function of strain rate [38].

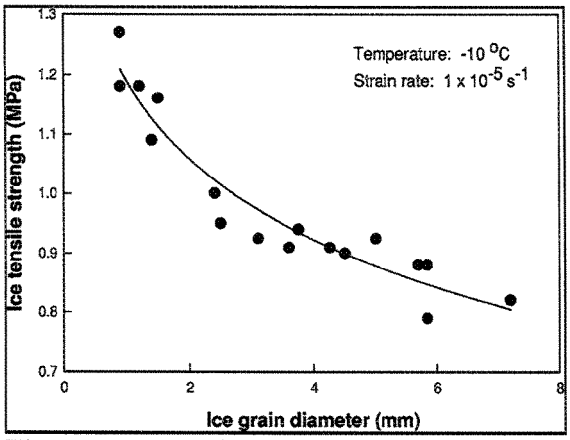

Figure 1.4: Tensile strength of ice as a function of grain size [67].

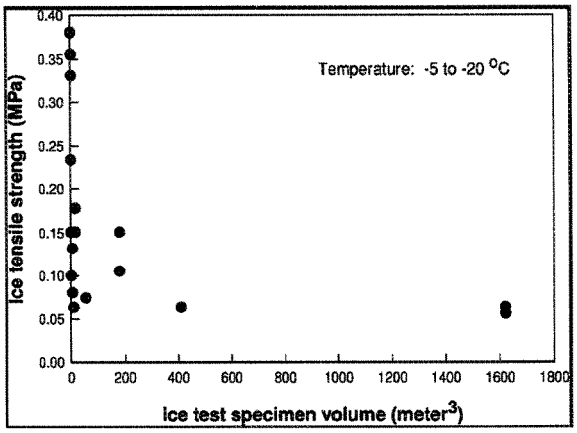

Figure 1.5: Tensile strength of ice as a function of volume [4 and 92].

1.3.2.4 Fracture toughness

The fracture toughness of ice has still seen only limited investigation [7, 15, 32, 50, 73, 97 and 100]. Fracture toughness or critical stress intensity factor is a material property that determines the stress necessary to propagate a crack of known size. Generally, the

fracture toughness of ice is in the range of 50 –150 kPa $m^{1/2}$, and typical values for freshwater ice range from $109 \pm 8 kPa\ m^{0.5}$. By way of comparison, the fracture toughness of glass is typically 700 –1000 kPa $m^{1/2}$ [8]. Thus, ice has roughly one-tenth the fracture toughness of glass.

The fracture toughness of ice depends on the ice type and is relatively insensitive to loading rate, with less variation ascribable to grain size and temperature. The fracture toughness of ice as a function of temperature [73, 97 and 100], loading rate [15, 73 and 97] and grain size [50] is shown in Figures 1.6, 1.7 and 1.8 respectively.

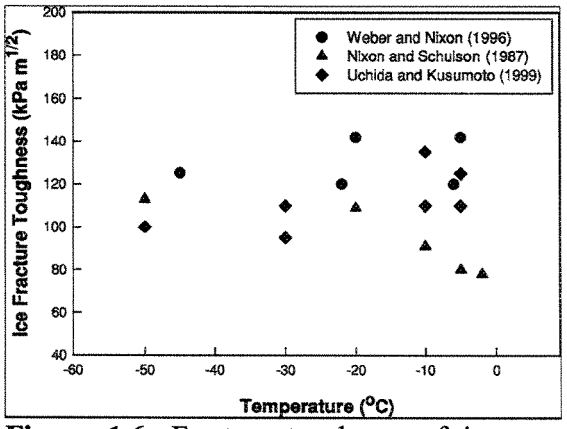

Figure 1.6: Fracture toughness of ice as a function of temperature [73, 97 and 99].

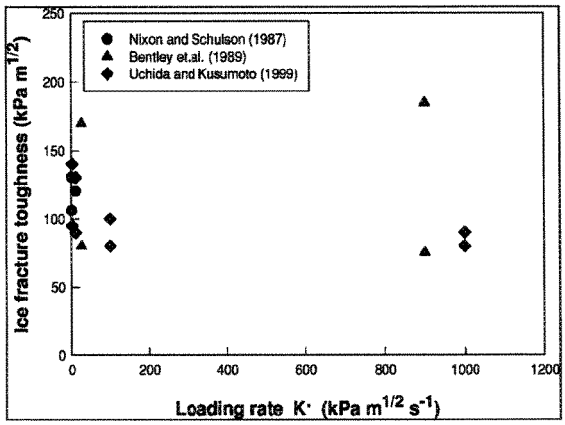

Figure 1.7: Fracture toughness of ice as a function of loading rate [15, 73 and 97].

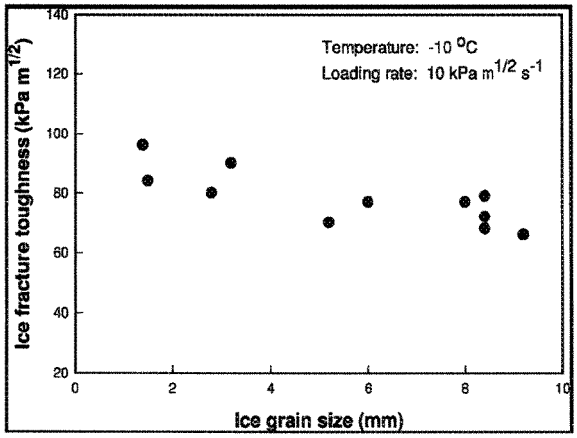

Figure 1.8: Fracture toughness of ice as a function of ice grain size [50].

1.3.2.5 Creep of ice

Ice is thus a material similar to a metal at high temperatures and the controlling creep mechanism is dislocation climb. Typical creep curve is shown in Figure 1.9. There are three distinct regions in the creep curve which can all be seen under favorable conditions. The region of decelerating (primary or transient creep) extends from point B to point C, where the creep-rate decreases continuously. In region BC (region of steady-state or secondary creep) the creep-rate remains constant, indicating a nearly steady state condition. Beyond C (tertiary or accelerated creep) the creep-rate increases again until it reaches a new steady state creep-rate, which is considerably greater than that observed during secondary creep [72].

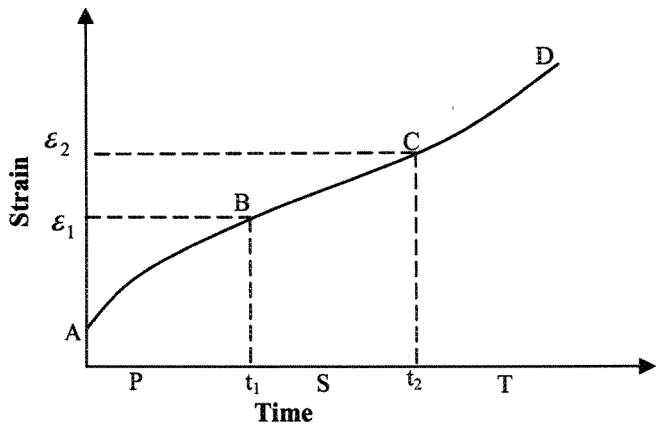

Figure 1.9: Schematic creep curve for polycrystalline ice under constant load.

1.3.3 De-icing

De-icing is the process of removing an accumulation of ice from a surface. De-icing can be accomplished by mechanical methods (scraping, brushing, blowing, wiping), through the application of heat, by use of chemicals designed to lower the freezing point

of water (various salts or alcohols), or a combination of these different techniques. As pointed out by Laforte et al, [61], there are four different techniques for de-icing:

1) Thermal de-icing technique, based on melting of ice;
2) Mechanical de-icing technique, based on the bricking and removing of ice;
3) Passive methods, based on natural forces;
4) Various methods, based on combination of these three different techniques.

Thermal de-icing techniques must be warm enough to melt ice which has already formed on a substrate completely or partially at interface or to prevent ice formation. The melting of the ice or de-icing is obtained by directly heating the ice, or by an intermediary of the substrate:

1) De-icing induced by Joule Effect (substrate's case);
2) Electro Impulse De-icing: in this method an electromagnetic coil is placed behind the surface skin that induces strong eddy currents in the metal surface.(case of substrate and ice);
3) Hot water de-icing (case of substrate and ice);
4) Using de-icing fluid with a lower freezing point and faster ice-melting action (case of ice)

Ice formation can be prevented in thermal de-icing techniques by:

1) Heating substrate to a positive temperature;
2) Covering the substrate with a substance which dissolve the collected particles of ice and prevents the coagulation of the water droplets.
3) Heating the rainfall (rain, snow, hail, etc) before freezing precipitation hits the substrate, for example using Hertzian waves (radio waves, microwaves, laser).

Unlike the thermal processes, the mechanical techniques only allow de-icing. Mechanical methods are based on the principle that ice is a very brittle material at a very high strain rate, which makes it very easy to break by shocks; therefore, the energy is not being dissipated by the plastic deformation of ice.

The great brittleness of atmospheric ice against the shock mechanics is illustrated in Figure 1.10, which shows resistance of ice samples at -2 °C in tension and compression as a function of strain rate [61]. As the figure shows, there are three distinct regions, and each region corresponds to a definite interval of strain rate. At a very low strain rate, lower than $10^{-5}s^{-1}$, the deformation of ice in both the tension and compression is in a ductile mode. At a very high strain rate, more than $10^{-3}s^{-1}$ (> 0.1 % per sec.), the failure of ice in both the tension and compression is in brittle mode. In the range of strain rate between $10^{-5}s^{-1}$ and $10^{-3}s^{-1}$ the behaviour of ice is ductile in compression and brittle in tension.

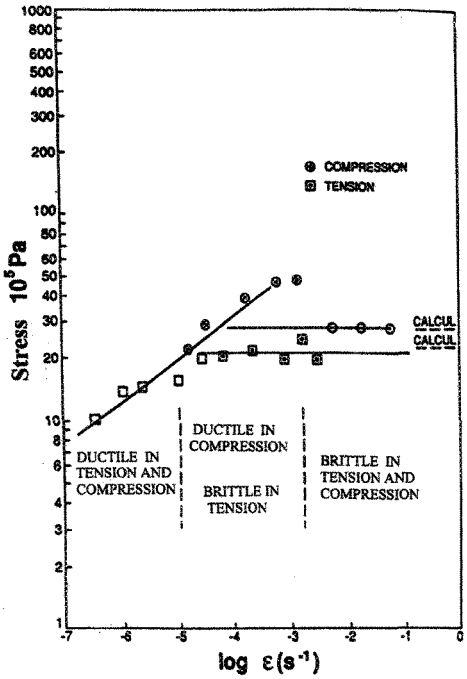

Figure 1.10: Strength of ice in tension and compression at -2° C [61].

The energy required to fracture the ice in brittle mode depends on three factors:

1) The mechanical resistance of the ice σ_f (a function of temperature and microstructure);
2) The Young's modulus E (a function of mass density) ;
3) The ice volume V.

This energy U_f can be determined by:

$$U_f = \frac{V\sigma_f^{\,2}}{2E} \tag{1.6}$$

Replacing a cylindrical mass of ice with thickness e and length L_c distributed around a conductor's diameter D_c, we obtain:

$$U_f = \frac{L_c \pi D_c e \sigma_f^2}{2E} \tag{1.7}$$

In this equation, the adhesion force of ice on the cylindrical conductor is not considered. According to Equation 1.7, the amount of energy required to break a layer of 3mm ice at -2° C on a conductor with a diameter of 37 mm in the brittle mode is very small, for example, 0.08 Joule/m in tension and 0.13 Joule/m in compression which corresponds to 0.25 and 0.42 Joule/kg respectively [61]. As illustrated in Table 1.1, when the temperature decreases the resistance increases. The energy required for breaking the ice layer using mechanical shocks is very small compared to the quantity of energy which is necessary to melt it. Also, the amount of energy required to break 3mm ice using mechanical shocks between -2 °C to -14° C is 70000 to 1400000 times less than the energy required for melting [61].

Table1.1: Energy required for thermal and mechanical de-icing [61].

Method	Type of ice	Temperature	Joule/m	Joule/kg	Joule/m^2
Thermal	Glaze	0°C	10.5×10^4	3.33×10^4	9.0×10^4
Shocks tension	Glaze	-2°C	0.08	0.25	0.69
Shocks compression	Glaze	-2°C	0.13	0.42	1.12
Shocks tension	Hard rime	-14°C	0.12	0.38	1.03
Shocks compression	Hard rime	-14°C	2.2	7.0	18.9

Therefore, because of this low consumption of energy, using mechanical methods is much more economical than using thermal methods.

For de-icing clean metal surfaces there is little profit in changing one metal to another, since generally the interfacial adhesion will be stronger than the strength of the ice. For this reason, ice removal cannot be accomplished by overcoming the interfacial adhesion, but only by breaking the ice itself near the interface. If the ice is not confined, it will tend to fracture in a brittle mode and this will be more noticeable at lower temperatures, as brittle fracture will generally occur at relatively low stresses. However, it may be possible to decrease the shear stress, even in the ductile range, if small amounts of salt or another anti-icing material are added to the ice.

1.3.4 History of fracture mechanics of brittle materials

The first milestone in the history of fracture mechanics was stated by Griffith in his famous 1920 paper that relates the energetic approach to fracture propagation and then continues afterwards with the cohesive models of Hillerborg [44]. Griffith recognized the macroscopic potential energy of the system consisting of the internal stored elastic energy and the external potential energy of the applied loads, varied with the size of the

crack. His theory began with the base of the hypothesis that brittle materials contain elliptical microcracks of length 2a oriented perpendicular to the maximum principal stress, which present high stress concentrations near their tips. He developed a relationship between crack length (a), surface energy connected with traction-free crack surfaces (2γ) and applied stress to propagation of a crack in a brittle material:

$$\sigma^2 = 2\gamma E/\pi a \tag{1.8}$$

Later, in 1957, Irwin provided the expansion of Griffith theory to an arbitrary crack and proposed the criterion for a growth of this crack (crack propagation). This criterion states that crack propagation can only occurs when the stress energy release rate (G), exceeds the critical value of G_C, which is required to create a new unit crack area. Irwin displayed that the stress field in the area of the crack tip is completely determined by the quantity K (stress intensity factor) $K_I = \sigma\sqrt{\pi a}$. Subscript I in the parameter K refers to mode I loading, the opening mode. Other modes of deformation at a crack tip are mode II (sliding mode) and mode III (tearing mode). In 1961, Kaplan focused on the possibility of applying the linear elastic fracture mechanics approach (LEFM) to concrete. In 1985, Hillerborg proposed a three-point beam test to determine the fracture energy (G_F) of concrete. The fracture energy is the energy necessary to create a unit crack surface and it represents a fracture property with the tensile strength f_t and the softening law. The constitutive relationship is described by a material softening law between tensile stress and local opening (width of fracture process zone), instead of a stress-versus-strain relationship for the continuous materials. This model can be applied to simulate the formation and propagation of crack using the finite element method. An energy criterion is used to simulate the crack propagation, which can be generalized for

non-linear materials behaviour. This model is especially suitable for finite element analysis (see Chapter 3).

1.4 Objectives

The main objectives of the planned research work are:

1) To develop a 3D numerical model to simulate the de-icing of an aluminium structure.
2) To study mechanisms of interaction between ice and substrate using the hypothesis of fracture propagation criteria and models that could explain these observations.
3) To compare the simulation results with the experimental results obtained from tests in the AMIL laboratory, and draw conclusions regarding the accuracy of the models.

The primary objective is to study the mechanical behaviour of the interface between ice (in the brittle region) and substrate to improve mechanical de-icing techniques. To obtain the relationship between ice dimensions on interfacial forces between ice and aluminium in order to develop an accurate model and to ensure its verification, the various mechanisms and parameters characteristic of the delaminating of the ice will be studied. To do so, the realistic behaviour of the ice, as well as the geometry of the components and the mechanisms occurring at the interface must be considered.

The ultimate goal of this project is to develop a three-dimensional finite element model to simulate the de-icing aluminium structure. This could correctly represent the behaviour of the interface between ice and aluminium. For this, besides the required data from literature, some systematic experimental tests are necessary, e.g to determine the

required supporting experimental data for modeling a traction test. Also, for fitting reliable interaction parameters, some data must be estimated.

1.5 Methodology

Initially, the proposed methodology consists of establishing a mathematical model allowing a good representation of the experimental delaminating tensile tests that carried out within the framework of the doctoral project of C. Laforte, [62].

Firstly, the model will be considered with the simplifying assumptions, such as linear elasticity of materials. The substrate (aluminium) as well as the ice is supposed to obey Hook's law. In this way, the effect of adhesion and cohesion between the ice and the substrate is ignored. From a purely qualitative point of view, it will be worthwhile to check the influence of the geometrical parameters (width, length, and thickness of the substrate, thickness and profile of the ice) and materials specifications (Young modulus, Poisson's ratio) on the shear stress distribution at the interface.

Then, modeling will be carried out finely, and the effect of adhesion and friction between the ice and the substrate will be taken into account using cohesive material theory; the nonlinear behaviour of the ice and the substrate will be considered. Certain constitutive laws make it possible to take into account the energy dissipated by the mechanisms of cohesion and friction at a total assessment [27]. Also, the constitutive law for the ice, taking into account the distinct behaviour in traction and compression with cracking, must be planned in order to adequately capture the risks of cracking before delamination, as the unknown parameters of these laws will be obtained by retro-

engineering with the experimental results.Then it will be possible to quantify the energy that is mobilized by the interface during delamination.

The proposed approach provides a framework for ice using appropriate progressive failure analyses where delamination is present. The approach consists of using interfacial decohesion formulation between the ice and an aluminium plate. The constitutive equations for the interface consist of mechanical relations between the tractions and interfacial separations. When the interfacial separation increases, the tractions across the interface reach a maximum decrease, and vanish when complete decohesion occurs. The work of normal and tangential separation can be related to the critical values of energy release rate, G [7].

ABAQUS, a general purpose finite element software, has been selected as the basic platform for this study. ABAQUS has a unique procedure for attaining solutions for interface using cohesive material: the unique ability to simulate delamination and de-icing. In order to predict the initiation and growth of delamination, an eight-node decohesion element is developed and implemented in the ABAQUS finite element code [1]. The decohesion element is used to model the interface between two layers, or between two bonded components. The material response makes it possible for the element to represent damage using a cohesive zone ahead of the crack tip to predict delamination growth.

To analyse the delamination growth using decohesion formulation, a fracture mechanics approach and evaluating the components of the energy release rate G, is applied. The energy release rate G values are usually evaluated using the virtual crack closure technique (VCCT) proposed by Rybicki and Kanninen [57]. The approach is

computationally effective because the components of the energy release rate can be obtained from only one analysis.

Decohesion formulations are specified on the basis of a Dudgale-Barenblatt cohesive zone approach [10 and 29], which is related to Griffith's theory of fracture when the cohesive zone size is negligible compared with characteristic dimensions, regardless of the shape of the constitutive equation [19]. These decohesion formulation use failure criteria that combine aspects of strength-based analysis to predict the softening process at the interface and fracture mechanics to predict delamination propagation. A main advantage of using cohesive elements is that without previous knowledge of the crack location and propagation direction, both onset and propagation of delamination can be predicted.

1.6 Overview of the thesis

This research introduces and discusses a finite element model that predicts the initiation and growth of delamination of ice/aluminium using decohesion formulation to model the interface between ice and aluminium (de-icing). The following is the summery of the contents of various chapters presented in this thesis:

Chapter 1 introduces the problem of ice in cold regions and also provides a brief review of the literature. In addition, the necessity of the research, the general objectives, and the methodology are outlined briefly in those sections.

Chapter 2 presents the laboratory experiments. Such experiments were carried out with different thicknesses of ice. The ice-making method and conditions are explained in

this chapter. The data from these experiments will be modeled by the ABAQUS codes for comparison with numerical model and for the validation of computer codes.

Chapter 3 presents the mathematical model and also contains a discussion of the cohesive material theory and the thought that went into the use of cohesive material to define the interfacial forces and brittle cracking constitutive low to define the brittle failure of ice. Also, it explains how the cohesive elements are used to show how this method can support the analysis and presentation of data.

Chapter 4 presents the linear and nonlinear approach. Also, this chapter concludes with some comments and the results of some simulations performed under three different thickness of ice.

Chapter 5 contains the important conclusion and the main observations of the thesis are made in this chapter. This chapter ends by hinting at the scope and the possible directions for further work.

CHAPTER 2

EXPERIMENTAL TESTS

CHAPTER 2

EXPERIMENTAL TESTS

2.1 General

The mechanical properties of structural materials are normally determined by tests which subject the specimen to comparatively simple stress conditions. For example, most of our information concerning the strength of material has been obtained from tensile tests. In a tensile experiment, the specimen is gripped firmly by mechanical jaws at the wide portion on either side and extended by means of a tensile testing machine. The pulling is normally carried out at different rates, depending on the type of material being tested. The low speeds are used to test rigid materials, and the higher speeds are chosen to test flexible materials. In this research, the tensile tests of ice accumulated on aluminium plates were carried out in order to introduce a model finite element that predicts the initiation and growth of delamination of ice/aluminium.

2.2 Sample preparation and icing

In order to have repeatable and comparable tests, all tests must be accomplished under suitably controlled conditions. Controlled conditions include the use of an appropriate cooling system (temperature), wind velocity (air circulation), water spraying

system and ice thickness deposited on an aluminium plate. Table 2.1 shows the experimental conditions of ice samples. In this study, the fine granular ice deposited on the aluminium plate was fabricated by spraying very fine water mist at -10 °C in one cold room at the AMIL laboratory. The water mist dropped on the surface of an aluminium plate which was firmly clamped by the mechanical jaws of the tensile test machine and quickly frozen to form a fine granular ice layer. Before the icing, the aluminium plate was elongated by approximately 0.05%. In this manner, the aluminium plate was perfectly horizontal and the ice accumulated uniformly. The length of the aluminium plate was 168 mm, and the width and the thickness of the plate were 18.87 mm and 0.43 mm, respectively.

Briefly, the method used to make ice with small crystal grains on aluminium substrate consisted of the following steps:

1) Suitable meteorological factors such as wind velocity and droplet size were controlled by using suitable air and water pressure, determined by trial and error, in the climate room. This room had been equipped with a water droplet generator (nozzle) and a cooling system with the accuracy of temperature control equal 0.1 °C. The environmental temperature was adjusted to –10 °C during the ice accretion period and the performance of the tests.
2) High purity water (ASTM deionized distilled water D1193) was sprayed onto a cooled aluminium plate which was already held in a tensile test machine in the cold room to form a thin layer of ice.
3) The procedure was repeated to get the desired thickness of the ice sample. The grain size of ice samples made by this method was typically 1 mm.

The ice-making temperature was an important variable in these experiments, and the aluminium plate was held at the selected temperature (–10 °C) in the cold room for at least 1 hour before the ice-making process began. Then, the hydraulic water spray nozzle, fed with distilled and deionized water (ASTM deionized distilled water D1193), starts to spray super-cooled droplets. The water then dropped on the surface of the aluminium substrate and froze quickly to form a granular ice layer. The time required to make the ice samples varied according to the temperature and ice thickness, so the icing is stopped when the aluminium sample is covered with the desired thickness of ice. Each specimen was kept at the ice-making temperature for one hour before starting the test process. This time allows the internal stresses to relax before testing, so that no temperature disturbances appear at this juncture. After this time, the ice is strongly bonded to the aluminium plate. The experimental protocol and more details are presented in Appendix D.

Table 2.1: The experimental conditions of ice samples.

Parameters	**Units**	**Type -quantity**
Type of precipitations	___	Rain glaze
Water temperature, T_w	°C	$\cong 4$
Air temperature, T_a	°C	-10.0 ± 0.5
Type of water	___	Deionized
Jet edge	___	11001
Time of spray nozzle	sec	For opening = 0.4 For stopping = 0.9
Ventilator	Hz	40
Intensity of precipitations	mm/h	18

2.3 The setup

Figures 2.1 and 2.2 show a schematic and a photograph of the test device, respectively. The experimental setup consists of a press machine model *Applied Test system,* ATS 2500 which is placed horizontally in the cold room. The sample must be directly under the jets of freezing ice. The main components of the experimental setup for the traction test are illustrated in Figure 2.2. The main components of experimental setup in this figure are: the aluminium plate that is used as the ice-coated beam sample after ice accumulate (# 1) which is mounted in the grips of the testing machine (# 2, see also Figure 2.2 (b)) and subjected to centric tensile loading (# 3), applied steadily at constant rate of 0.05921 mm/s (M7 position of press machine ATS 2500) at a cold room with -10°C. A mould (# 4) is installed before icing to permit the accumulation of ice on the sample's surface only. A strain gauge (# 5, see also Figure 2.2 (c)) is attached to the back face of the sample, and the PC software Quick log starts to read the values of strain in a real time from the strain gauge. The testing procedure consists of applying successive increments of load while taking the corresponding extensometer reading of the elongation between two gauge marks on the sample. Also, a high speed camera (500 images per second) was used for the visual observation of cracking and de-icing.

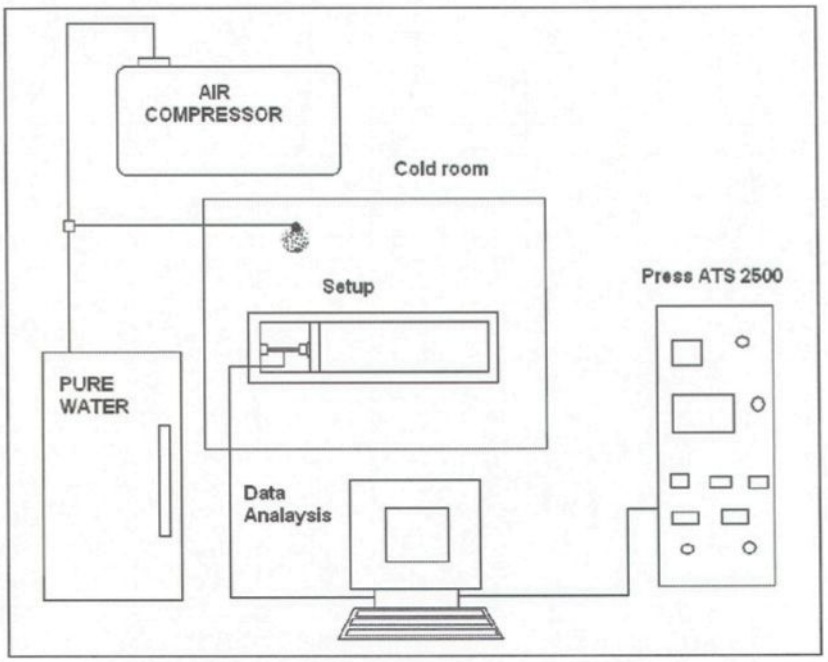

Figure 2.1: Schematic of tensile test device.

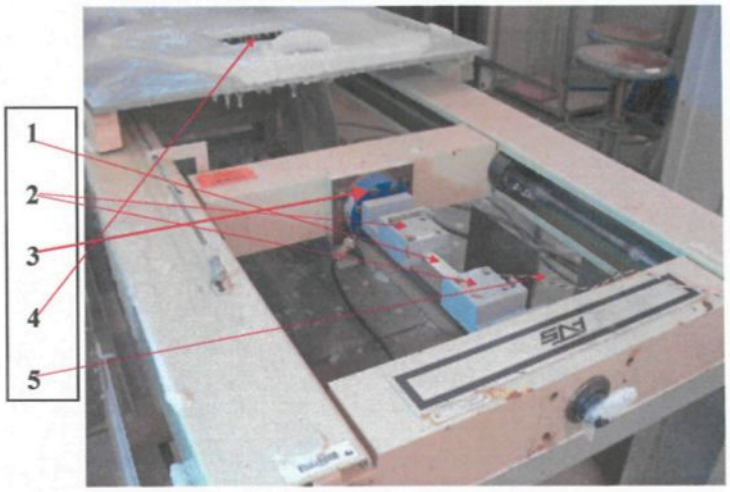

a):The setup with its main components.

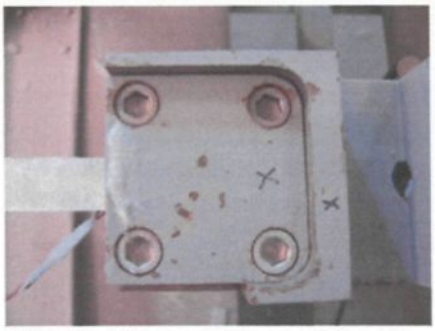

b): The grip (component #2).

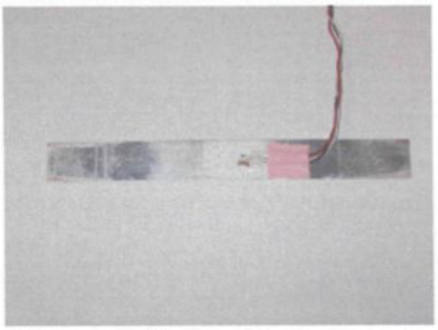

C): The strain gauge (component # 4)

Figure 2.2: Experimental setup.

Strain gauges are used to determine the state of strain existing at a point on a loaded member for the purpose of stress analysis. The strain is the change in a dimension brought about by load application, divided by the initial dimension, as shown in Figure 2.3:

$$\varepsilon_a = \frac{L - L_0}{L_0} \tag{2.1}$$

The tensile stress is measured as the force at any time divided by the original cross-sectional area of the waist portion in N/m^2, i.e.:

$$Tensile\ stress = \frac{force\ recorded\ at\ any\ time}{original\ waist\ cross\ sectional\ area}$$

The tensile strain is calculated as the ratio of the difference in length between the length marked by the gauge marks and the original length, *i.e.*

$$Tensile\ strain = \frac{Gauge\ length\ after\ extension}{Original\ gauge\ length}$$

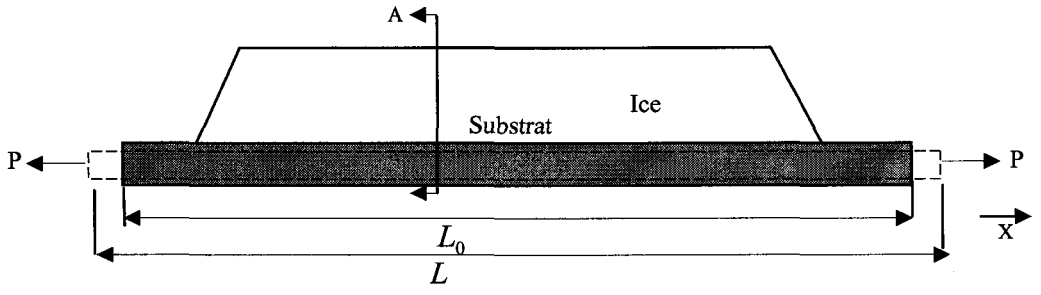

Figure 2.3: Relations for axial and lateral strains.

The related equations to determine the value of strain at failure for ice are presented in Table 2.2. In order to validate the measure of strain, firstly, it is assumed that just before the fracture of ice the value of strain in ice and aluminium are the same. In this

assumption, the measured value of strain for the uncovered part at each end of the substrate can be representative of that prevailing in the ice just before ice separation. The validity of this assumption depends mainly on the quality of the adhesion at the interface between the two materials. Here, it is assumed that the two materials are bonded completely. Secondly, it is assumed that the strain values remain constant throughout the length of ice-coated sample. Therefore, the measured strain during a tensile test can be represented by that being exerted in the middle of the sample (where the strain gage is located).

Using the relations for uniaxial condition such as they exist in a simple tensile test specimen, the complete stress-strain diagram can be determined for the material as described in Figures 2.4 to 2.6 for each thickness of ice. In these Figures, the dotted curve in dark blue is the average applied stress in function of the strain of the ice-coated sample. The strain values in the x axes are measured directly by the strain gauge, whereas the applied stress values in the Y axes are the applied load measured in the traction test divided by the section area of the aluminium plate. Generally, ice accumulation increases rigidity, because the deposit of ice increases the thickness. When the ice breaks or de-icing is occurred the rigidity decreases. This decreasing of rigidity appears with the change of the slope of graph. The slope can be changed gradually (Figure 2.4) or discontinuously with a jump (Figure 2.6). A gradual change of slope is interpreted as de-icing (ice removal) occurs slowly or there is simply ice breaking without de-icing. The break in slope is interpreted as ice removal (de-icing) occurs very fast.

Table 2.2: The related equations to determine the stress values.

Calculated Values	Equations	Parameters (Units)
$\sigma_{nominal}$, σ_0	$\sigma_0 = \frac{Pg}{b_{subst.} t_{subst.}}$	P = applied force (kg) $g = 9.82$ (m/s^2) $b_{subst.}$ = width of substrate (m) $t_{subst.}$ = thickness of substrate (m)
E	$E = \frac{\sigma_0}{\varepsilon_{measured}}$	$\sigma_{nominal}$ = nominal stress (MPa) $\varepsilon_{measured}$ =measured strain by gage
$\sigma_{ice\ fract.}$	If $\varepsilon_{ice} = \varepsilon_{substrate}$ $\sigma_{axial} \rangle\rangle \sigma_{lateral}$ $\sigma_{ice\ fract.} = \varepsilon_{fract} E_g$	E_g = 9000 (MPa) ε_{fract} = strain at fracture

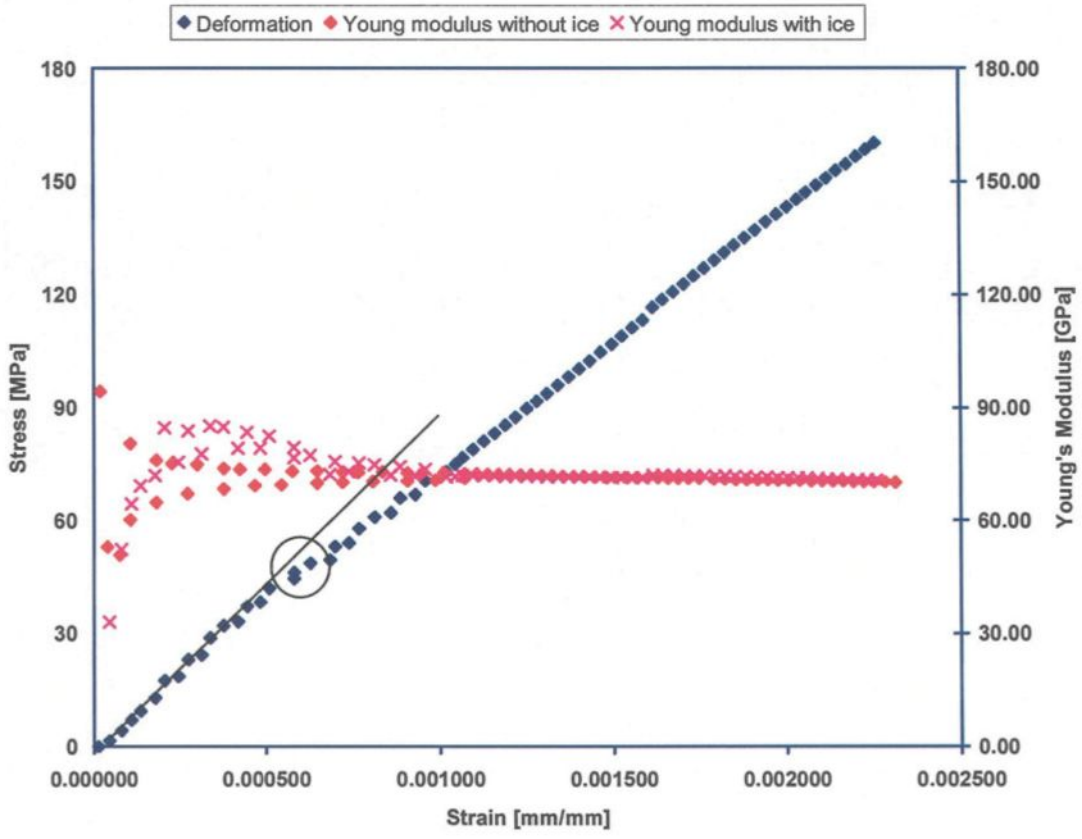

Figure 2.4: Experimental stress– strain curve for ice thickness 2 mm (test 1).

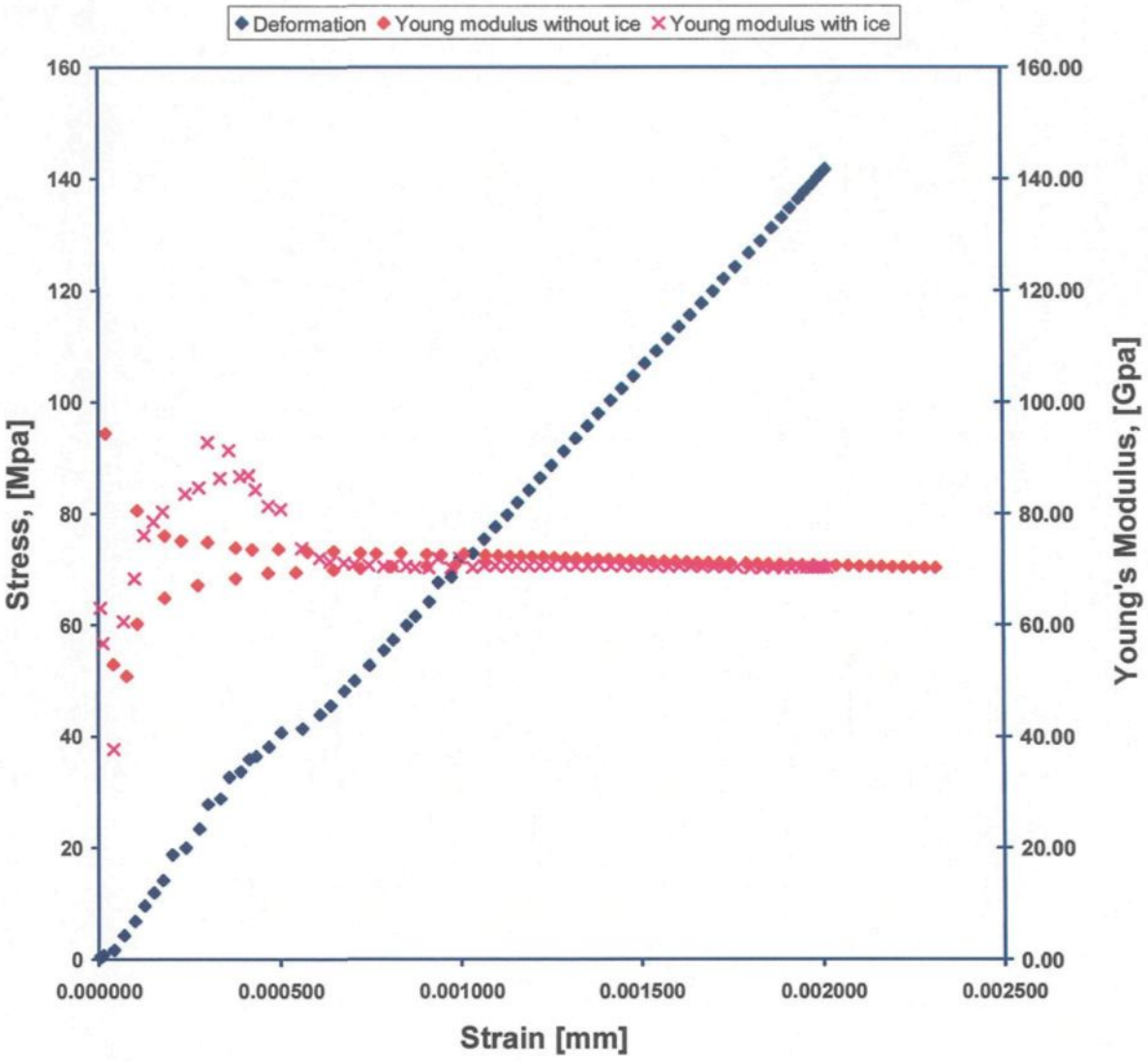

Figure 2.5: Experimental stress– strain curve for ice thickness 5 mm (test 6).

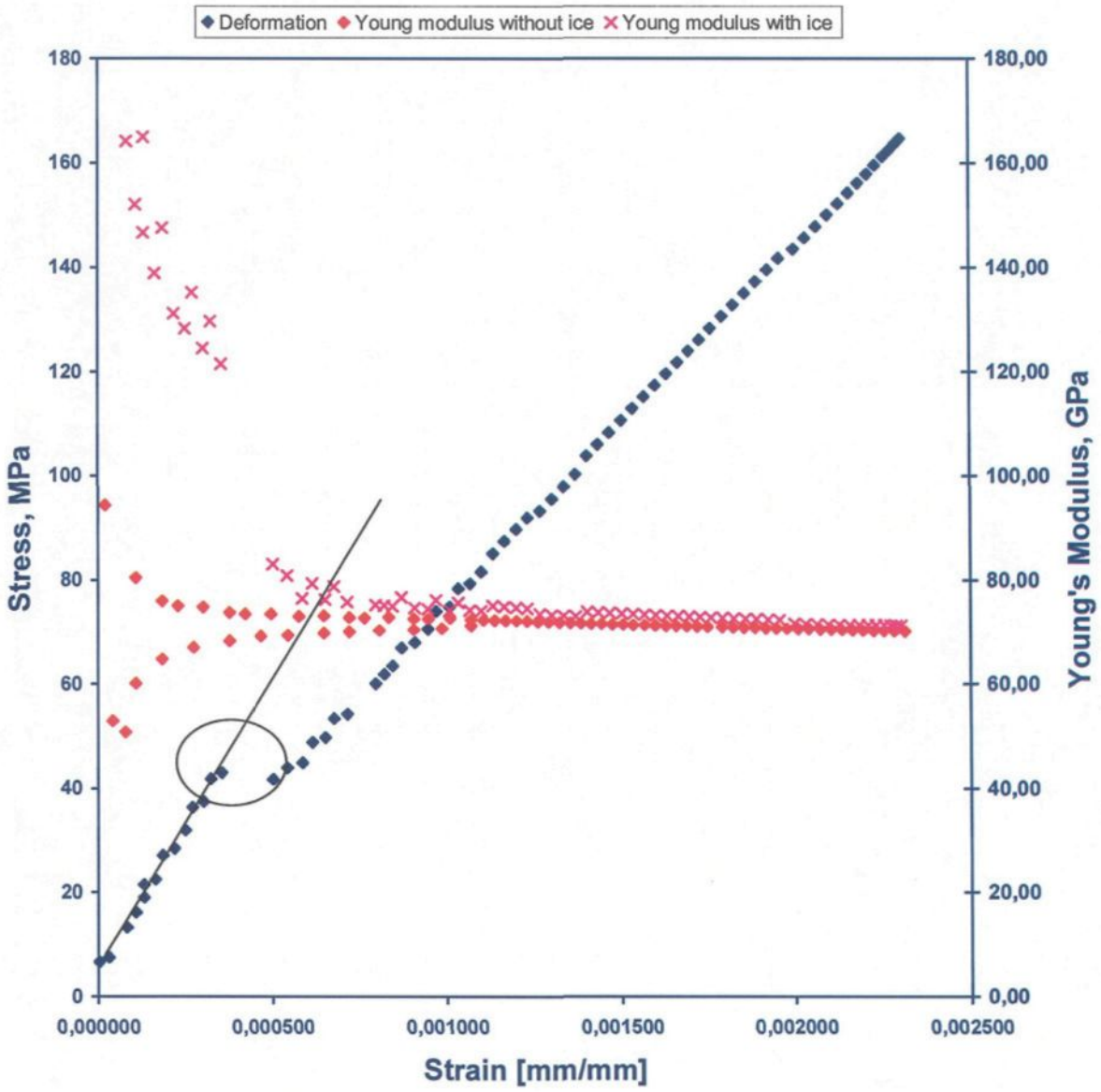

Figure 2.6: Experimental stress– strain curve for ice thickness 10 mm (test 9).

2.4 Test results and discussions

For each different thickness of ice, three tests were performed under the same conditions. The results of these tests show that:

1) In the case of the 2 mm thickness, the tensile stress imposed at the ice sheet generates the cracks perpendicular to the aluminium length, breaking it in pieces (see Figure 2.7 and ice failure is characteristic of a brittle failure. This mode of failure is expected, given the very fast deformation rate imposed, which is equal to a strain rate of about 2×10^{-4} mm/s. Also, the experiments show that when water is frozen on an aluminium surface which is completely wet, the interfacial forces for a thin thickness of ice are larger than the cohesive forces of the ice. For this reason, when the sample is stressed, the failure occurs in the ice; however, the form of the failure depends on the experimental configuration. If the ice is suitably constrained, if the tensile forces are spread over a large enough area so that the tensile stresses are small, the ice deforms plastically, the breaking force is proportional to the number of degrees of frost, and if the tensile stress is large compared with the shear forces (as our tests), a brittle fracture takes place and the breaking force is dependent on the thickness of ice. The results show that with the thickness of ice equalling 2 mm, the interface is stronger than the ice and cracks are created in the ice sheet. In other words, corresponding to a thin thickness of ice, the surface molecules are more susceptible to breakage than bulk and interface molecules, which means in this case the cohesive failure (Failure occurs within ice itself) is more probable than adhesive failure (failure of the bond between the adhesive and substrate surface).

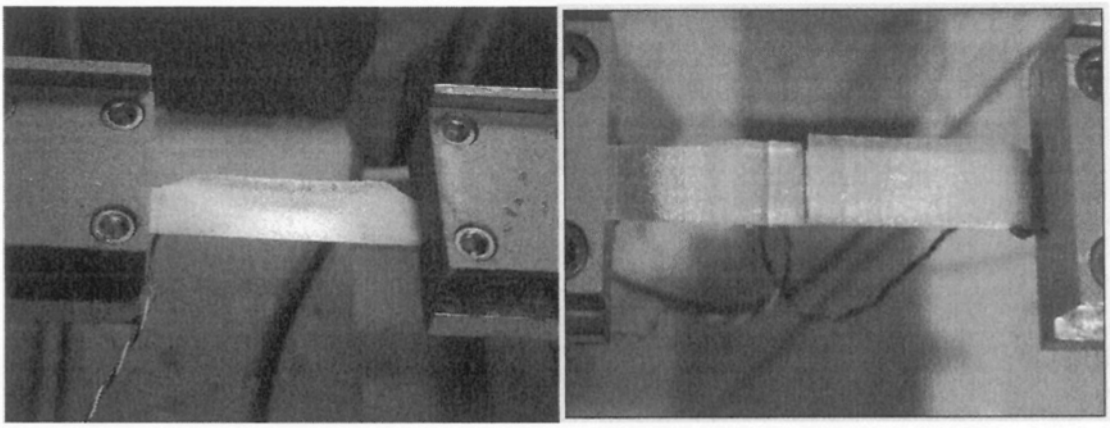

a): Ice-coated beam sample before testing. b): Ice-coated beam sample after testing.

Figure 2.7: Description of the tensile test.

2) In the case of the 5 mm thickness, it can be observed that not only ice fracture (cohesive failure) but also ice removal (adhesive failure) occurs. In this case, a transition is observed from cohesive to adhesive failure, and a significant proportion of specimens exhibited some regions of interfacial separation in this thickness range.

3) In the case of the 10 mm thickness, ice de-bonds without breaking the ice sheet (cohesive break). In this case, the ice is stronger than the interface and ice removal occurs without cracking the ice. In other words, the crack extended along the interface and the bonding was broken by an adhesive separation. The results obtained in these nine tests are presented in Table 2.3. Also, the force versus strain graphs for tests number 2, 6 and 9 are shown in Figures 2.8, 2.9 and 2.10 respectively (the results from these three tests will be used for the numerical model).

Table 2.3: Tensile test data.

Test	Ice thickness (mm)	Strain (mm/mm)	Force (N)	Normal stress at bottom face in Al (MPa)
1	2.61	0.000508	340.01	35.56
2	1.97	0.000529	343.35	37.03
3	3.29	0.000570	369.83	39.9
4	6.59	0.00052	373.27	36.4
5	5.56	0.00040	310.97	28.0
6	5.35	0.000503	329.20	35.21
7	9.98	0.000299	372.87	20.93
8	10.09	0.000354	348.25	24.78
9	10.09	0.000375	297.63	26.25

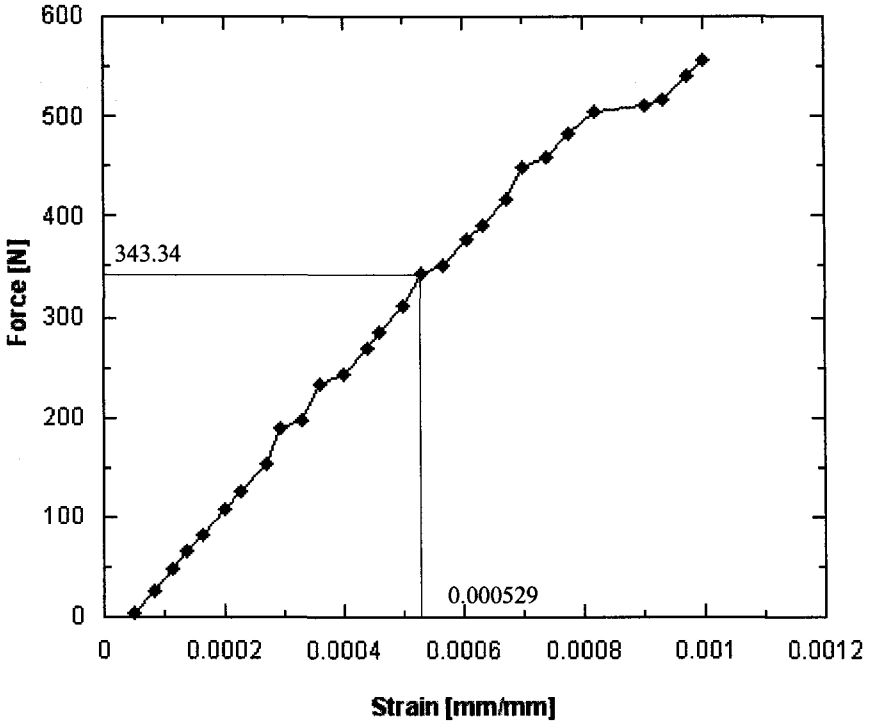

Figure 2.8: Experimental force – strain curve for ice thickness 2 mm.

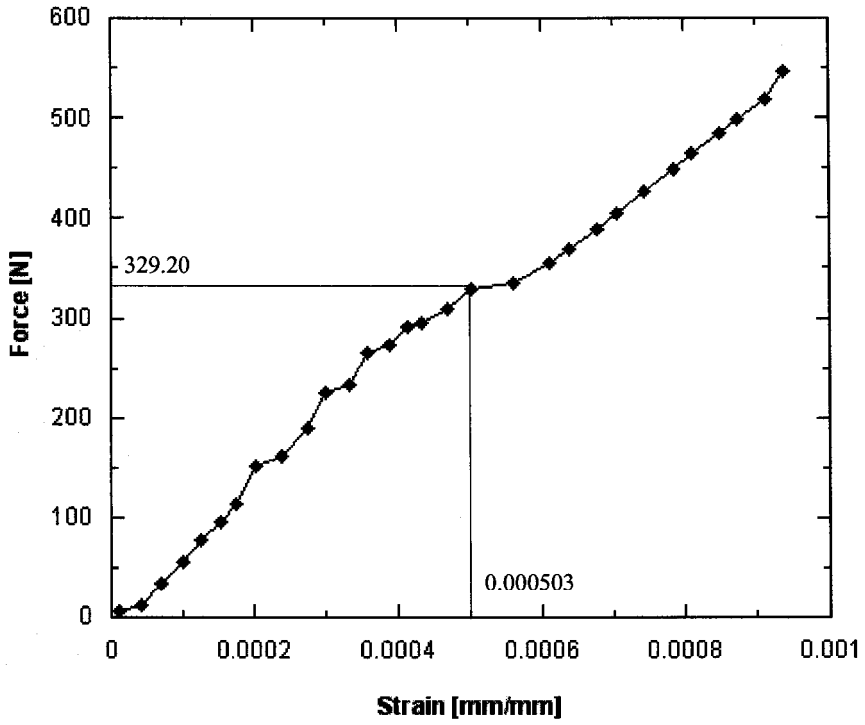

Figure 2.9: Experimental force – strain curve for ice thickness 5 mm.

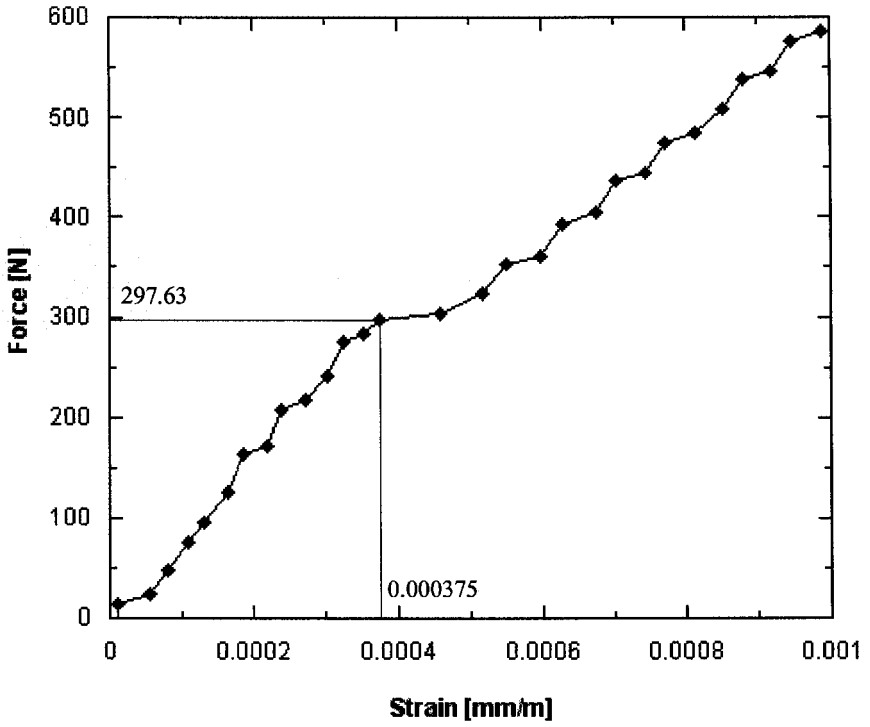

Figure 2.10: Experimental force – strain curve for ice thickness 10 mm.

CHAPTER 3

THEORY AND MATHEMATICAL MODEL FOR ICE AND INTERFACE

CHAPTER 3

THEORY AND MATHEMATICAL MODEL FOR ICE AND INTERFACE

3.1 General

Mathematical modeling can be used to represent some phenomena in order to gain a better understanding of that phenomenon by exhibiting a designated similarity to physical objects. A mathematical model attempts to match observation that uses mathematical equations. When a model is developed and it is used to answer questions, it should be examined, and often modified, to obtain a more accurate response of the observed reality of that phenomenon. In this way, mathematical modeling is a developing process, and each real-world phenomenon can be represented by using theoretical, mathematical, and computational models together. In order to describe the stress-strain behaviour of ice on the substrate under tension loading, a model will be developed to improve our understanding of the mechanisms of ice/substrate interface underlying the mechanical properties of ice. This chapter first presents a mathematical model based on classical beam theory, and then describes the two proposed constitutive laws for ice and interface in detail, respectively: a *brittle cracking* constitutive law, which has been developed basically for concrete and can be used for the other brittle materials such as

ice, and a *cohesive material* constitutive law which predicts the initiation as well as evolution of damage to the interface.

3.2 The classical linear beam theory

In order to define a simplified mathematical model, the ice mass on the aluminium plate can be assumed to be a composite material. Using the elastic properties of each material, the equations are defined considering an equivalent material. The free-body diagram of the model is shown in Figure 3.1. From this theory, we can develop the following relations.

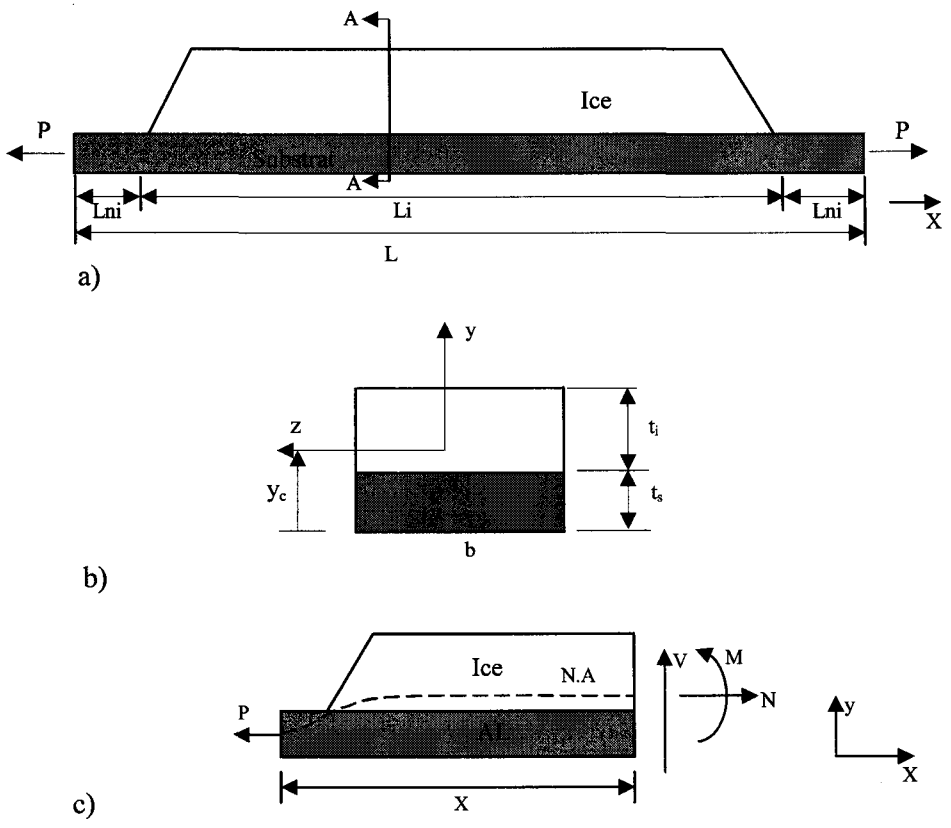

Figure 3.1: Free-body diagram of the theoretical model. a) Description of the geometry, b) Description of section A-A, c) Equilibrium of the beam system.

A formula for normal stress is [98]:

$$\sigma_x = -\frac{My}{I} \tag{3.1}$$

where M and I are the bending moment and the moment of inertia respectively. Usually called the elastic bending formula, this important equation shows that the stresses vary linearly with the distance (y) from the neutral axis. For combined normal force and bending, the axial stress is given by:

$$\sigma_x = \frac{P}{A} - \frac{My}{I} \tag{3.2}$$

The maximum stress $\sigma_{\max}$ occurs at the outermost fibres of the beam. Since at a given section, M and I are constant,

$$\sigma_{\max} = \frac{Mc}{I} = \frac{M}{S} \tag{3.3}$$

where $c = |y_{\max}|$, and $S = \frac{I}{c}$ is called the elastic section modulus of the beam. For a beam of rectangular cross section with width b and height h, we have:

$$I_z = \frac{bh^3}{12}, S = \frac{bh^2}{6} \tag{3.4}$$

The substrate covered by ice can be assumed to be a composite material. The materials having different modules of elasticity must be combined as unique materials with the balance coefficient (n) such that:

$$n = \frac{E^{al}}{E^{ice}} \tag{3.5}$$

If I^{ice} and I^{al} represent the moments of inertia about the neutral axis of the cross-sectional areas ice (A^{ice}) and aluminium (A^{al}), respectively, it is convenient to define a combined inertia and total area given by:

$$I^t = I^{ice} + nI^{al}, \tag{3.6}$$

$$A^t = A^{ice} + nA^{al} \tag{3.7}$$

The flexure formulas now are given by:

$$\sigma_x^{ice} = \frac{-P}{A^t} - \frac{My}{I^t}, \quad \sigma_x^{al} = n\sigma_x^{ice} \tag{3.8}$$

where σ_x^{ice} and σ_x^{al} are the stresses in materials ice and aluminium, respectively.

In the iced composite beam solicited in flexion by a bending moment $M = force \times eccentricity$, the value of shear stress τ at the aluminium interface can be calculated from the applied shear force V. The value of shear flux due to the variation of the bending moment (see Figure 3.1(c) and 3.2) is given by:

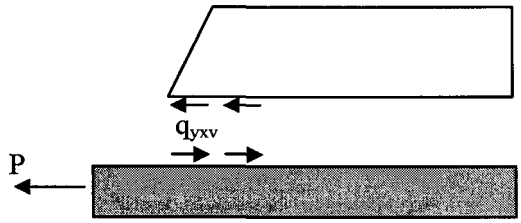

Figure 3.2: Description of shear flux due to the variation of the bending moment.

$$q_{yxv} = \frac{VQ}{I^t} \tag{3.9}$$

where

$$V = -\frac{dM}{dx} \tag{3.10}$$

and

$$Q = t_{ice}\, b_{ice}\left(t_{al} + \frac{t_{ice}}{2} - y\right) \tag{3.11}$$

And from equilibrium at interface:

$$N_{ice} - \int_0^{\frac{L}{2}} q_{yxe} dx - \int_0^{\frac{L}{2}} q_{yxv} dx = 0,$$

$$N_{al} - P + \int_0^{\frac{L}{2}} q_{yxe} dx + \int_0^{\frac{L}{2}} q_{yxv} dx = 0 \qquad (3.12)$$

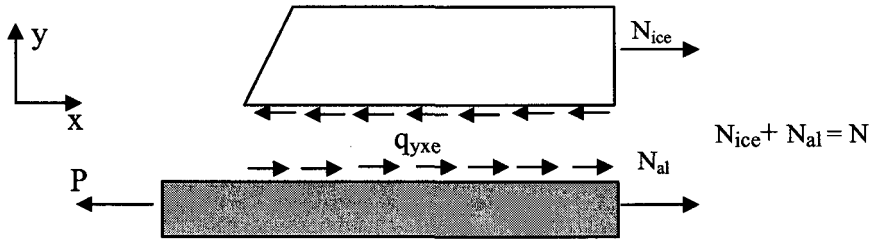

Figure 3.3: Description of equivalent shear flux.

Considering the assumption that the equivalent shear flux is uniform on the mid-length:

$$q_{yxe} = \frac{2}{L}\left(N_{ice} - \int_0^{\frac{L}{2}} q_{yxv}\, dx \right) \qquad (3.13)$$

and the values of shear stress τ at ice and aluminium interfaces are given respectively by:

$$\tau_{ice} = \frac{qyx}{b} \quad , \quad \tau_{al} = \frac{\tau_{ice}}{n} \qquad (3.14)$$

Equations 3.1 to 3.14 have been implemented in the numerical software Maple to determine the normal stress and shear stress distribution in accordance to the linear elastic theory. Figure 3.4 shows the normal stress distribution at mid-length for the three thicknesses of ice considered in the experimental setup and for an external applied force corresponding to the point of fracture as shown in Figures 2.8 to 2.10.

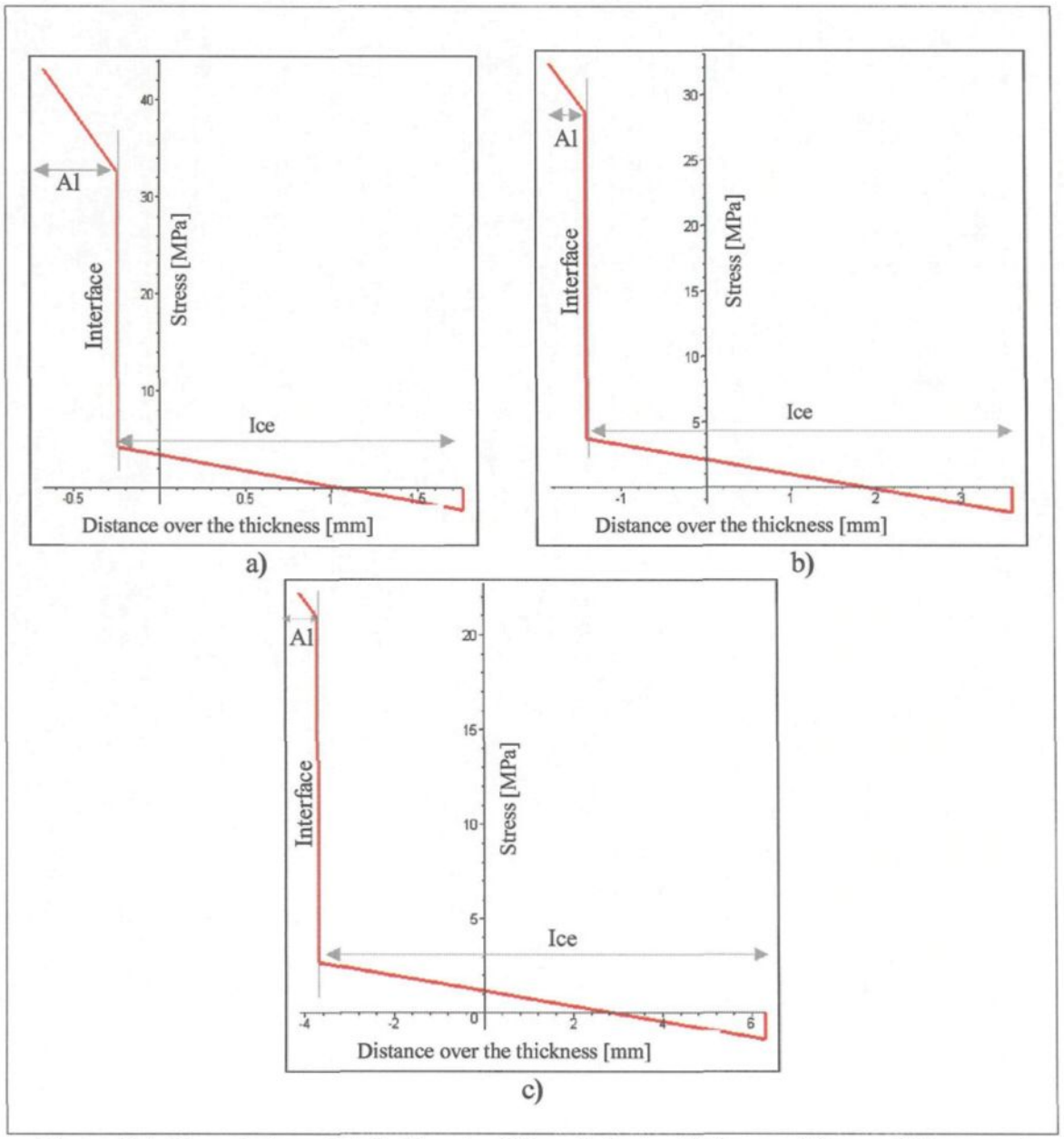

Figure 3.4: Normal stress distribution at mid-length for ice thickness: a) 2 mm, b) 5 mm and c) 10 mm.

The longitudinal shear stress distributed through the thickness of ice is shown in Figure 3.5:

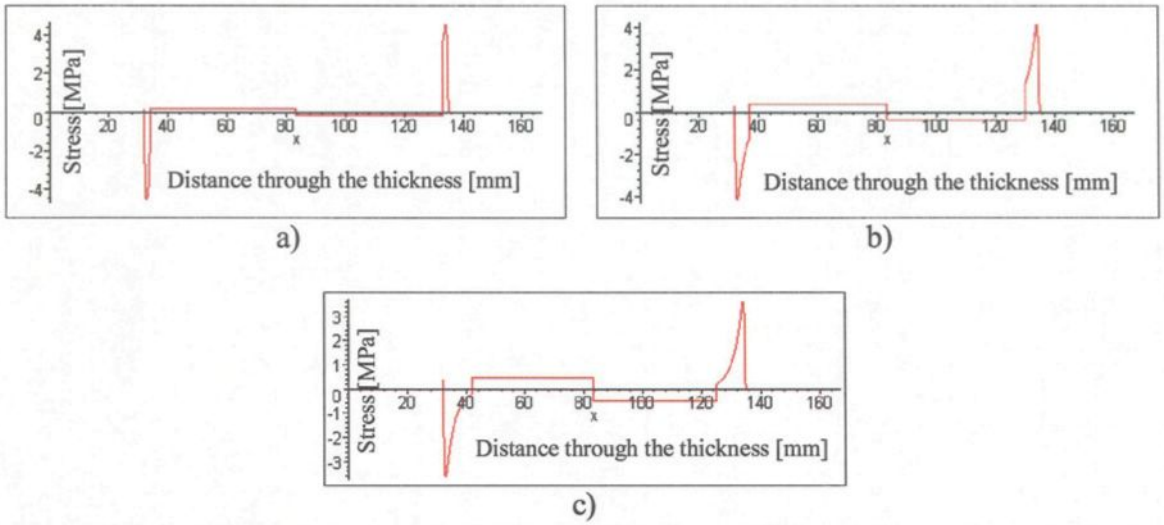

Figure 3.5: Longitudinal shear stress distribution through the thickness of ice: a) 2 mm, b) 5 mm and c) 10 mm.

In Table 3.1 a comparison between experimental and mathematical models (Maple) shows that realistic stress distribution cannot be evaluated using the linear description of the strain tensor. This is mainly due to the small thickness of the aluminium plate. Also, another argument is that the shear and normal stresses at the interface of the ice/aluminium have a complex distribution which cannot be demonstrated by using the classical beam theory. The beam theory also leads one to believe that the interfacial longitudinal shear stresses can be calculated using the elementary shear stress equations given in strength of material books (Eq. 3.14). In reality, these stresses have a much more complex distribution. Furthermore, when the ice on an aluminium plate cracks, the stresses at the interface in the neighbourhood of the crack deviate significantly from the distribution predicted by simple beam theory or by any other theory that ignores the

presence of cracks. The experimentally observed delamination of ice on aluminium substrate is caused by the combined effect of these high interfacial stresses.

Table 3.1: Comparative results between the experimental and the mathematical models.

Thickness (mm)	Force (N)	Normal stress σ_{xx} at bottom face in Al (MPa)		Longitudinal shear stress (S_{xz}) through the ice (MPa)	
		Experimental	Theoretical	Theoretical	Experimental*
2	343.35	37.03	43.27	4.53	0.47± 0.06
5	329.20	35.21	32.44	4.16	
10	297.63	26.25	22.27	3.62	

* This average value was obtained from centrifuge test by C. Laforte in LIMA laboratory.

However, there are many theories proposed to understand the complex behaviour of fracture in the material. One such class of theories, which involved energy concepts, was developed by Griffith, who recognized that the macroscopic potential energy of the system consisting of the internal stored elastic energy and the external potential energy of the applied loads, varied with the size of the crack [95]. Based on the Griffith theory, fracture is associated with the consumption of energy:

$$U = U_0 - U_a - U_\gamma \tag{3.15}$$

where U is the total potential energy of the system, U_0 is the elastic energy of the un-cracked plate, U_a is the decrease in the elastic energy caused by introducing the crack in the plate and U_γ is the increase in the elastic-surface energy caused by the formation of the crack surface [95].

3.3 Model for the ice

3.3.1 Introduction

The failure mode of ice is dependent on at least four parameters: temperature, porosity, grain size and strain rate. Here, it is focused on the strain rate effects, because our experimental tests were performed at a high strain rate. The scope of the problem is that a brittle failure mode will occur when the strain rate is higher than $10^{-3}s^{-1}$ and a ductile failure mode will dominate when the strain rate is lower than$10^{-3}s^{-1}$[25]. At strain rates below $10^{-5}s^{-1}$ in tension and $10^{-4}s^{-1}$ in compression, ice deforms mostly by creep. At higher strain rates, ice deformation is mostly elastic because it takes time to develop creep deformation, and the failure of ice specimens is by fracture [25]. Figure 3.6 shows the schematic effect of strain rate on the tensile and compressive stress-strain behaviour of ice. At low rates of deformation, cracks do not form, and the material has a ductile behaviour (Figure 3.6 - curves I). At high rates, cracks do initiate, and the material has a brittle behaviour (Figure 3.6 - curves III) independent of stress state. At intermediate strain rates, cracks also develop, and the behaviour of material is brittle under tension (Figure 3.6 - curve TII) but ductile under compression (Figure 3.6 - curve CII). At lower strain rates the ductile-brittle transition occurs under tension because the applied stress opens the cracks directly [83]. Figure 3.7 shows the tensile and compressive strengths of fresh-water ice of about 1 mm in grain size versus strain rate loaded uniaxially at temperatures around -10°C. For ice deformed under these conditions, the low strain rate is less than $10^{-7}s^{-1}$ and the high strain rate is greater than $10^{-3}s^{-1}$[83].

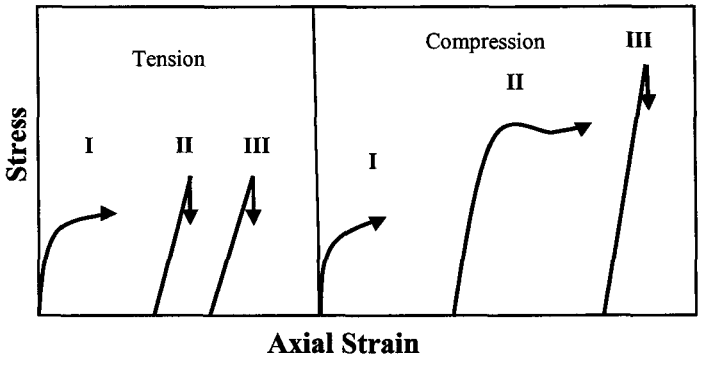

Figure 3.6: Schematic effect of strain rate on the tensile and compressive stress-strain behaviour of ice. I, II, and III denote low-, intermediate-, and high-strain rates respectively [83].

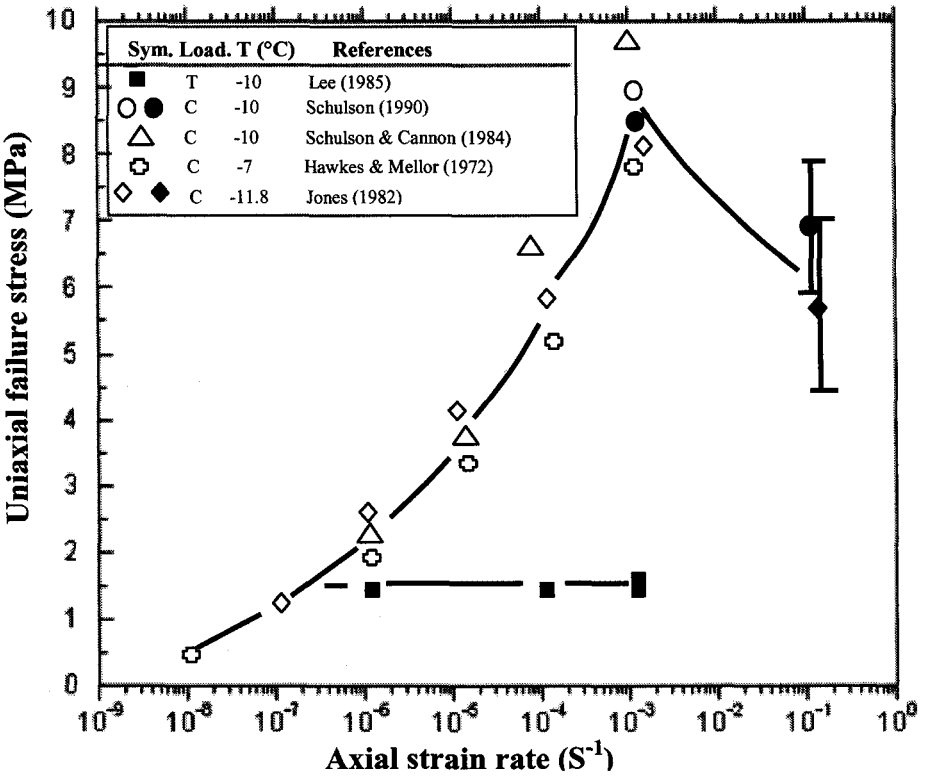

Figure 3.7: Graph demonstrating the effect of strain rate on the uniaxial compressive strength (C) of equiaxed and randomly oriented polycrystals of ice Ih of 1 mm grain size at −10°C. The tensile strength (T) is shown for comparison. The peak in the compressive strength versus strain rate marks the macroscopic ductile-to-brittle transition [83].

In the range of the average loading rate in our experiments ($\approx 10^{-4} s^{-1}$), ice has a brittle behaviour. This behaviour will be explained in this section.

The most commonly-used method to calculate stresses from a structural engineer's point of view is the theories from strength of materials. The mechanical engineer is able to look at the microstructure of the failure process, and if there are cracks in the failure one may try to use the linear elastic fracture mechanics (LEFM) approach. This approach will be illustrated in this section in order to describe the parameters, the critical stress intensity factor K_{Ic}, and the energy release rate G for using a brittle cracking ice model.

3.3.2 Brittle behaviour of ice under tension

At higher strain rates under tension (regimes TII & TIII, Figures 3.6 and 3.7) ice breaks after lengthening 0.01-0.1% through transgranular cleavage, at an applied stress around 1 MPa [23, 42, 72, 84 and 85]. As described in section 1.3.2, the tensile strength of ice is essentially rate independent and slightly dependent on temperature, increasing by less than 25% upon decreasing temperature from -5°C to -20°C. Also, the tensile strength decreases with increasing grain size [83]. The tensile behaviour of ice has been described and modeled in the nucleation and growth of cracks (propagation) terms. Their resistance to propagation is controlled by the fracture toughness of the material. Therefore, within finely grained size (around 1-2 mm), cracks are shorter upon nucleation than the critical size, so the tensile strength is limited by crack propagation. With more coarsely-grained ice, the cracks propagate immediately based on nucleation. The significance is that the tensile strength of the cracked ice is controlled by crack propagation [85]. Apart from cracks, grain size has the largest effect on tensile strength of ice. For example, by

decreasing the grain diameter d from 10 to 1mm, the strength σ_t increases by about a factor of 2 as illustrated in Figures 3.8 (b) and 3.8 (c).

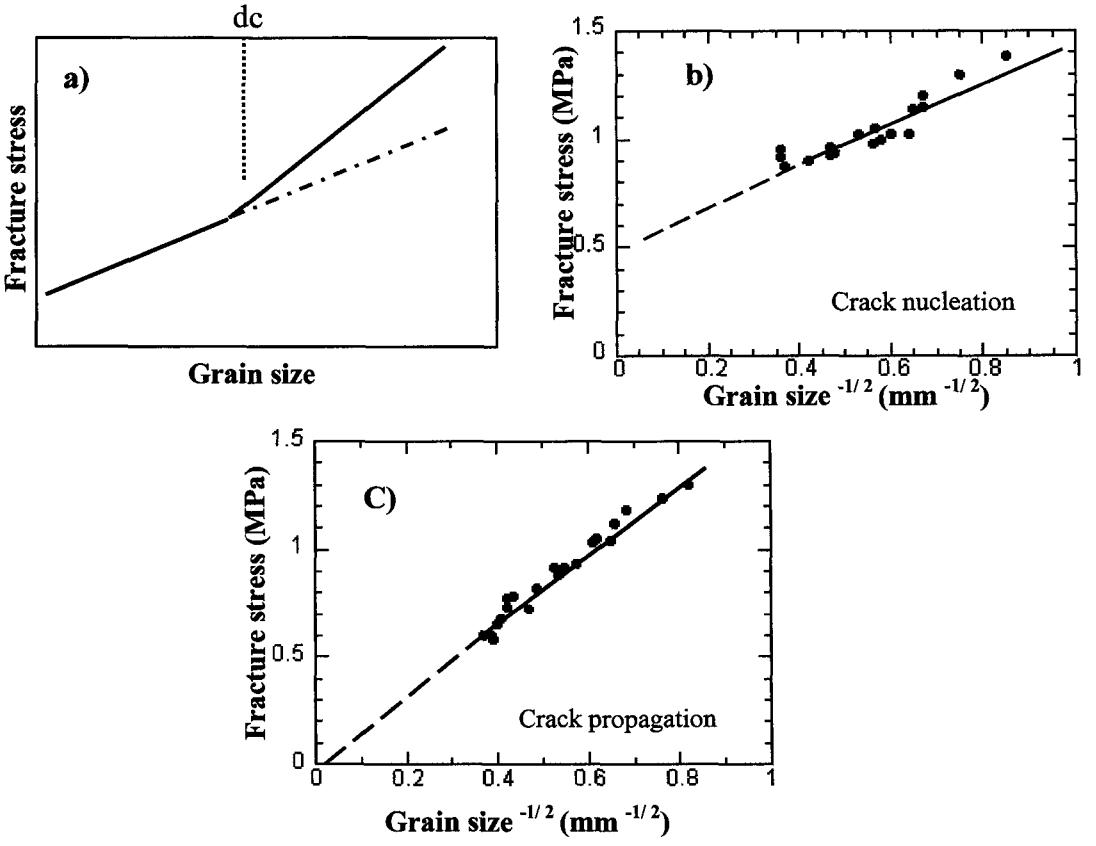

Figure 3.8: Graphs of tensile fracture stress versus $(grain\ size)^{-0.5}$ of equiaxed and randomly-oriented aggregates of fresh-water ice Ih loaded under uniaxial tension: a) showing schematically the critical grain size, dc, below which the material exhibits a minor amount of inelastic deformation that increases with decreasing grain size; b) showing that at −10°C at a strain rate of $10^{-3}s^{-1}$, where dc <1.4 mm, the strength is controlled by crack nucleation; and c) showing that at −10°C at a strain rate of $10^{-7}s^{-1}$, where d_c〉 6.7 mm, the strength is controlled by crack propagation [87].

The relationship is either [87]:

$$\sigma_t = \sigma_0 + k_t d^{-0.5} \text{ (for d > d}_c\text{)} \tag{3.16}$$

or

$$\sigma_t = Kd^{-0.5} \text{ (for d < d}_c\text{)} \tag{3.17}$$

where σ_0, k_t and K are material constants and d_c is critical grain size. Values at -10°C are σ_0 = 0.6 MPa, k_t = 0.02 MPa$\sqrt{m}$ and K = 0.044 MPa$\sqrt{m}$, with increasing strain rate, d_c decreases from > 6.7 mm at 10^{-7} S $^{-1}$ to 1.6 mm at 10^{-6} S $^{-1}$ and to < 1.4 mm at 10^{-3} S $^{-1}$ [85 and 86]. According to the concept of brittle fracture and the mechanisms underlying Equations (3.16) and (3.17), critical grain size d_c, is given by :

$$d_c = \left(\frac{K - k_t}{\sigma_0}\right)^2 \tag{3.18}$$

3.3.3 The brittle cracking theory

The cracking constitutive model for ice and other brittle materials is described in this section. As aforementioned, it is generally accepted that ice exhibits two primary modes of behaviour:

1) A brittle mode that is associated with cleavage, shear and mixed-mode fracture mechanisms that are observed under tension and tension-compression states of stress. It almost always involves softening of the material.
2) A ductile mode that is associated with distributed microcracking mechanisms that are primarily observed under compression states of stress. It almost always involves hardening of the material.

The cracking model that is described here models only the brittle aspects of ice behaviour. The brittle cracking model is used for applications in which the material behaviour is dominated by tensile cracking and compressive failure is unimportant.

3.3.3.1 Fracture mechanics of brittle materials based on linear elastic fracture mechanic (LEFM)

As described briefly in section 1.3.4 (a history of fracture mechanics of brittle materials) in LEFM, crack growth is defined by the energy release rate G and stress intensity factor K_I (index I related to mode I). To define these variables, a crack of length 2a, which extends right through an infinite elastic flat plate with dimension D and small thickness b (see Figure 3.9) is considered. From equilibrium, compatibility and the linear elastic constitutive law (the material is assumed as linear elastic), the stress distribution in the uncracked part of the panel is [13]:

$$\sigma_{22} = \sigma_n \frac{|x_1|}{\sqrt{x_1^2 - a^2}} \tag{3.19}$$

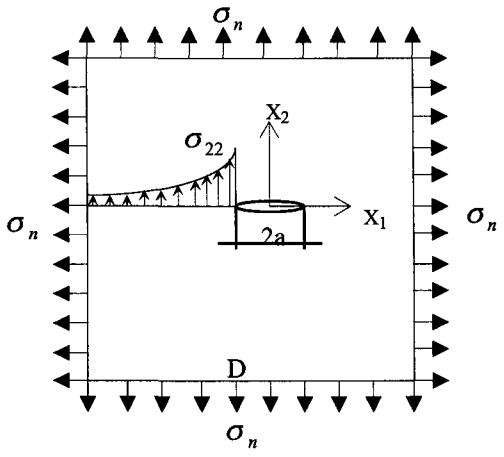

Figure 3.9: Multiaxial stressed panel with thickness b and width D, and a predefined crack width 2a [13].

If we then let the distance $x_1 - a \langle\langle a$, then the stress intensity factor, K, which defines the magnitude of the local stresses around the crack tip as:

$$K_I = \sigma_n \sqrt{\pi a} \tag{3.20}$$

This intensity factor depends on loading, crack shape, crack size, and geometric boundaries. The stress distribution in the intact panel is given by:

$$\sigma_{22} = \frac{K_I}{\sqrt{2\pi r}} \tag{3.21}$$

where r is equal to $x_1 - a$.

To define the energy release rate parameter G, the relation between the energy release rate and the stress intensity factor K_I is called Irwin's formula, and derivations are shown in many fracture mechanics textbooks [13]. Here we only consider the result of the derivations; the famous Irwin's formula is:

$$G = \frac{K_I^2}{E} \tag{3.22}$$

where E is the elastic modulus.

Let us now turn to the local crack growth in Mode I. Since intensity factor K_I only determines the stress state of the material in the crack tip (a very small fracture process zone), the crack will propagate when this stress intensity factor reaches a critical value, K_{Ic}, called fracture toughness [3]. According to the fundamental relationship (Eq. 3.22), K_{Ic} is related to the fracture energy by:

$$K_{Ic} = \sqrt{E G_f} \tag{3.23}$$

where the index f on G will be used when the fracture is considered.

It is quite hard to get a good value of K_{Ic} for ice. The typical values of K_{Ic} are in the range of 80 - 120 $kPa\ m^{1/2}$ for pure ice. The mean values obtained by different authors

for the critical stress intensity factor K_{Ic} and corresponding G_f values are presented in Table 3.2. In Appendix A, the mixed-mode bending (MMB) test is analyzed using beam theory to calculate the mode I and mode II components of strain energy release rate, G_I and G_{II} respectively.

Table 3.2: Fracture toughness and critical stress intensity factor for ice [96].

Authors	**Temperature T °C**	**Critical stress intensity factor K_{IC}** $KN.m^{-3/2}$	**Fracture toughness G** Jm^{-2} **or** $\frac{N}{m}$
Goodman	-11	119 ± 34	1.45± 0.83
Goodman and Tabor (1978)	-13	116 ± 13	1.41± 0.31
Liu and Miller (1979)	—	108 ± 10	1.471± 0.27
Gold (1963)	-16.7	94 -110	0.923 - 1.53

3.3.3.2 Determining the fracture energy of interfaces

The fracture mechanics approach is ideally suited to the interfacial failure subjects, and has interested many researchers in mechanics and materials science [30, 47, 49, 76, 79, 94 and 99]. In the last decade, interface fracture mechanics has been the object of significant development and which can be applied to the ice/solid interface adhesion problem. It should be noted that the crack growth of bi-material interface cracks like ice/solid interface is always mixed-mode because of the mismatch of material properties across the interface. The fracture of bi-material interfaces can be characterized by two parameters: the fracture energy G_f, and the phase angle ψ [30]. As aforementioned, the fracture energy G_f can be obtained via the energy release rate calibration of test

specimens or can be calculated from the critical stress intensity factor K_{IC} (Eq. 3.23). The phase angle ψ is a measure of the mixity of shear-to-opening experienced by an interface crack surface, and can be determined either from finite element calculations or by using integral equation methods. The sign and magnitude of ψ are of particular significance in determining whether a propagating crack can extend along the interface or kink into one of the composite constituents [101]. Obviously, performing standard shear, tensile, or impact tests is not sufficient to characterize the failure of ice/solid interfaces. This work attempts to utilize fracture mechanics to characterize the failure of ice/aluminium adhesion.

Various methods exist to characterize the fracture energy of interfaces [30]. Charalambides et *al* developed a four-point bending delamination specimen (see Figure 3.10) to determine the critical energy release rate at the bimaterial interface. The method of Charalambides et *al.* has the advantage of being able to simulate icing on the surface of structures on the simple sample geometry. This method has been described in Appendix c.

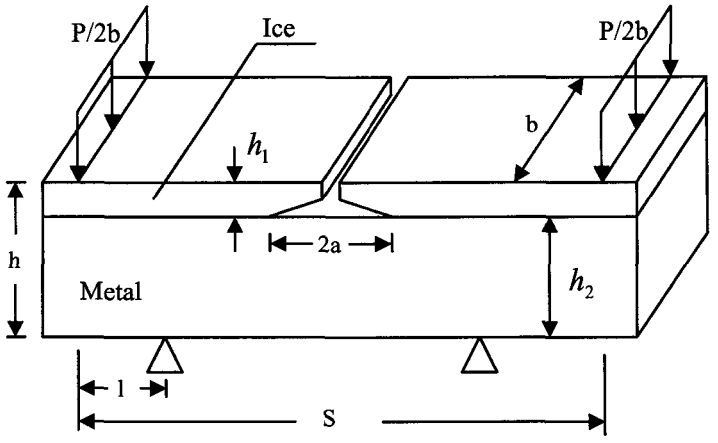

Figure 3.10: Four-point bending specimen geometry and loading configuration.

The phase angle ψ of this configuration is in the range of 35°- 60° [47]. This method was used by Wei et *al* [101], in order to characterize the failure of ice/solid adhesion. On the base of the Euler-Bernoulli beam theory, the critical interface fracture energy G_f is:

$$G_f = \frac{M_f^2(1-\upsilon_2^2)}{2E_2}\left(\frac{1}{I_2} - \frac{\lambda}{I_c}\right) \tag{3.24}$$

where

$$\lambda = \frac{E_2\left(1-\upsilon_1^2\right)}{E_1\left(1-\upsilon_2^2\right)},\quad M_f = \frac{Pl}{2b},\quad I_2 = \frac{h_2^3}{12} \tag{3.25}$$

The bending moment M_f exists along the sample cross section. I denotes the moment of inertia, the subscripts 1 and 2 refer to the ice and substrate materials respectively, and subscript c refers to the composite beam. It should be noted that this approach is valid when the crack length must be significantly larger than the thickness of the upper layer. Table 3.3 gives the values of fracture energy for different ice/metal interfaces tested by Wei et *al.* [101].

Table 3.3: Fracture energy of ice/metal interfaces (a/l = 0.5) [101].

Interface type	**Relative thickness** $\frac{h_1}{h_2}$	**Relative modulus** $\frac{E_2}{E_1}$	**Fracture energy** G_f (Jm^{-2} or $\frac{\mathrm{N}}{\mathrm{m}}$)
Ice/Al	0.8	7.1	1.0
Ice/steel	1.0	20.4	1.1

Analytical results [22] show that the fracture energy G_f increases monotonically when the relative upper beam thickness h_1/h_2 increases and decreases when the relative modulus of the lower layer E_2/E_1 increases. Also, it should be noted that the fracture

energy of ice/metal interfaces is affected by the ice type and the procedure of ice formation on substrate [101].

3.3.3.3 Analysis of crack formation and crack growth in ice

Recently, the development of finite element methods (FEM) and fracture mechanics have now given us the possibility of analysing crack growth. While the fundamental rules for crack propagation come from the fracture mechanics approach (*e.g.* the energy balance approach), FEM makes it possible to apply these rules to complicated cases.

As aforementioned, in the energy balance approach it is assumed that a certain amount of energy, G_f, is absorbed by the formation of a unit area of the crack surface. The crack propagates when a certain amount of stored energy is released and this released energy is equal to or greater than the absorbed energy. FEM can be used to determine the energy release rate in the energy balance approach. This enables the use of a FEM mesh with rather large elements. The formation of cracks cannot be explained with this energy balance approach [44].

The crack is assumed to propagate when the stress at the crack tip reaches the tensile strength f_t. When the crack opens, the stress is not assumed to fall to zero immediately, but the stress decreases with increasing crack width δ . As shown in Figure 3.11 at the crack width δ_c, the stress reaches zero. Where $\delta < \delta_c$, the crack in reality corresponds to a micro-cracked zone with some remaining ligaments for stress transfer. As there is a stress to be overcome in opening the crack, energy is absorbed. The amount

of energy absorbed per unit crack area in widening the crack from zero to or beyond δ_c corresponds to the area between the curve and the coordinate axis in Figure 3.11 is:

$$\int_0^{\delta_c} \sigma \, d\delta = G_f \tag{3.26}$$

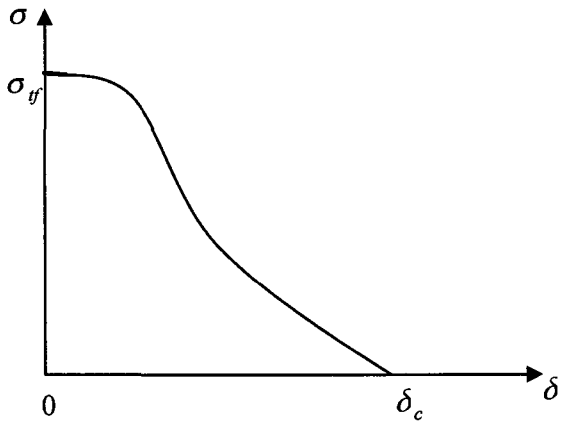

Figure 3.11: General case of assumed variation of stress σ with crack width δ .

The σ - δ curve (see Figure 3.11) may be chosen in various shapes, *e.g.* according to Figures 3.12 (a), (b) or (c), which all show simple mathematical relations. For typical yielding materials, like mild steel, Figure 3.12 (a) seems to be the best choice while Figure 3.12 (c) is the best choice for concrete material [44]. For the ice we consider the simplest σ - δ curve such as Figure 3.12 (c).

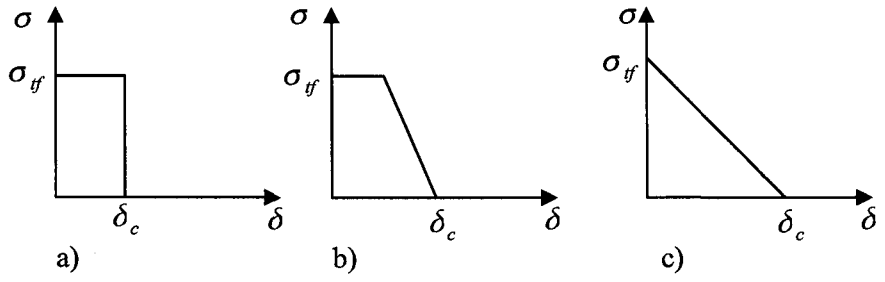

Figure 3.12: Typical stress-separation curves.

Quantification of the stress-separation model requires knowledge of the shape of the curve. The shape of the stress-separation curve is important in determining the fracture process zone development. Typical shapes based on concrete are shown in Figure 3.12. Pure polycrystalline ice has a much more homogeneous (uniform) microstructure than concrete; as a result the curve is unlikely to have an elongated tail and the choice of a linear stress- separation curve (see Figure 3.12 (c)) may be realistic. Identical simplifying assumptions have been successfully applied to concrete. The critical separation distance is then given by [44]:

$$\delta_c = 2G_f / \sigma_{tf} \tag{3.27}$$

The value of G_f for ice should be obtained from the area under the stress-separation curve. In the absence of experimental data for the curve, G_f may be estimated from K_{Ic} values obtained from conventional tests conducted on ice at high loading rates.

3.3.3.4 Using brittle cracking criterion

It is generally accepted that brittle materials such as ice and concrete exhibit two modes of behaviour:

1) A brittle mode that is related to cleavage, shear and mixed-mode fracture mechanisms that are observed under tension and tension-compression states of stress.
2) A ductile mode that is associated with distributed microcracking mechanisms that are primarily observed under compression states of stress. It involves the hardening of the material.

The brittle cracking theory considers only the brittle aspects of a brittle material. Although this is a great simplification, there are many cases where only the brittle

behaviour of a material is significant, and therefore the assumption that the material is linear elastic in compression is justified in those cases. Therefore, the brittle cracking model:

1) Is used for cases in which the behaviour of the brittle material is dominated by tensile cracking like the behaviour of ice in our tensile test.
2) Assumes that the compressive behaviour of brittle material is always linear elastic.

The cracking behaviour is defined in three parts:

I. Crack directions

The fixed orthogonal cracks model is used with the maximum number of cracks at a material point limited by the number of direct stress components present at that material point of the finite element model (for example, a maximum of three cracks in three-dimensional, axisymmetric, and plane strain problems). Once a crack is created at a point, the component of all vector and tensor valued quantities are rotated so that they lie in the local system defined by the crack orientation vectors (the normals to the crack faces). The model ensures that these crack face normal vectors are orthogonal so that this local system is the rectangular Cartesian. Crack closing and reopening can take place along the directions of the crack surface normals. The model neglects any permanent strain associated with cracking; that is, we assume that the cracks can close completely when the stress across them becomes compressive [1].

II. Crack detection

In order to detect crack initiation a simple Rankine criterion is used. Based on this criterion, a crack forms when the maximum principal tensile stress exceeds the tensile strength of the brittle material. Cracking is not recoverable. This means that once a crack

occurred at a point, it remains throughout the rest of calculation. However, crack closing and reopening may take place along the directions of the crack surface normals. Any permanent strain associated with cracking is neglected by the model. Therefore, it is assumed that when the stress across the cracks becomes compressive the cracks can close completely.

Although crack detection is based on the Mode I fracture, while cracked behaviour includes both Mode I (tension softening/stiffening) and Mode II (shear softening/retention) behaviour, details of these two modes will be described later.

III. Cracking conditions

A consistent condition for cracking in the crack direction coordinate system in the form of a tensor is:

$$C = C\left(t, \sigma^{I,II}\right) = 0 \tag{3.28}$$

where $C = \left[C_{nn}\, C_{tt}\, C_{ss}\, C_{nt}\, C_{ns}\, C_{ts}\right]^T$

and $t = \left[t_{nn}\, t_{tt}\, t_{ss}\, t_{nt}\, t_{ns}\, t_{ts}\right]^T$ is stress in the local cracking system and $\sigma^{I,II}$ represents a mode I fracture (tension softening mode) in the case of the direct components of stress and a mode II fracture (shear softening/retention model) in the case of the shear components of stress. The matrices $\partial C/\partial t$ and $\partial C/\partial \sigma^{I,II}$ are assumed to be diagonal, implying the assumption that there is no coupling between cracks in the cracking conditions. Two states of cracking are possible for each cracking condition (an opening crack state and a closing/reopening crack state). This can be described by writing the cracking conditions for a particular crack normal direction n (can also be written for the other two possible crack normal directions, s and t):

$$C_{nn} = C_{nn}(t_{nn}, \sigma_t^I) = t_{nn} - \sigma_t^I\left(e_{nn}^{ck}\right) = 0 \tag{3.29}$$

For an opening crack state where $\sigma_t^I\left(e_{nn}^{ck}\right)$ is the tension softening evolution and e_{nn}^{ck} is the crack opening strain and this parameter must be defined by the user. And

$$C_{nn} = C_{nn}(t_{nn}, \sigma_C^I) = t_{nn} - \sigma_C^I\left(e^{ck}_{nn}\right)\Big|_{e_{nn}^{open}} = 0 \tag{3.30}$$

for a closing/reopening crack where $\sigma_C^I\left(e_{nn}^{ck}\right)\Big|_{e_{nn}^{open}}$ is the crack closing/reopening evolution. These two conditions are illustrated in Figure 3.13; also, the tension softening model (mode I) is represented. It should be noted that similar conditions can be written for the other two possible crack normal directions, s and t.

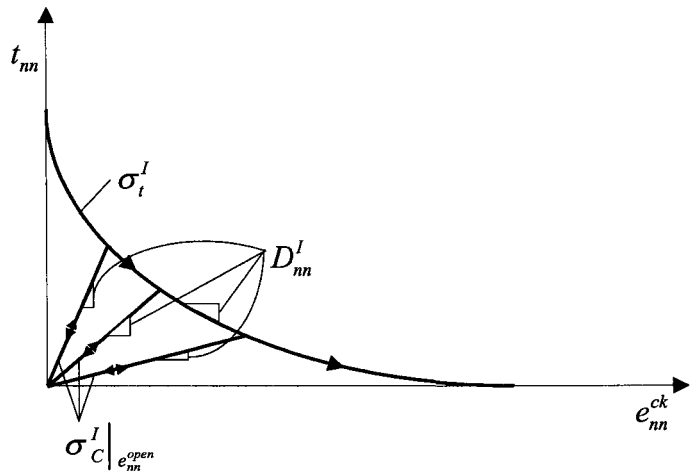

Figure 3.13: Cracking conditions for Mode I cracking [1].

Also, the shear cracking conditions can be presented, for example, by writing the conditions for shear component nt (also can be written for the other possible shear components). Therefore, the crack opening dependent shear model (shear retention model) is written as:

$$C_{nt} = C_{nt}(t_{nt}, \sigma_S^{II}) = t_{nt} - \sigma_S^{II}(g_{nt}^{ck}, e_{nn}^{ck}, e_{tt}^{ck}) = 0 \tag{3.31}$$

where $\sigma_S^{II}(g_{nt}^{ck}, e_{nn}^{ck}, e_{tt}^{ck})$ is the shear evolution that depends linearly on the shear strain and also depends on the crack opening strain (e_{nn}^{ck}) (this parameter also must be defined by the user). This model is illustrated in Figure 3.14.

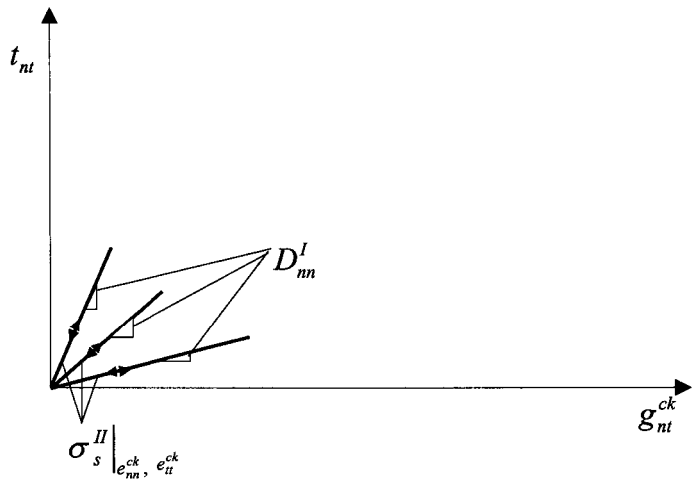

Figure 3.14: Cracking conditions for Mode II cracking [1].

Although crack detection is based purely on Mode I fracture considerations, ensuing cracked behaviour includes both Mode I (tension softening) and Mode II (shear softening/retention) behaviour, as described:

1) Tension softening/stiffening (mode I):

The basis of the post-cracked behaviour in the direction normal to the crack surface (tension softening) comes from the brittle fracture concept of Hilleborg [81]. Hilleborg defines the energy required to open a unit area of crack in Mode I, G_f^I as a material parameter, using brittle fracture concepts. This fracture energy can be calculated from measuring the tensile stress as a function of the crack opening displacement, as follows:

$$G_f^I = \int \sigma_t^I \, d u_n \tag{3.32}$$

As aforementioned, the mode I fracture energy G_f^I can be specified directly as a material property; in this case, the failure stress σ_t^I is defined as a tabular function of the mode I fracture energy. This model assumes a linear loss of strength after cracking (see Figure 3.15).

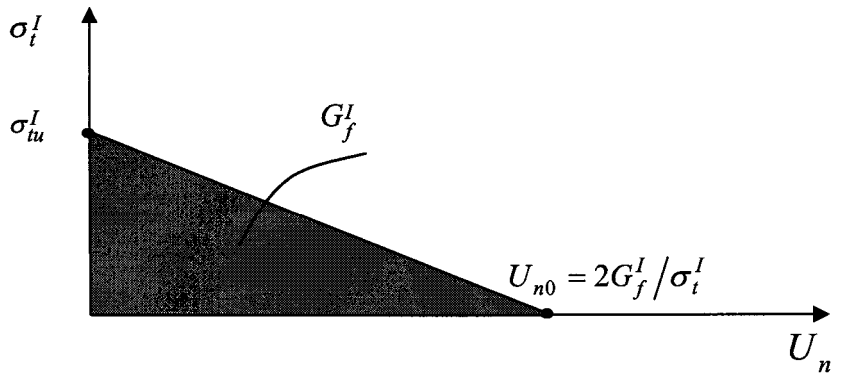

Figure 3.15: Post-failure stress-fracture energy curve [1].

The crack normal displacement at which complete loss of strength takes place is, therefore, $U_{n0} = 2G_f^I / \sigma_t^I$.

2) Shear retention model (mode II):

An important aspect of the cracking model is that, whereas crack initiation is based on Mode I fracture only, post-cracked behaviour includes Mode II as well as Mode I. The Mode II shear behaviour depends on the amount of crack opening. The dependency is when the crack opens, the cracked shear modulus is reduced. Therefore, a shear retention model can be used in which the post-cracked shear stiffness is defined as a function of the

opening strain across the crack. This shear retention model defines the total shear stress as a function of the total shear strain (shear direction *nt* is used as an example):

$$t_{nt} = D^{II}_{nt}(e^{ck}_{nn}, e^{ck}_{tt})\, g^{ck}_{nt} \tag{3.33}$$

where $D^{II}_{nt}(e^{ck}_{nn}, e^{ck}_{tt})$ is a stiffness that depends on crack opening, D^{II}_{nt} can be expressed as :

$$D^{II}_{nt} = \alpha(e^{ck}_{nn}, e^{ck}_{tt})\, G \tag{3.34}$$

where G is the shear modulus of the uncracked material and $\alpha(e^{ck}_{nn}, e^{ck}_{tt})$ is a user-defined dependence of the form shown in Figure 3.16.

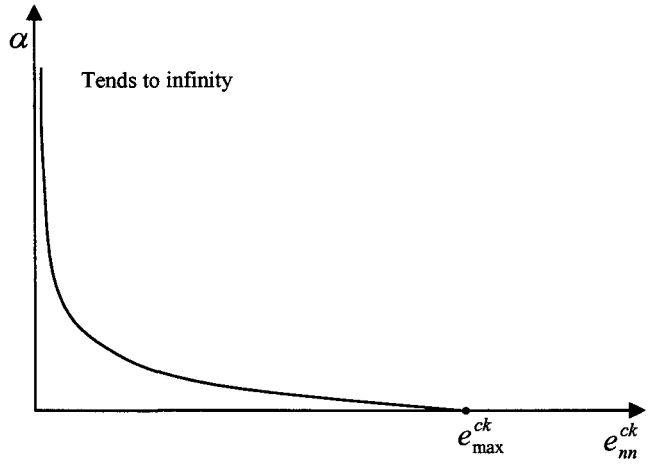

Figure 3.16: Shear retention factor dependence on crack opening [1].

A mathematical form for this dependence when there is only one crack, related to direction n, is the power law form [5]:

$$\alpha(e_{nn}^{ck}) = \frac{\left(1 - \frac{e_{nn}^{ck}}{e_{\max}^{ck}}\right)^{P}}{1 - \left(1 - \frac{e_{nn}^{ck}}{e_{\max}^{ck}}\right)^{P}} \tag{3.35}$$

where P and $e_{\max}^{ck}$ are material parameters. This form satisfies the requirements that $\alpha \to \infty$ as $e_{nn}^{ck} \to 0$ (corresponding to the state before crack initiation) and $\alpha \to 0$ as $e_{nn}^{ck} \to e_{\max}^{ck}$ (corresponding to complete loss of aggregate integrate). It should be noted that the bounds of α, as defined in our model using the elastic-cracking strain decomposition, are ∞ and zero. This compares with some of the traditional shear retention models where the intact brittle material and cracking strains are not separated; in these models the shear retention is defined using a shear retention factor ρ, which can have values between one and zero. The relationship between these two shear retention parameters is:

$$\rho = \frac{\alpha}{(\alpha + 1)} \tag{3.36}$$

The shear retention power law form given in Equation 3.35 can then be written in terms of ρ as:

$$\rho\left(e_{nn}^{ck}\right) = \left(1 - \frac{e_{nn}^{ck}}{e_{\max}^{ck}}\right)^{P} \tag{3.37}$$

Since users are more accustomed to specifying shear retention factors in the traditional way, (with values between one and zero), the data needed are $\rho - e_{nn}^{ck}$ data. Using the above equations, these data are then converted to $\alpha - e_{nn}^{ck}$ data for computation purposes.

Therefore, in shear retention models the dependence is defined by expressing the post-cracking shear modulus G_c, as a fraction of the uncracked shear modulus G:

$$G_c = \rho(e_{nn}^{ck})G \tag{3.38}$$

where the shear retention factor $\rho(e_{nn}^{ck})$, depends on the crack opening strain, e_{nn}^{ck}. This dependence can be illustrated in piecewise linear form, as shown in Figure 3.17 [1].

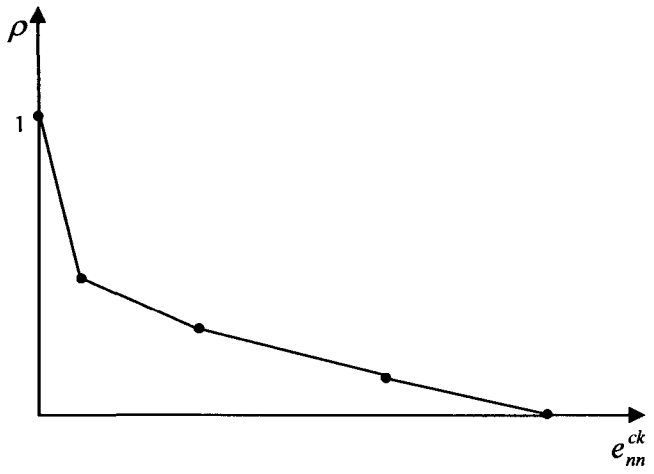

Figure 3.17: Piecewise linear form of the shear retention model [1].

At least one experiment, a uniaxial tension test, is required to calibrate the simplest version of the brittle cracking model. Usually, this test is difficult to perform because it is necessary to have a very stiff testing machine to record the post-cracking response. Quite

often such equipment is not available; in this situation we must make an assumption about the tensile failure strength of the material and the post-cracking response. For ice, the tensile strength is about 1.4 MPa [83]. Other experiments may be required to gain accuracy in post-failure behaviour.

Calibration of the post-cracking shear behaviour (mode II) requires combined tension and shear experiments, which are also difficult to perform. Because such test data are not available, a value for crack opening strain e_{nn}^{ck} is assumed. It is also assumed that the shear retention factor ρ, goes linearly to zero at this crack opening strain.

3.4 Model for the interface

3.4.1 Introduction

Although the strength of ice itself is interesting for glaciologists, the adhesion of ice to metals is a matter of great concern to those involved with the operation of civil, nautical and aeronautical structures in cold regions. Three failure modes can be considered for the calculation of the strength of adhesively bonded joints: 1) substrate failure, 2) adhesive failure (the interfacial failure between adhesive and substrate) and 3) cohesive failure (internal failure of the adhesive itself). In other words, the bond will fail when the maximum strength of the bonded materials is less than the strength of the adhesive strength between them. Generally, the failure of joints is neither completely cohesive nor completely adhesive. As noted in Chapter 2, for the thin thickness of the ice layer, because ice is a brittle material and is not strong in either tensile or compressive mode, the stress developed on freezing might cause cracking, producing a cohesive

failure before an adhesive failure. In other words, ice cohesion force is weaker than its adhesion force; therefore, cohesive failure is more probable than adhesive failure. The studies on the mechanics of adhesion [43] demonstrate that the cohesive strength of an adhering material has a direct affect on its adhesive properties.

As discussed earlier, the cohesive strength of ice has been investigated by many researchers, and it can be seen that the cohesive strength of ice depends on the applied technique and the testing conditions [34, 36, 42, 53 and 103]. Goodman [37] and Goodman and Tabor [66] measured fracture energy using the three-point bending test of sharply notched beams, as well as by a diamond indentation test, while Liu and Miller [52] carried out tests on compact tension specimens at different rates.

A review of the adhesive properties of ice has been done by Jellinek [6], who considered the idea that a liquid-like transition layer exists at the ice/solid interface in order to describe the characteristics of ice adhesion. His idea is especially useful in explaining the differences between tensile and shear modes of adhesive testing and the transition from cohesive to adhesive failure with rising temperature [77].

When water is frozen on to a clean metal surface the interface is stronger than the ice, and fracture occurs within the ice itself. The detailed behaviour depends on the stresses distributed near the interface. If the values of tensile stresses are high, then the failure mode is brittle and the breaking stress is independent of temperature. If the tensile stresses are less than a critical limit the failure mode is ductile, and the breaking stress increases linearly with reduction in temperature below 0°C [18].

3.4.2 The cohesive material theory

3.4.2.1 Introduction

A new family of cohesive elements has been introduced to bond components together and can be used for detailed modeling of the deformation and damage of adhesive layers at interfaces between bonded parts. Application includes finite thickness, as well as zero thickness adhesive between two parts. The constitutive response of cohesive elements depends on the specific application and is based on assumptions about the stress states and deformation that are suitable for each application area. If the cohesive zone is very thin and for all practical purposes may be considered to be of zero thickness. Cohesive behaviour defined directly in terms of a traction-separation law [1]:

1) can be used to model the delamination at interfaces in composites directly in terms of traction versus separation;
2) allows specification of material data such as the fracture energy as a function of the ratio of normal to shear deformation (mode mix) at the interface;
3) assumes a linear elastic traction-separation law prior to damage;
4) assumes that failure of the elements is characterized by progressive degradation of the material stiffness, which is driven by a damage process.

In this case, the macroscopic material properties are not directly relevant, and the analyst must resort to concepts derived from fracture mechanics such as the amount of energy required to create new surfaces. In three-dimensional problems the traction-separation-based model assumes three components of separation, one normal to the

interface and two parallel to it, and the corresponding stress components are assumed to be active at a material point.

3.4.2.2 Constitutive equation

An appropriate constitutive equation in the formulation of the decohesion element is fundamentally needed for an accurate simulation of the interlaminar cracking process. A constitutive equation is used to connect the traction σ to the relative displacement δ, at the interface. Some proposed softening models are shown in Figure 3.18. All softening models show that the cohesive zone can still transfer load after the beginning of damage (δ^0 in Figure 3.18). For pure mode I, II or III loading, after the interfacial normal or shear tractions reach their interlaminar tensile or shear strengths, the stiffness is gradually reduced to zero. The area under the traction-relative displacement curves is the related (mode I, II or III) fracture energy. Using the definition of the J integral [80], it can be proved that for small cohesive zones:

$$\int_0^{\delta^f} \sigma(\delta)\, d\delta = G_C \tag{3.39}$$

where G_C is the critical energy release rate for a respective mode, and δ^f is the corresponding relative displacement at failure ($\delta_{pp}, \delta_{pro}, \delta_{lin}$ or δ_{Ne} in Figure 3.18).

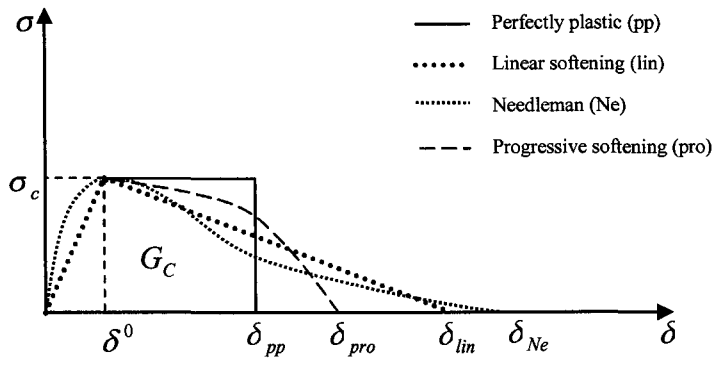

Figure 3.18: Strain softening constitutive model [21].

3.4.2.3 Bilinear softening model

The linear elastic-linear softening (bilinear) model (see Figure 3.18) is the simplest way to perform, and is most commonly used to define a softening model. The material response is illustrated in Figure 3.19. Point 1 is related to a low tensile load in the linear elastic range. A high initial stiffness K_P (penalty stiffness) is used to hold the top and bottom faces of the interface element together. After the interfacial normal or shear tractions reach their relative interlaminar tensile or shear strength (point 2), the stiffness is gradually reduced to zero. In other words, point 2 represents the onset of damage. In single-mode delamination, the traction at point 2 is equal to the corresponding interlaminar strength of the material σ_C. This value is denoted by T for the interlaminar tensile strength in mode I and S and N for interlaminar shear strength in modes II and III respectively. Therefore the onset displacements can be defined as:

$$\delta_I^0 = T/K_P \,,\ \delta_{II}^0 = S/K_P \,,\ \delta_{III}^0 = N/K_P \tag{3.40}$$

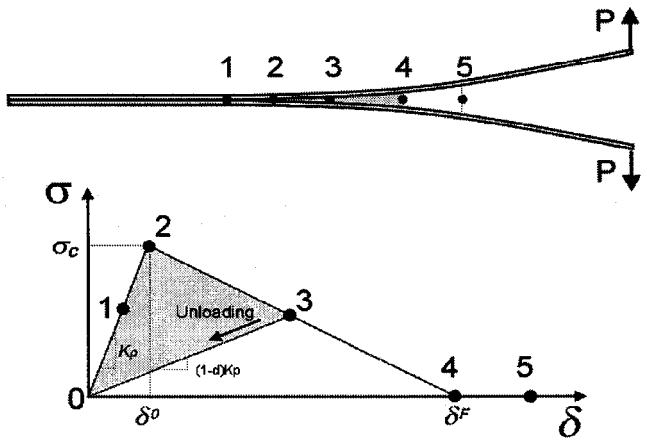

Figure 3.19: Bilinear constitutive model [21].

The area under the traction-relative displacement curves for Mode I, II or III is the relative critical energies released at failure G_{IC}, G_{IIC}, G_{IIIC} respectively:

$$G_{IC} = \int_0^{\delta_I^f} \sigma_z d\delta_z$$

$$G_{IIC} = \int_0^{\delta_{II}^f} \tau_{xz} d\delta_x$$

$$G_{IIIC} = \int_0^{\delta_{III}^f} \tau_{yz} d\delta_y \qquad (3.41)$$

Then, the final relative displacements, corresponding to complete decohesion are obtained as:

$$\delta_I^f = 2G_{IC}/T$$

$$\delta_{II}^f = 2G_{IIC}/S$$

$$\delta_{III}^f = 2G_{IIIC}/N \qquad (3.42)$$

As shown in Figure 3.19, as the respective displacement increases, the interface accumulates damage and the traction is lower than the strength (point 3). The area of the triangle 0-2-3 shows the energy released at point 3. At point 4, the energy release rate

reaches the critical value. For any respective displacement larger than point 4, the interface is unable to transfer any tensile or shear loads and all the penalty stiffness reverts to zero (point 5). This means that all the available interfacial fracture energy has been completely used at point 4 [21]. The bilinear interfacial constitutive response shown in Figure 3.19 can be performed in three cases as follows:

i) $\delta \langle \delta^0$, which in this case the constitutive equation is given by:

$$\sigma = K_P \delta \tag{3.43}$$

ii) $\delta^0 \leq \delta \langle \delta^F$, which in this case the constitutive equation is given by:

$$\sigma = (1 - D) K_P \delta \tag{3.44}$$

where D represents the damage accumulated at the interface, which is zero initially, and reaches 1 when the material is fully damaged.

iii) $\delta \geq \delta^F$, in this case all the penalty stiffness is equal to zero and if crack closure is detected, interpenetration is prevented by reapplying only the normal stiffness. Frictional effects are ignored.

Briefly, the parameters required to define the bilinear interfacial softening model are the penalty stiffness K_P, the fracture energies G_{IC}, G_{IIC} and G_{IIIC} and the corresponding nominal interlaminar tensile T and shear strengths, S and N [18].

3.4.2.4 Mixed-Mode Delamination Criterion

In structural applications delamination growth is usually most likely to occur under mixed-mode loading. Therefore, a general formulation for decohesion elements must satisfy the mixed-mode delamination growth problems.

Under pure mode I, II or III loading, the onset of damage at the interface can be determined simply by comparing the tractions (stress components) with their respective allowable. It should be noted that the onset of damage does not imply the initiation of delamination, since the tractions closing the crack at onset are at their maximum value. However, under mixed-mode loading, the beginning of damage may occur before any of the stress components involved attain their respective allowable. The mixed-mode criterion proposed is based on a few simplifying assumptions. Firstly, it is assumed that damage initiation can be predicted using the quadratic failure criterion:

$$\sqrt{\left(\frac{\sigma_z}{T}\right)^2+\left(\frac{\tau_{xz}}{S}\right)^2+\left(\frac{\tau_{yz}}{S}\right)^2}=1 \qquad \text{for} \qquad \sigma_z \rangle 0 \tag{3.45}$$

$$\sqrt{\left(\frac{\tau_{xz}}{S}\right)^2+\left(\frac{\tau_{yz}}{S}\right)^2}=1 \qquad \text{for} \qquad \sigma_z \leq 0 \tag{3.46}$$

where σ_z is the normal traction, and τ_{xz} and τ_{yz} are the transverse shears. T and S are the nominal normal tensile and shear strengths, respectively. It is assumed that the delamination mechanisms in mode II and mode III are the same. Therefore, mode III can be combined with mode II by using a total tangential displacement δ_{II} defined as the norm of the two orthogonal tangential relative displacements δ_x and δ_y as:

$$\delta_{II}=\sqrt{\delta_x{}^2+\delta_y{}^2} \tag{3.47}$$

The total mixed-mode relative displacement δ_m is defined as:

$$\delta_m=\sqrt{\delta_z{}^2+\delta_{II}^2} \tag{3.48}$$

where δ_z is the relative opening (mode I) displacement. Using the same penalty stiffness K_p in modes I and II, the tractions before the onset of damage are:

$$\begin{aligned} \sigma_z &= K_P \delta_z \\ \tau_{xz} &= K_P \delta_x \\ \tau_{yz} &= K_P \delta_y \end{aligned} \tag{3.49}$$

The single-mode failure initiation displacements are then:

$$\begin{aligned} \delta_{II}^0 &= \frac{S}{K_p} \\ \delta_I^0 &= \frac{T}{K_p} \end{aligned} \tag{3.50}$$

If the relative opening displacement δ_z is not zero, the mode mixity can be expressed by:

$$\beta = \frac{\delta_{II}}{\delta_z} \tag{3.51}$$

The mixed-mode damage initiation displacement is obtained by substituting Equations 3.47-3.51 into 3.45, as:

$$\delta^0 = \delta_I^0 \delta_{II}^0 \sqrt{\frac{1+\beta^2}{(\delta_{II}^0)^2 + (\beta \delta_I^0)^2}} \tag{3.52}$$

The energy release rates and fracture toughness are generally used to predict the propagation of delamination under mixed-mode loading conditions. The most famously used criteria to predict the interaction of the energy release rates in mixed-mode is the power law form given by the expression:

$$\left(\frac{G_I}{G_{Ic}}\right)^{\alpha} + \left(\frac{G_{II}}{G_{IIc}}\right)^{\alpha} = 1 \tag{3.53}$$

where the value of exponent α in the power law form is usually selected to be either 1 or 2, in which case the criterion is a two-parameter interaction law with parameters G_{Ic} and G_{IIc}.

For the bilinear traction-relative displacement softening law assumed here, the critical energy release rates in mode I and mode II are:

$$G_{Ic} = \frac{T\delta_I^f}{2} \quad , \qquad G_{IIc} = \frac{S\delta_{II}^f}{2} \tag{3.54}$$

where δ_I^f and δ_{II}^f are the ultimate opening and tangential displacements, respectively. The mode I and mode II energies released at failure are calculated from Equations [21]:

$$G_I = \int_0^{\delta_I^{FM}} \sigma_{zz} d\delta_I \qquad , G_{II} = \int_0^{\delta_{II}^{FM}} \sqrt{\tau_{xz}^2 + \tau_{yz}^2}\, d\delta_{II} \tag{3.55}$$

3.5 The finite element model

3.5.1 Equilibrium equations and the Principle of Virtual Work

The Principle of Virtual Work states that the external virtual work is equal to internal virtual work when equilibrated forces and stresses undergo unrelated but consistent displacements and strains. For a general three-dimensional body that is in equilibrium, the external forces acting on the body are surface traction F^S, body forces F^B, and concentrated forces F^i. These forces include all externally-applied forces and reactions and have in general three components corresponding to the three coordinate axes [12]:

$$F^B = \begin{bmatrix} F_X^B \\ F_Y^B \\ F_Z^B \end{bmatrix}, \quad F^S = \begin{bmatrix} F_X^S \\ F_Y^S \\ F_Z^S \end{bmatrix}, \quad F^i = \begin{bmatrix} F_X^i \\ F_Y^i \\ F_Z^i \end{bmatrix} \tag{3.56}$$

The displacements of the body from the unloaded configuration are denoted by U, where

$$U^T = [U \quad V \quad W] \tag{3.57}$$

The strains corresponding to U are:

$$\varepsilon^T = [\varepsilon_{XX} \quad \varepsilon_{YY} \quad \varepsilon_{ZZ} \quad \gamma_{XY} \quad \gamma_{YZ} \quad \gamma_{ZX}] \tag{3.58}$$

and the stresses corresponding to ε are:

$$\tau^T = [\tau_{XX} \quad \tau_{YY} \quad \tau_{ZZ} \quad \tau_{XY} \quad \tau_{YZ} \quad \tau_{ZX}] \tag{3.59}$$

An approach to express the equilibrium of the body is to use the principle of virtual displacements. This principle states that the equilibrium of the body requires that for any compatible, small virtual displacements (which satisfy the essential boundary conditions) imposed onto the body, the total internal virtual work is equal to total external virtual work:

$$\int_V \bar{\varepsilon}^T \tau \, dV = \int_V \bar{U}^T F^B \, dV + \int_S \bar{U}^{S^T} F^S \, dS + \sum_i \int_S \bar{U}^{i^T} F^i \tag{3.60}$$

The internal virtual work is given on the left side of Eq.3.60, and is equal to the actual stresses τ going through the virtual strains $\bar{\varepsilon}$ (that correspond to the imposed virtual displacements):

$$\bar{\varepsilon}^T = [\bar{\varepsilon}_{XX} \quad \bar{\varepsilon}_{YY} \quad \bar{\varepsilon}_{ZZ} \quad \bar{\gamma}_{XY} \quad \bar{\gamma}_{YZ} \quad \bar{\gamma}_{ZX}] \tag{3.61}$$

The external work is given on the right side of Eq.3.60, and is equal to the actual forces F^B, F^S and F^i going through the virtual displacements $\bar{U}$, where:

$$\overline{U}^T = \begin{bmatrix} \overline{U} & \overline{V} & \overline{W} \end{bmatrix} \tag{3.62}$$

The equation (3.60) is an expression of equilibrium, and for different virtual displacements, correspondingly different equations of equilibrium are obtained. As an example the virtual work $W(u)$ for contact problems can be expressed in terms of virtual work of internal $W(\text{int})$, external $W(ext)$ and contact $W(cnt)$ as [24]:

$$W(u) = W_{\text{int}}(u) + W_{ext}(u) + W_{cnt}(u) \tag{3.63}$$

Also, for a large displacement formulation, neglecting inertia and body forces, the virtual work expression for a body of volume V containing various cohesive surfaces denoted by S_{coh} can be written in the form [88]:

$$\int_V \sigma \nabla^S \delta u dV + \int_{Scoh} \delta \Delta u^T t_{coh} \, dS_{coh} = \int_{Sext} \delta u^T t_{ext} \, dS_{ext} \tag{3.64}$$

where σ is the Cauchy stress tensor, u denotes the displacement field and Δu is the relative displacement between point pairs on opposing sides of the cohesive surface. Also, t_{coh} and t_{ext} denote the tractions acting, respectively, across the cohesive surfaces and on the external surfaces in the current configuration.

3.5.2 Interface finite element

3.5.2.1 Element kinematics

In order to predict the initiation and growth of delamination, a zero-thickness decohesion element with 8-nodes is proposed to simulate the cohesive layer connecting two lamina of a composite laminate (Figure 3.20). The constitutive equation of zero-thickness decohesion elements is introduced based on relative displacements and

tractions across the interface. The vector defining the relative displacement in global coordinates, Δ, can be obtained as:

$$\Delta_i = u_i^+ - u_i^- = N_k u_{ki}^+ - N_k u_{ki}^- = \overline{N}_k u_{ki} \tag{3.65}$$

where N_k are standard lagrangian shape functions, u_i^+ and u_i^- are the components of the displacements of the top and bottom surfaces respectively, u_{ki}^+, u_{ki}^- are the displacements in i direction of k top and bottom nodes of the element, respectively [18].

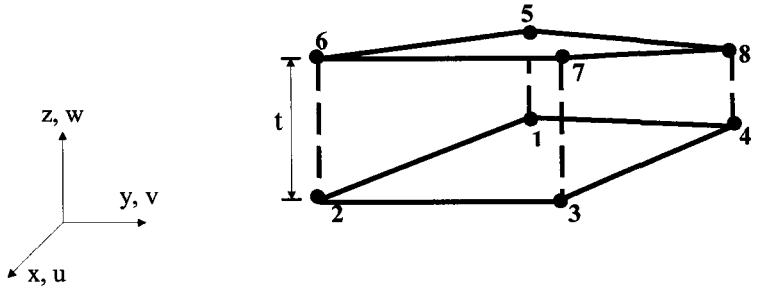

Figure 3.20: Eight- node decohesion element, t = 0.

For a general element shape and alignment, the normal and tangential relative displacements δ_s must be determined in local coordinates. Therefore, using Equation 3.65 and defining the transformation tensor θ_{si}, the transformation between the local and the global coordinate is defined as [18]:

$$\delta_s = \theta_{si}\Delta_i = \theta_{si}\overline{N}_k u_{ki} = B_{sik}u_{ki} \tag{3.66}$$

3.5.2.2 Element Formulation

The element stiffness matrix is obtained by considering the standard isoparametric linear Lagrangian interpolation functions for three-dimensional (8-node) elements. The respective displacements between the top and the bottom faces of the element in a local coordinate frame x-y-z can be written as:

$$\begin{Bmatrix} \delta_z \\ \delta_x \\ \delta_y \end{Bmatrix} = \begin{Bmatrix} w \\ u \\ v \end{Bmatrix}_{top} - \begin{Bmatrix} w \\ u \\ v \end{Bmatrix}_{bot} = BU \tag{3.67}$$

where B is the matrix that relates the element's degrees of freedom U to the relative displacements between the top and bottom interfaces. The three-dimensional form of Eq. 3.42 is:

$$\sigma = (I - D)C\delta \quad \text{or} \quad \begin{Bmatrix} \delta_z \\ \tau_{xz} \\ \tau_{yz} \end{Bmatrix} = (I - D)C \begin{Bmatrix} \delta_z \\ \delta_x \\ \delta_y \end{Bmatrix} \tag{3.68}$$

where I is the identity matrix, C is the undamaged constitutive matrix

$$C = \begin{bmatrix} K_P & 0 & 0 \\ 0 & K_P & 0 \\ 0 & 0 & K_P \end{bmatrix} \tag{3.69}$$

and D is a diagonal matrix representing the damage accumulated at the interface:

$$D = \begin{bmatrix} d & 0 & 0 \\ 0 & d & 0 \\ 0 & 0 & d \end{bmatrix} \tag{3.70}$$

where d is the damage parameter, which is a nonlinear function of $\delta_m^{\max}$, the highest mixed-mode relative displacement experienced by the material is:

$$d = \frac{\delta^F (\delta_m^{\max} - \delta^0)}{\delta_m^{\max} (\delta^F - \delta^0)} \tag{3.71}$$

The minimization of the potential energy subjected to the kinematic constraints of Eq. 3.65 leads to the usual integral over the area of the element, which gives the following element stiffness [21]:

$$K_{elem} = \int_A B^T ((I - D)C) B \, dA \tag{3.72}$$

3.5.2.3 Discretization - computational model

Based on the work of Beer, the interface element is formulated [14]. A non-linear solution procedure is required because of the geometrical nonlinearities and the nonlinear mechanical behaviour of the interface material. Two required parameters of the nonlinear solution procedure, the tangent stiffness matrix K_t^e and the internal force vector f_{int}^e, are obtained in this section.

A 2n-noded isoparametric interface element with 6n degrees of freedom for three dimensional analyses is used. The element consists of an upper and lower surface $S_e^{\pm}$ and the natural coordinate system is η_1 and η_2. For the surfaces $S_e^{\pm}$, node j has three translational degrees of freedom, $q_{1j}^{\pm}$, $q_{2j}^{\pm}$ and $q_{3j}^{\pm}$, with the first subscript implying the associated global direction. The nodal displacement vector q is arranged as follows:

$$q = \left\{ q^+, q^- \right\}^T \tag{3.73}$$

$$q^{\pm} = \left\{ q_{11}^{\pm}, q_{21}^{\pm}, q_{31}^{\pm}, \ldots, q_{1n}^{\pm}, q_{2n}^{\pm}, q_{3n}^{\pm} \right\}^T$$

The displacement fields $U_j^{\pm}(\eta_1,\eta_2), j=1,2,3$ for the lower and upper surfaces are independent and in terms of the global displacement degrees of freedom vector $q_{ij}^{\pm}$:

$$U_j^{\pm}(\eta_1,\eta_2) = q_{jn}^{\pm} N_n(\eta_1,\eta_2) \tag{3.74}$$

where N_n is the shape function corresponding to the n-th degree of freedom. The virtual relative displacement vector $\delta\Delta$ in terms of $q_{jn}^{\pm}$:

$$\delta\Delta_i = Q_{ji}^{+} N_n \delta q_{jn}^{+} - Q_{ji}^{-} N_n \delta q_{jn}^{-} \tag{3.75}$$

The matrix form of Equation 3.75 is:

$$\delta\Delta = \left[Q_{+}^{T} N, -Q_{-}^{T} N\right]\delta q = \left[B^{+}, -B^{-}\right]\delta q = B\delta q \tag{3.76}$$

The internal force vector of the interface element is obtained by:

$$\delta W_{\text{int}}^{e} = \delta q^{T} \iint_{S_e^m} B^{T} T dS_e^m = \delta q^{T} f_{\text{int}}^{e} \tag{3.77}$$

where T is the traction vector acting on the deformed mid-surface and the integration is performed over the deformed element mid-surface. In numerical analyses, the internal force vector needs to be computed accurately, and the tangent stiffness matrix may be computed approximately. The computation of the tangent stiffness matrix is intensive and a very accurate expression is not required. For the computation of K_{et}, the derivatives of the rotation matrix with respect to the nodal displacements are neglected. This approximation with Equation 3.76 leads to:

$$\begin{aligned} &B^{+} = B^{-} = B_S \\ &\delta\Delta = \left[B_S, -B_S\right]\delta q = B'\delta q \end{aligned} \tag{3.78}$$

Thus, the approximate tangent stiffness matrix is:

$$K_t^e = \frac{\partial f_{\text{int}}^e}{\partial q} \approx \iint_{S_e^m} B'^{T} D B' dS_e^m \tag{3.79}$$

where D is the material tangent stiffness. Equation 3.79 is rewritten using the relation in Equation 3.78:

$$K_t^e = \begin{bmatrix} K_S & -K_S \\ -K_S & K_S \end{bmatrix} \tag{3.80}$$

where

$$K_S = \iint_{S_e^m} B_S{}^T D B_S \, dS_e^m \tag{3.81}$$

The internal force vector is accurately computed, while the approximations for the tangent stiffness matrix save computational time because only a quarter of the full matrix has to be computed [39].

CHAPTER 4

NUMERICAL SIMULATION

CHAPTER 4

NUMERICAL SIMULATION

4.1 Introduction

Analytical evaluations were performed with the commercial, general-purpose finite element code ABAQUS, which can effectively characterize the nonlinear behaviour in brittle fracture of ice. It also has the unique capability of describing the behaviour of an interface using the cohesive material. Three-dimensional finite element models were developed to determine the behaviour of the ice on substrate. The necessary input material properties (constitutive, brittle cracking and cohesive material properties) of the ice and interface are obtained from literature and some of them are assumed values based on the respective theories.

To identify possible modeling inconsistency and errors and to verify the accuracy of these computer codes, results from linear and nonlinear finite element analyses need to be compared with those from experimental tests. This may be obtained only if the analysis can account realistically for the material and geometric properties of the various components of a model and the interaction between them. However, the accuracy of the model was verified with data from tensile tests which were performed at the beginning of this research in laboratory testing (AMIL). It should be noted that the finite element method works very well for many structural materials such as steel and aluminium, which

have well-defined constitutive properties. When the constitutive behaviour is not so straightforward, the task is more difficult. For materials such as ice, in which discrete cracking occurs, this is certainly the case.

4.2 De-icing of a thin iced plate using tensile force

In this research, an investigation of the mechanical behaviour of ice on a thin aluminium plate is performed using finite element analysis. A numerical finite element for a thin iced plate is created and executed utilizing both linear and nonlinear approaches like geometric nonlinearity and the constitutive brittle cracking model for ice.

As described in Section 2.4, using a tensile test in which the sample (ice composite beam) is pulled uniformly in a single direction (uniaxial tension) until ice fractures, in the case of ice with a thickness of 2 mm (cohesive failure) , and removes, for the case of ice with a thickness of 10 mm (adhesive failure). For ice of a thickness equal to 5 mm, not only ice fracture but also ice removal occurs. It is obvious that this ice fracture or removal is because of the bending due to the change in the length of the sample as pulling proceeds.

Transfer of load to an adhesively-bonded structure like an interface of a thin iced composite beam by tension, either directly or indirectly (peel), shows the most severe form of loading, since the strength of the adhesive joint depends on the tensile strength of the adhesive, which is low. Generally, in a tensile test of adhesive bond, the adhesive is restrained in the radial and circumferential directions by the adherends (ice and aluminium). In the absence of this restraint, the adhesive is free to undergo radial contraction with respect to the stiffer adherend and it assumes that the adhesive has a

much lower stiffness than the adherends. It should be noted, from the ice composite beam test in tension that the stress state at the interface is complicated by through-thickness shear stresses and the presence of stress singularities.

4.2.1 Description of the problem

This work attempts a better comprehension of the behaviour of the interface ice-substrate, in order to improve mechanical ice removal and de-icing techniques. To do so, this research illustrates the application of cohesive elements to predict the initiation and progression of debonding at the ice-aluminium interface of an ice-coated beam. A complete analysis using ABAQUS requires a description of the material, the model formation, boundary conditions, and loading. For service-load simulations, at least two material constants are required to characterize the linear elastic behaviour of the material: Young's modulus (E) and Poisson's ratio (υ). For nonlinear analysis, the ice uniaxial behaviour beyond the elastic range must be defined to simulate its behaviour at higher stresses. The input parameters required to define the ice material are the E, υ and the other parameters for defining brittle cracking behaviour of ice, such as uniaxial tensile strength and fracture energy of ice. In this section, finite element models of three tests (three different thicknesses of ice) will be prepared, utilizing both linear and nonlinear approaches and using the finite element code ABAQUS. The finite element models will be calibrated using the available experimental data from the tests as well as some parameters from literature.

4.2.2 Loading, boundary conditions and meshing

The complete geometry of the model is shown in Figure 4.1. The length of the aluminium plate is 168 mm, and the length of the ice layer is 108.42 mm, with a 45-degree slope at each end of the ice-deposited mass. The uncovered part at each end of the plate is 29.79 mm. The width and the thickness of the plate are 18.87 mm and 0.43 mm, respectively. The thickness of the ice is 2 mm (also, the model will also be considered with ice thicknesses equal to 5 mm and 10 mm).

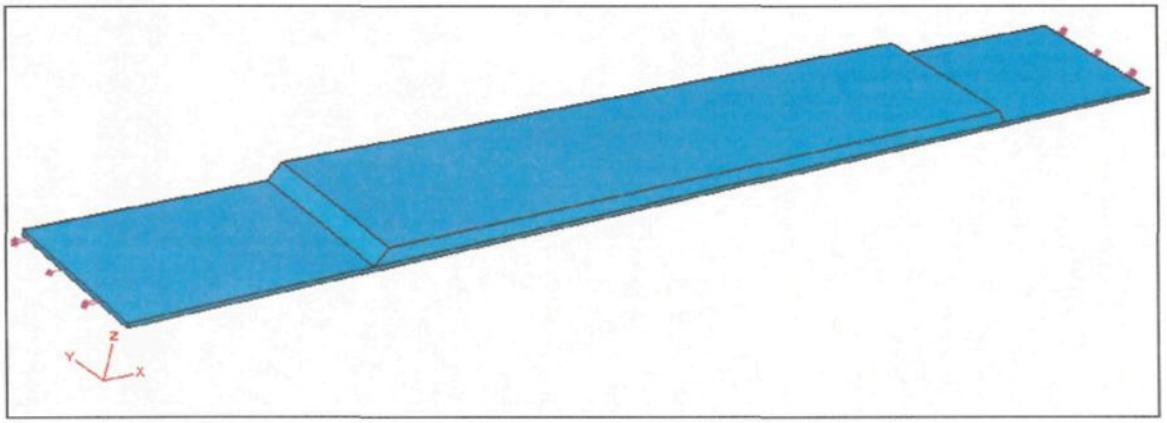

Figure 4.1: The complete geometry of model.

By increasing the number of elements in the meshing of the model the accuracy of the solution increases; however, it is immediately obvious that the time of solution with a progressive rate increases. In fact, one of the skills in the finite element is the ability to analyze the model with the maximum possible accuracy in the minimum time. For this reason, numerous techniques for solving the problem are used; of these, using the symmetry is one of the usual techniques. As shown in Figure 4.2 for the case of the complete model (a) the numbers of elements are four times the numbers in case (b), which means that the time for analysing case (a) will be more than four times than case

(b). But analyzing model (b) leads us to the same information as obtained by analyzing model (a). Therefore, we can use the model (b) with fine elements and at the same time the system will be solved with maximum accuracy. In these cases, it is extremely important to apply the boundary conditions correctly. However, because this model had two axes of symmetry, it was possible to represent the full model by modeling only one-quarter of the model.

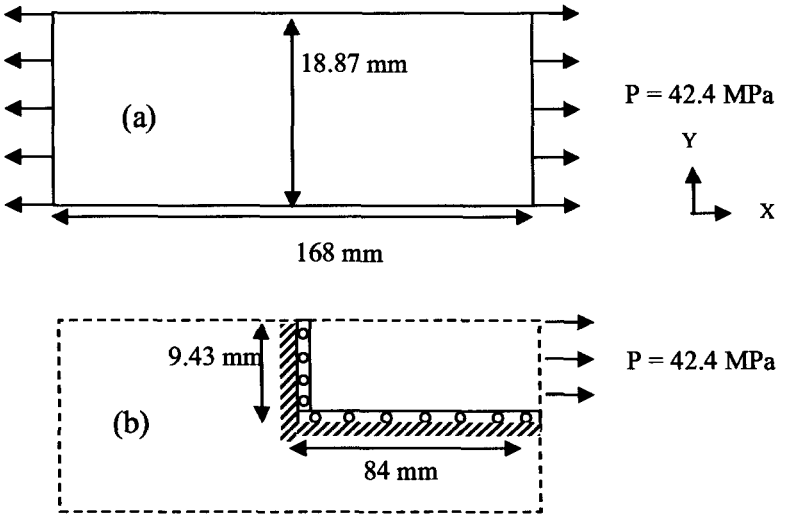

Figure 4.2: Symmetrical representation of the model.

Boundary conditions representing structural supports specify values of displacement and rotation variables at appropriate nodes. On the other hand, a boundary condition shows how the body is supported in space. To facilitate a more economical solution, finite element meshes may also use symmetry, which can be implemented with symmetric boundary conditions. For the model, two classes of boundary conditions (essential and natural boundary conditions) are considered. The essential boundary conditions (also called Dirichlet boundary conditions) correspond to prescribed

displacement and rotation. Therefore, for this model Ux = URy = URz = 0 (symmetry about plane x) that is applied to the symmetry of the length of the plane, and Uy = URx = URz = 0 (symmetry about plane y) that is applied to the symmetry of the across of the plane are essential conditions. Nodes at the side faces of the ice and aluminium sheeting along the specimen length and at the mid-length were given appropriate boundary conditions to simulate the continuity of the model in the lateral direction and the half model in the longitudinal direction. Therefore, according to these symmetry conditions, one-quarter of this model presents sufficient information about the completed mode. Other stresses with considering the symmetry will have the same conditions.

The second class of boundary conditions is natural boundary conditions, also called Neumann boundary conditions, which correspond to prescribed boundary forces and moments. For this model, the natural boundary condition Uz = URx = URy = 0 is applied for free body motions in the end of the plate where the force is applied to the plate as well.

The actual concentrated applying load for the model with 2 mm of ice is 343 N (this value is obtained from Figure 2.8 for which the ice is broken and the slope of the graph has changed) since only half of the plate is modeled, the actual concentrated load is 171.5 N. Therefore, the distribution force would be $p = \frac{F}{A} = \frac{171.5}{9.4 \times 0.43} = 42.4$ MPa. In the same manner for the case of the ice thicknesses equal to 5 mm and 10 mm, the distribution force is obtained as 40.59 and 36.70 MPa respectively. The loading and boundary conditions are shown in Figure.4.3.

For the three-dimensional computations, a one-quarter symmetry model with C3D20R elements was used. The kind of element shape for meshing was selected

hexahedral. The finite element of the symmetric half of the model is shown in Figure 4.4. At the interface, the boundaries are assumed to be in perfect contact condition without possibility of separation during the simulation.

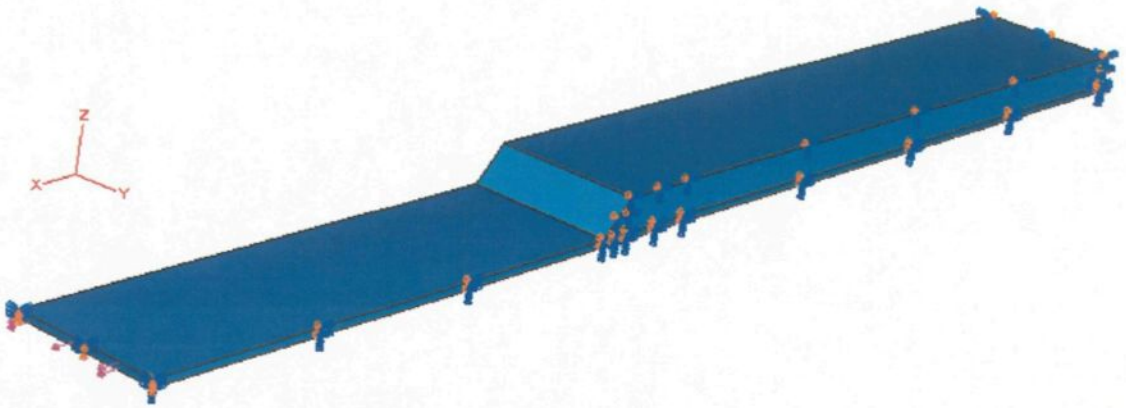

Figure 4.3: Loading and boundary conditions.

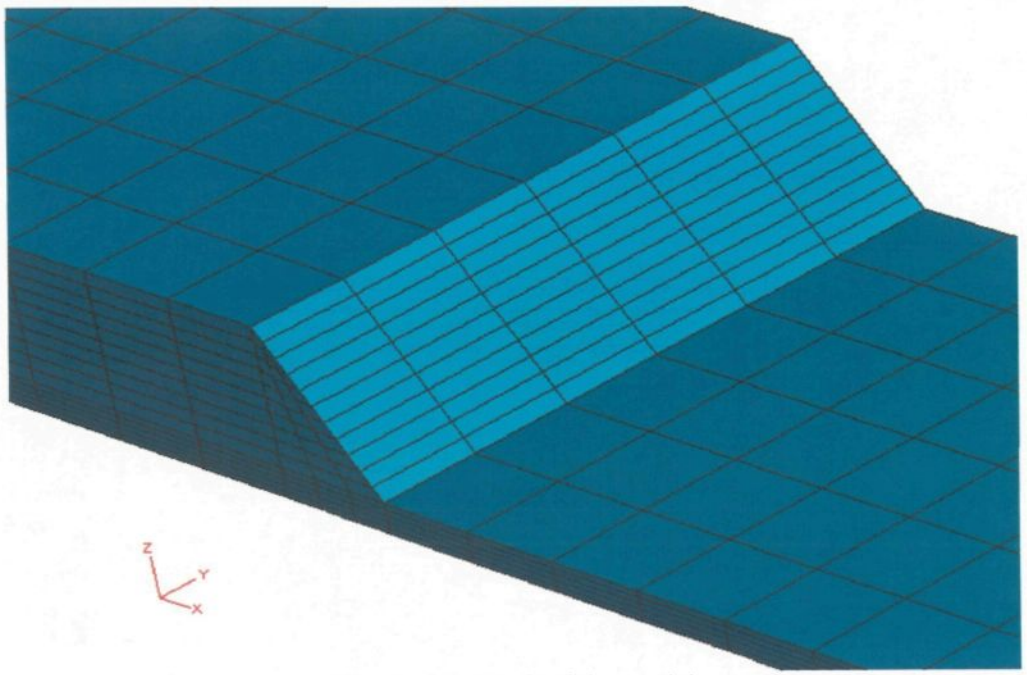

Figure 4.4: Mesh of the model.

4.2.3 The linear approach

In the linear finite element approach, it is assumed that the displacements of the finite element assemblage are infinitesimally small and that the material is linearly elastic. In addition, it is assumed that the nature of the boundary conditions remains unchanged during the application of the loads on the finite element assemblage. With these assumptions, the finite element equilibrium equations derived in [105]:

a) a linear form of strain-displacement relationships $\varepsilon = Su$ (where S is a suitable linear operator and u is the displacement response) and

b) a linear form of stress-strain relationships $\sigma = D(\varepsilon - \varepsilon_0) + \sigma_0$ (where D is an elasticity matrix containing the appropriate material properties).

In the linear approach, when the ice is deformed elastically, its behaviour follows Hook's law and the strain ε, is proportional to the applied stress. Therefore, the stress σ in a linear elastic material is given by the generalized Hook's law as $\{\sigma\} = [C]\{\varepsilon\}$ and by inversion the strains may be expressed as:

$$\{\varepsilon\} = [C]^{-1}\{\sigma\} = [D]\{\sigma\} \tag{4.1}$$

The matrix [C] is called the material stiffness matrix, while its inverse [D] is the material flexibility matrix. These relations between stress and strain take on less complex forms if we assume that the elastic body is homogeneous and isotropic. By homogeneous we mean that any elemental volume of the body possesses the same specific physical properties as any other elemental volume of the body; by isotropic we mean that the physical properties are the same in all directions. For homogeneous isotropic material only two physical constants are required to express all the coefficients in Hook's law;

these are Young's modulus E and Poisson's ratio υ. In terms of these constants the matrices in Hook's law are as follows [56]:

$$[C]=\frac{E}{(1+\upsilon)(1-2\upsilon)}\times\begin{bmatrix} 1-\upsilon & \upsilon & \upsilon & 0 & 0 & 0 \\ \upsilon & 1-\upsilon & \upsilon & 0 & 0 & 0 \\ \upsilon & \upsilon & 1-\upsilon & 0 & 0 & 0 \\ 0 & 0 & 0 & \frac{1-2\upsilon}{2} & 0 & 0 \\ 0 & 0 & 0 & 0 & \frac{1-2\upsilon}{2} & 0 \\ 0 & 0 & 0 & 0 & 0 & \frac{1-2\upsilon}{2} \end{bmatrix} \tag{4.2}$$

$$[D]=[C]^{-1}=\frac{1}{E}\begin{bmatrix} 1 & -\upsilon & -\upsilon & 0 & 0 & 0 \\ -\upsilon & 1 & -\upsilon & 0 & 0 & 0 \\ -\upsilon & -\upsilon & 1 & 0 & 0 & 0 \\ 0 & 0 & 0 & 2(1+\upsilon) & 0 & 0 \\ 0 & 0 & 0 & 0 & 2(1+\upsilon) & 0 \\ 0 & 0 & 0 & 0 & 0 & 2(1+\upsilon) \end{bmatrix} \tag{4.3}$$

For all three models, an existing material model was employed: the C3D20R material type 20-node quadratic brick, reduced integration element. The 3D mesh was shown in Figure 4.5. For the model with 2 mm of ice this quarter-symmetric model has 2364 solid elements and 12424 nodes. As aforementioned, the linear static structural analysis requires specification of Young's modulus, which is $E = 9000$ MPa for the ice and $E = 70000$ MPa for the aluminum, and Poisson's ratio, which is $\upsilon = 0.31$ for the ice and $\upsilon = 0.34$ for the aluminium respectively. One solid, homogenous section is used to assign material properties to the elements.

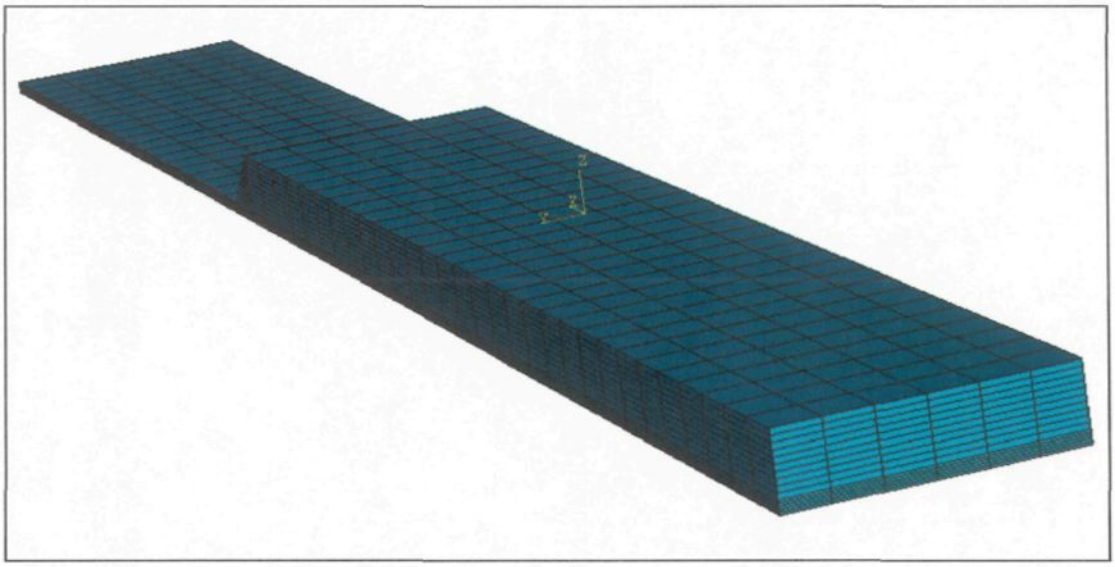

Figure 4.5: Mesh of the model with 2 mm of ice.

Figure 4.6 shows the von Mises stress distribution in the aluminium plate. It can be seen that the highest value is located near the points where the force is applied and is lower that the first yield stress of this material. It should be noted that this stress has no significance and is due to the load discretization. Assuming that bending occurring in the specimen generates critical stresses located at mid-length, all the next results are monitored along a path as shown in Figure 4.7.

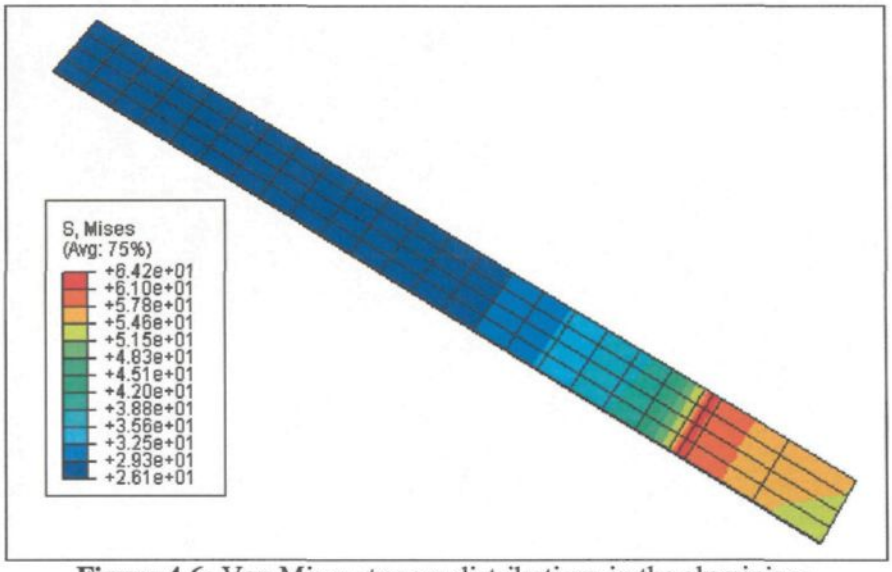

Figure 4.6: Von Mises stresses distributions in the aluminium.

Figure 4.8 shows the axial normal stresses in the specimen. The obtained results are compared with the results of theoretical model (Figure 3.4) and experimental results. Figure 4.8 shows that the maximum value of stress is related to the lower point of the aluminium plate (where the distance is zero). Then stress decreases until the ice part in which the neutral axis is located. Before this level, the ice is in traction, whereas after the neutral axis (abbreviated N.A. in Figure 4.8), the ice is in the compression area. It is obvious that the ice fibres above the neutral axis will decrease in length, whereas the ice fibres below the neutral axes will increase in length. In other words, $(0.63/2)=0.315\times100=31.5$ percent of the top ice grains shorten and are thus in compression, while 68.5 percent of the bottom fibres lengthen and are therefore in traction. Figure 4.9 shows that the strain distribution is already linear with respect to the continuum.

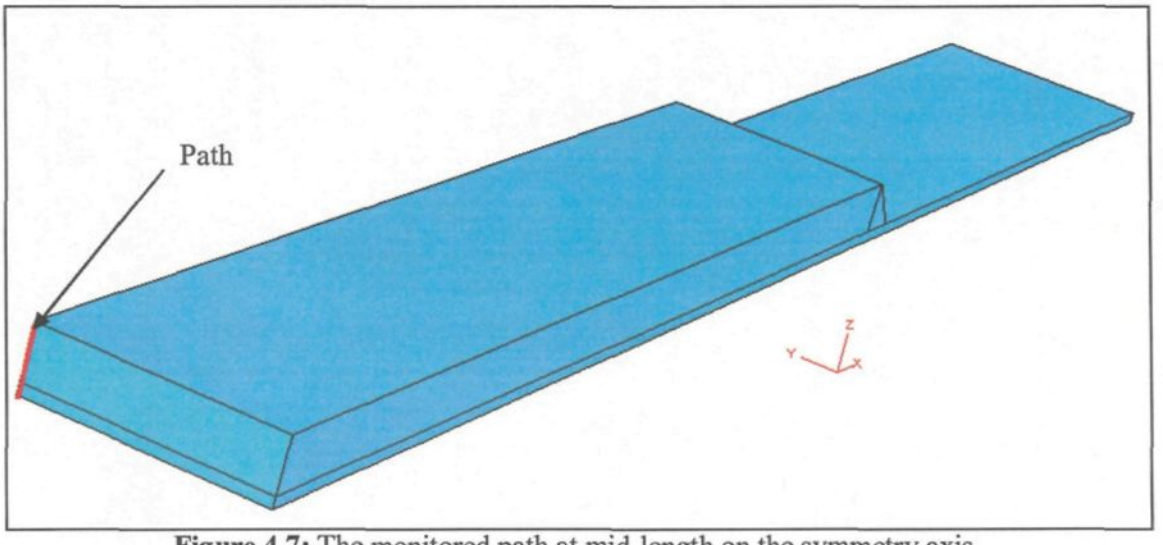

Figure 4.7: The monitored path at mid-length on the symmetry axis.

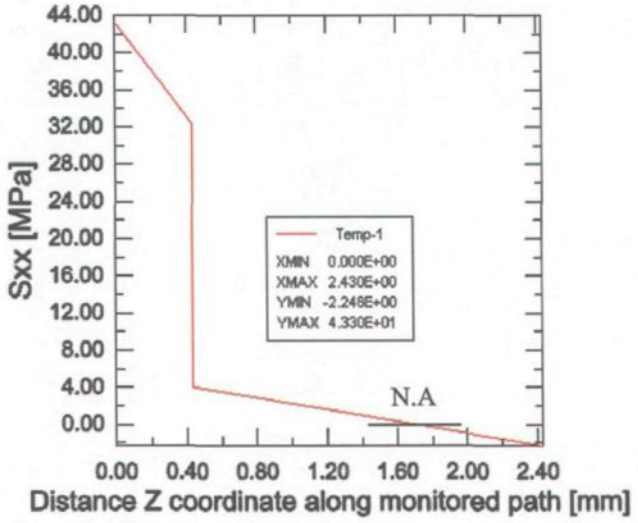

Figure 4.8: Axial stress distribution along the monitored path for 2 mm of ice.

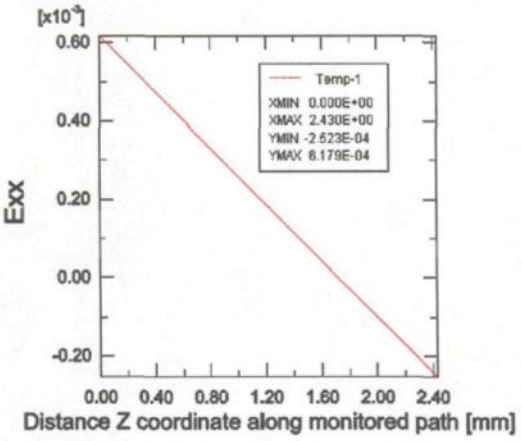

Figure 4.9: Strain distribution along the monitored path for 2 mm of ice.

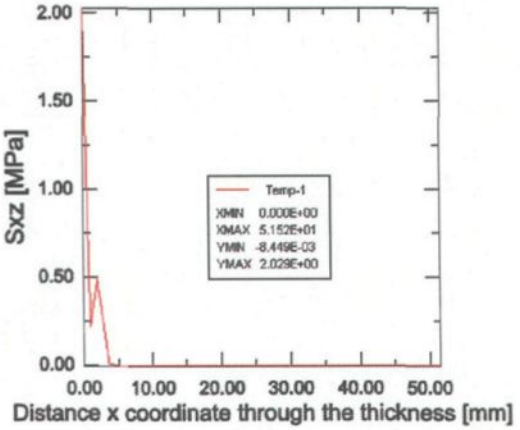

Figure 4.10: Shear stress (S_{xz}) through the thickness of ice (2 mm).

Figures 4.10 and 4.11 show the longitudinal shear stress (S_{xz}) graph and a contour plot of shear stress (S_{xz}) through the thickness of ice, respectively. The maximum shear stress of 2.08 MPa (appears in red in the figure) occurs at the front of the ice mass (at the beginning of the ice accumulation). It is believed that these longitudinal shear stresses have a significant influence on the development of cracks once they reach a certain depth.

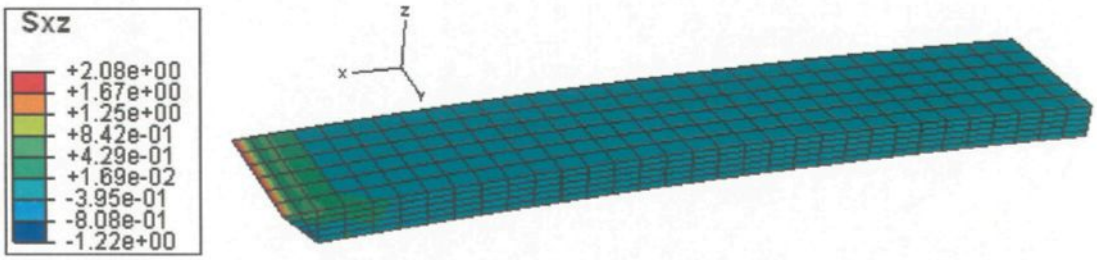

Figure 4.11: Longitudinal shear stress (S_{xz}) through the thickness of ice (2 mm).

For the model with 5 mm of ice, the actual load is F = 329.20 N (see Figure 2.9). Because of the symmetric condition, a uniform pressure load of 40.59 MPa is applied on one-quarter of the model. The mesh is considered fine as shown in Figure 4.12 and the number of elements and nodes are 7200 and 34866 respectively.

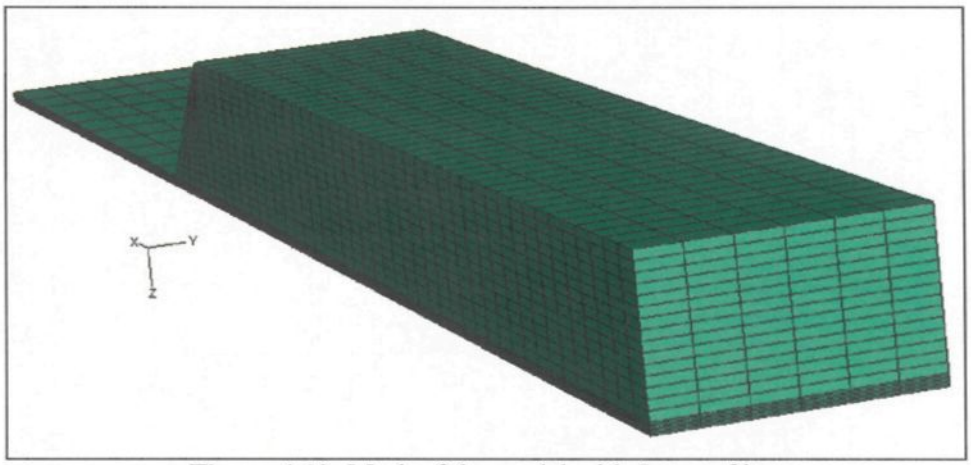

Figure 4.12: Mesh of the model with 5 mm of ice.

The axial normal stress (S_{xx}) distribution along the monitored path is shown in Figure 4.13. This figure shows that stress decreases when the ice thickness increases. This is due the increase of the global stiffness of the specimen. Figures 4.14 (a) and 4.14 (b) show the longitudinal shear stress (S_{xz}) graph and a contour plot of shear stress (S_{xz}) through the thickness of ice, respectively. The maximum shear stress of 1.90 MPa (appears in red in the figure) occurs at the front of the ice mass (at the beginning of the

ice accumulation). It is believed that these longitudinal shear stresses have a significant influence on the development of cracks once they reach a certain depth.

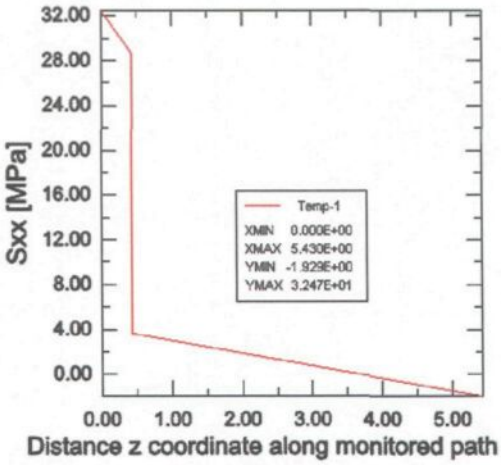

Figure 4.13: Axial stress distribution along the monitored path for 5 mm of ice.

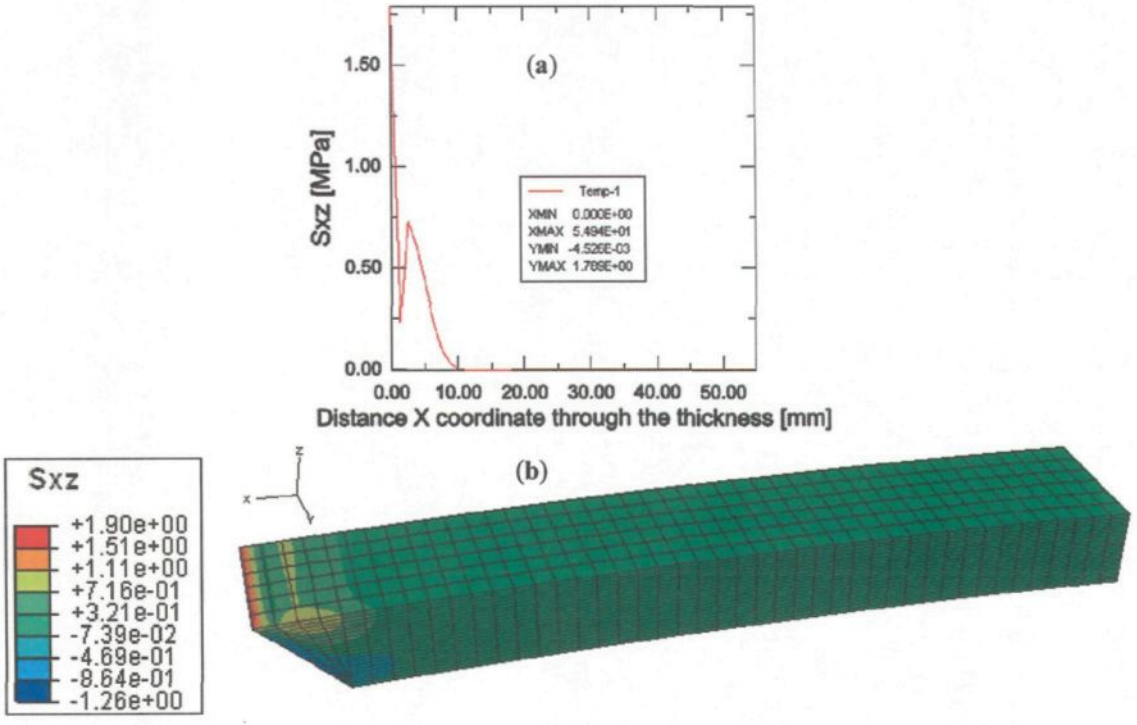

Figure 4.14: Longitudinal shear stress (S_{xz}) through the thickness of ice (5 mm). a) Shear stress (S_{xz}) graph. b) Contour plot showing the shear stress (S_{xz}).

Finally, for the model with 10 mm of ice, the ice beam and aluminium plate were modeled using 13350 elements. The mesh for this case is shown in Figure 4.15. The actual load is F = 297.63 N (see Figure 2.10). Because of the symmetric condition, a uniform pressure load of 36.70 MPa is applied on one-quarter of the model. The axial normal stress (S_{xx}) distribution along the monitored path is shown in Figure 4.16. As this figure shows, the stress decreases when the ice thickness increases. This is due to the increase of the global stiffness of the specimen.

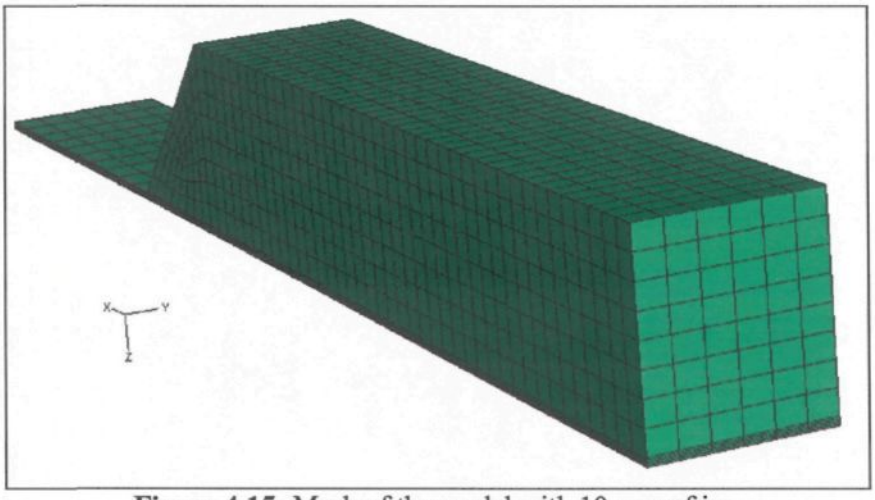

Figure 4.15: Mesh of the model with 10 mm of ice.

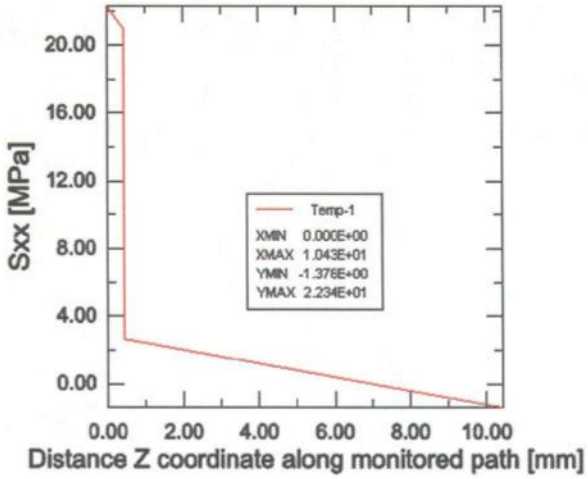

Figure 4.16: Axial stress distribution along the monitored path for 10 mm of ice.

For this case also, the longitudinal shear stress (S_{xz}) graph and a contour plot of shear stress (S_{xz}) through the thickness of ice are shown in Figures 4.17 (a) and 4.17 (b) respectively. The maximum shear stress of 1.77 MPa (appears in red in the figure) occurs at the front of the ice mass (at the beginning of the ice accumulation). It is believed that these longitudinal shear stresses have a significant influence on the development of cracks once they reach a certain depth.

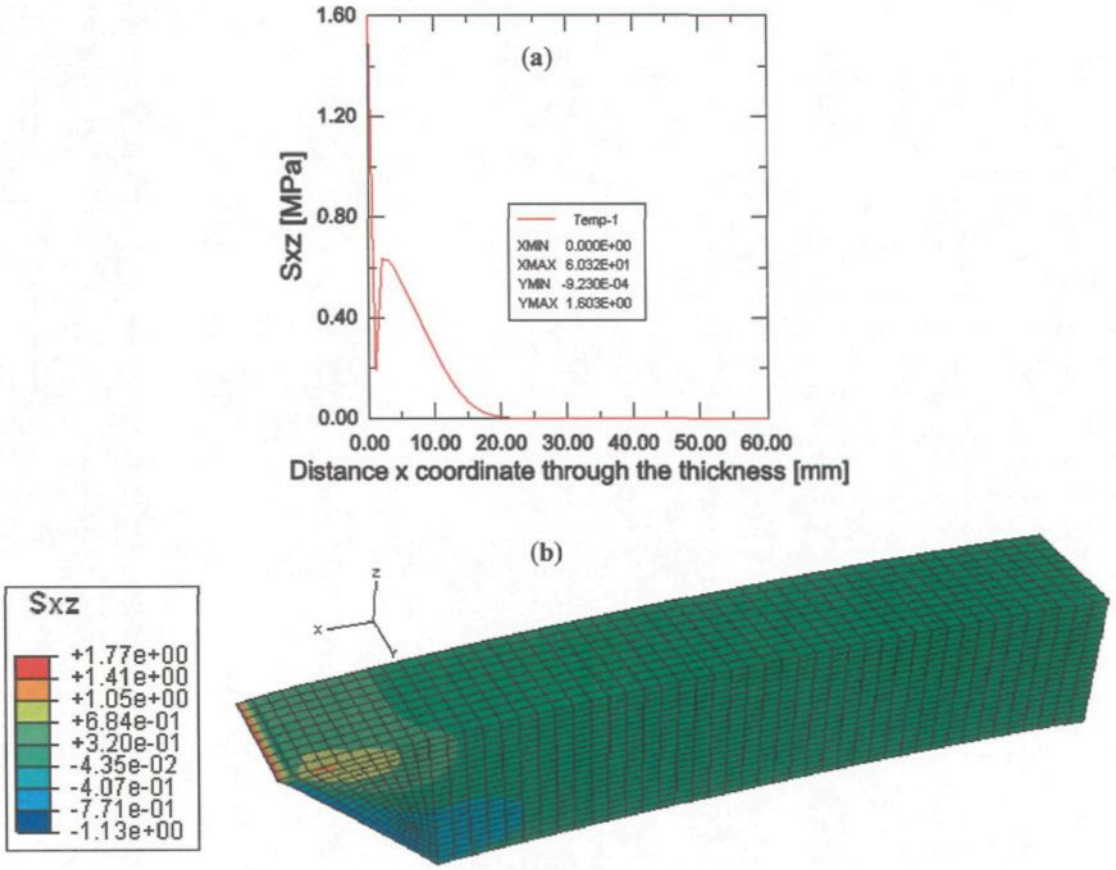

Figure 4.17: Longitudinal shear stress (S_{xz}) through the thickness of ice (10 mm). a) Shear stress (S_{xz}) graph. b) Contour plot showing the shear stress (S_{xz}).

4.2.4 The non-linear approach

A nonlinear structural problem is one in which the structure's stiffness changes as it deforms. All physical structures are nonlinear. Linear analysis is a convenient approximation that is often adequate for design purposes. It is obviously inadequate for many structural simulations, such as forging, stamping, or crash analyses. There is a range of solid mechanics situations in which such phenomena as plasticity, creep or other complex constitutive relations supersede the simple linear elasticity assumptions. Since the response of a nonlinear system is not a linear function of the magnitude of the applied load, it is not possible to create solutions for different load cases by superposition. Each load case must be defined and solved as a separate analysis. There are three sources of nonlinearity in structural mechanics simulations:

1) Geometry (nonlinear relations between strain and displacement components);
2) Material (nonlinear relations between stress and strain components);
3) Boundary conditions.

4.2.4.1 Basic results for geometrical nonlinearity

The first source of nonlinearity is related to changes in the geometry of the model during the analysis. Geometric nonlinearity occurs whenever the magnitude of the displacements affects the response of the structure. This may be caused by various aspects, such as large deflections or rotations and snap, through initial stresses or load stiffening. In our problem, because bending occurs on aluminium plate, it would be interesting to investigate the influence of the geometrical nonlinearity on the solution. Considering the effect of geometric nonlinearity, in this simulation the plate gets stiffer as

it deforms due to bending effects. Therefore, as shown in Figure 4.18, the resulting displacement is less than that predicted by the linear analysis, which did not include the geometric nonlinearity effect. This can be done by changing the definition on the strain tensor using its full definition such that:

$$\varepsilon_x = \frac{\partial u}{\partial x} + \frac{1}{2}\left[\left(\frac{\partial u}{\partial x}\right)^2 + \left(\frac{\partial v}{\partial x}\right)^2 + \left(\frac{\partial w}{\partial x}\right)^2\right] \tag{4.4}$$

where u, v and w are the scalar components of the displacement field. In the case of small displacement, the second order terms vanished. Using this strain definition, the problem must be solved using a non-linear approach such as the Newton-Raphson solution technique. This method is available in ABAQUS and needs other information such as the time step, the number of load step and the accuracy of the solution.

Incorporating the effects of geometric nonlinearity in an analysis requires only minor changes to the model. We need to make sure the step definition considers geometrically nonlinear effects. If the displacements in a model due to loading are relatively small during a step, the effects of geometric nonlinearity may be small enough to be ignored. However, in cases where the loads on a model result in large displacements, nonlinear geometric effects can become important. Therefore, with the same conditions, such as the same load, boundary conditions and meshing, the model considering the effects of geometric nonlinearity was analyzed and the results for each thickness of ice were obtained.

The Figure 4.19 shows the normal stress (S_{xx}) distribution along the monitored path regarding the geometrical non-linear solution for each model. For 2 mm of ice, Figure 4.19 (a) and Figure 4.8 (a) show that the maximum normal stress decreases from 43.30

MPa for linear solution to 33.16 MPa considering the geometrical nonlinearity for the model. Also, for 5 mm of ice, the maximum normal stress decreases from 32.47 MPa to 30.46 MPa (see Figures 4.13 and 4.19 (b)). Finally, for 10 mm of ice, Figures 4.16 and 4.19 (c) show the geometrical nonlinearity has a little effect on the maximum normal stress (from 22.34 MPa to 22.00 MPa). In fact, the influence of the nonlinear strains decreases when the ice thickness increases.

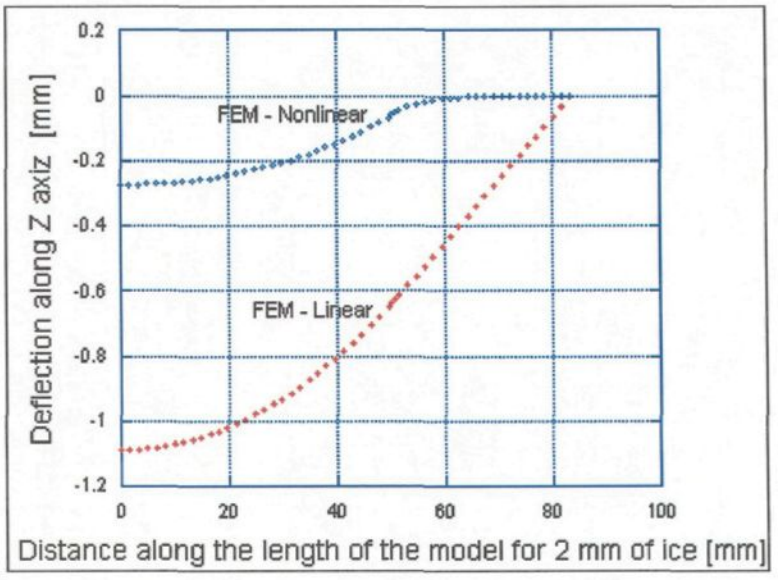

Figure 4.18: Influence of the non linear strain description on the deflection curve.

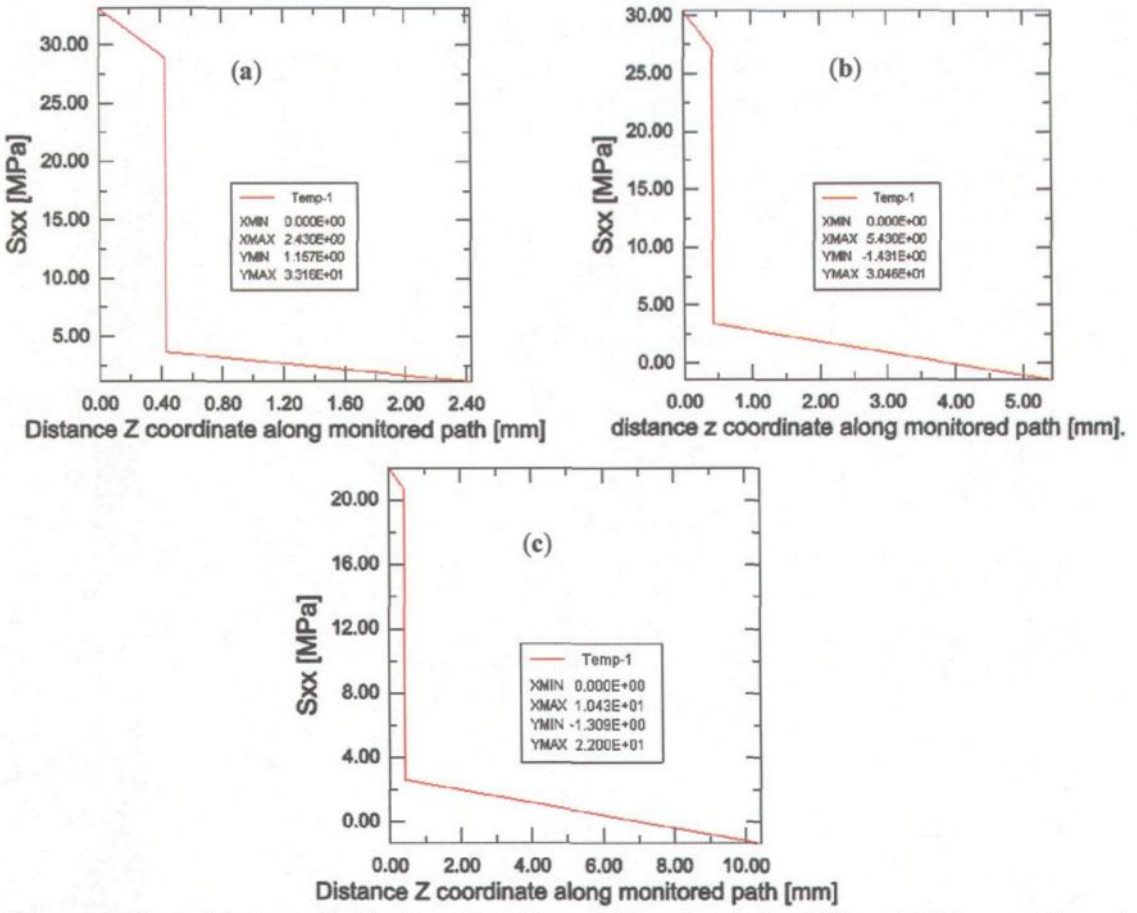

Figure 4.19: Axial stress distribution along the monitored path for different thickness of ice. a) 2 mm, b) 5 mm and c)10 mm.

Also, the longitudinal shear stress (S_{xz}) graph and a contour plot of shear stress (S_{xz}) through the thickness of ice have been shown in Figures 4.20 to 4.22 for each thickness of ice. As these figures show, the maximum shear stress in contour plots (appears in red in the figures) occurs at the front of the ice mass (at the beginning of the ice deposit). It is believed that these longitudinal shear stresses have a significant influence on the development of cracks once they reach a certain depth.

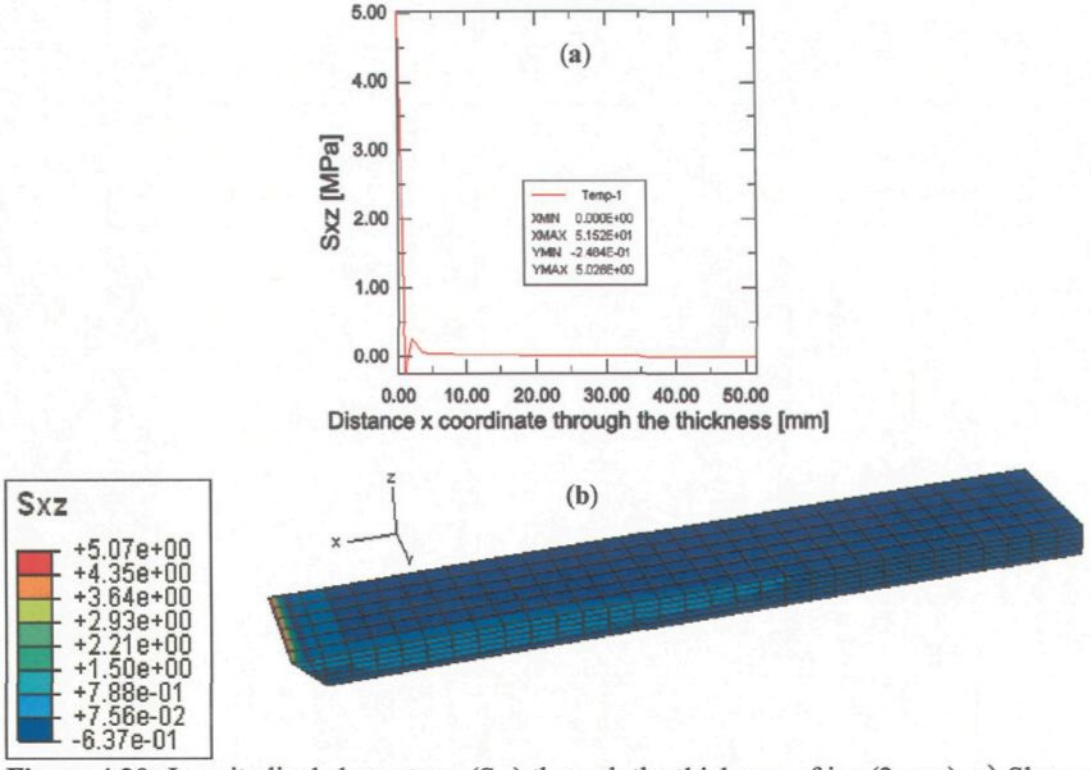

Figure 4.20: Longitudinal shear stress (S_{xz}) through the thickness of ice (2 mm). a) Shear stress (S_{xz}) graph. b) Contour plot showing the shear stress (S_{xz}).

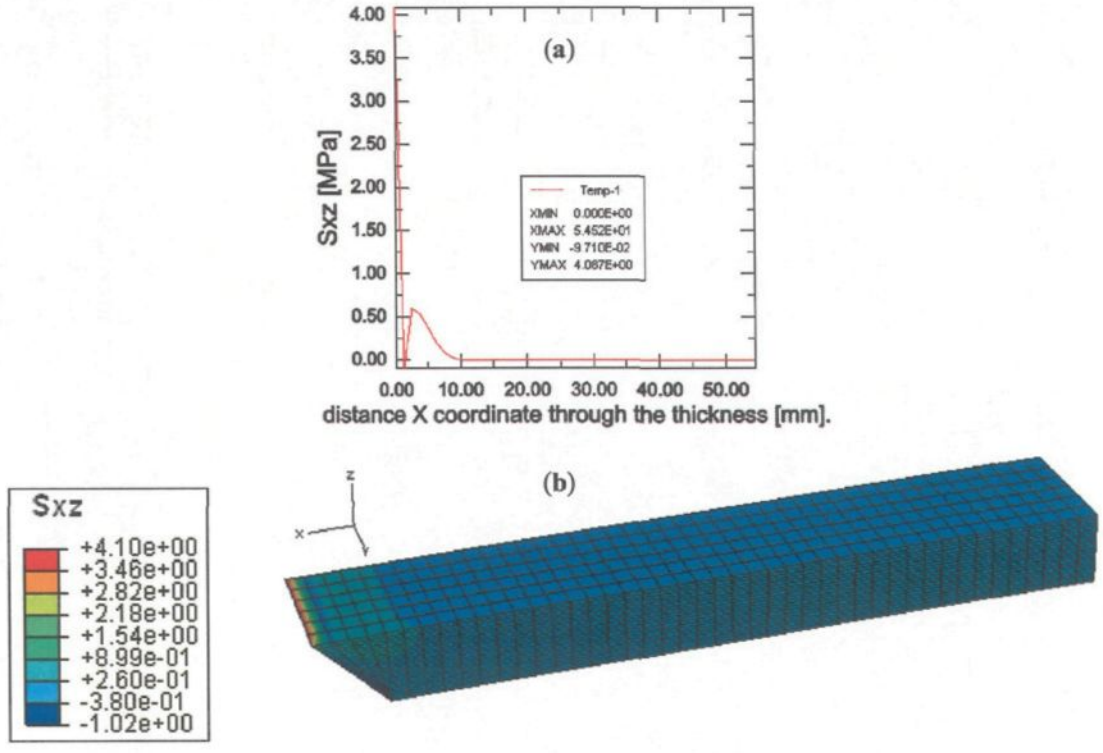

Figure 4.21: Longitudinal shear stress (S_{xz}) through the thickness of ice (5 mm). a) Shear stress (S_{xz}) graph. b) Contour plot showing the shear stress (S_{xz}).

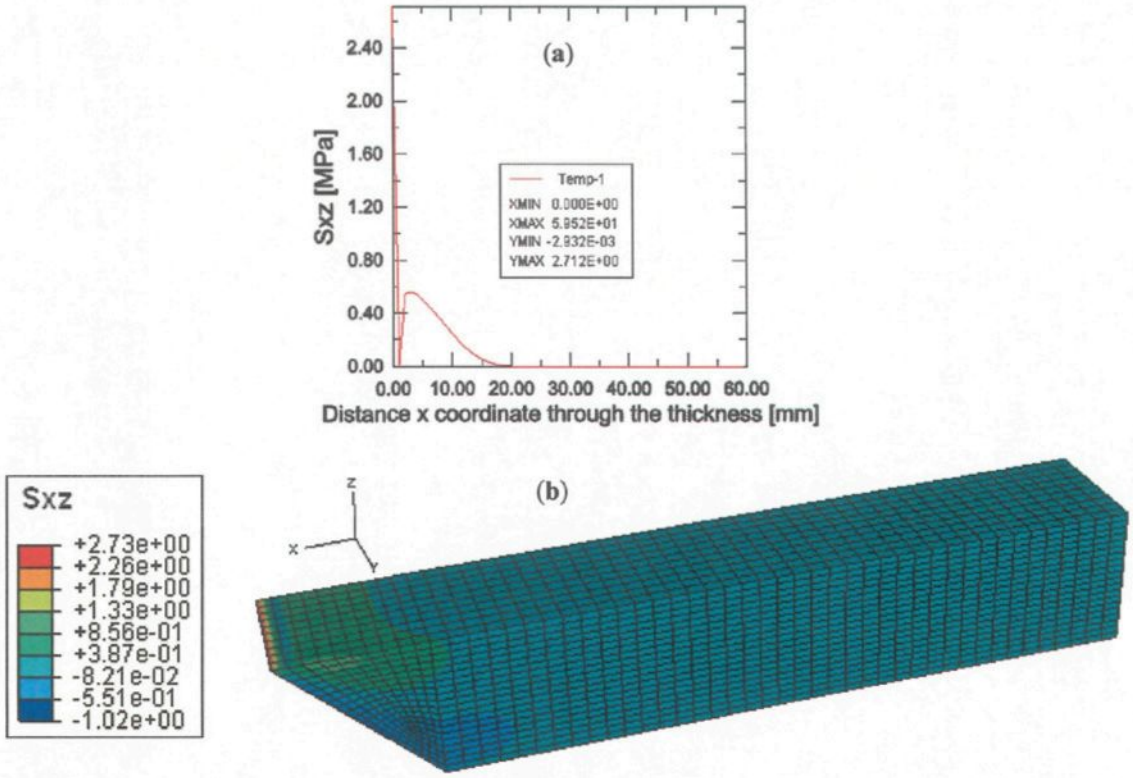

Figure 4.22: Longitudinal shear stress (S_{xz}) through the thickness of ice (10 mm). a) Shear stress (S_{xz}) graph. b) Contour plot showing the shear stress (S_{xz}).

4.2.4.2 Brittle cracking and cohesive material constitutive laws

As brittle cracking constitutive law described in detail in Section 3.3, under a high strain rate, ice behaves in a brittle manner and the main failure mechanisms are cracking in tension and crushing in compression. The brittle behaviour of ice can be characterized by elastic deformation followed by a sudden fracture. When a uniaxial specimen of ice is loaded into tension, its response is elastic until cracks form; this happens so quickly that it can be very difficult to observe the actual behaviour. For the purpose of modeling, using brittle cracking constitutive law, it is assumed that the ice is subjected to tension through a softening mechanism and that the open cracks can be represented by a loss of elastic stiffness. It is also assumed that the cracks can close completely when the stress

across them becomes compressive. The constitutive model for the ice consists of a compressive yield/flow surface to model the ice response in the predominantly compressive states of stress, together with damaged elasticity to represent cracks that have occurred at an integration point of the cross-section; the occurrence of cracks is defined by a crack detection failure surface and is considered part of elasticity [1].

Ice parameters

In ABAQUS two options must be used to define brittle cracking material. The BRITTLE CRACKING option must be used in conjunction with the BRITTLE SHEAR option, which must immediately precede it. So, the minimum input parameters required to define the ice material using this constitutive law when the TYPE = GFI is used in BRITTLE CRACKING option to define cracking and postcracking properties are the failure stress (σ_{tu}^{I}) and mode I fracture energy (G_f^I). Also, for the BRITTLE SHEAR option, when the TYPE=RETENTION FACTOR was selected to specify the postcracking shear behaviour by entering the shear retention factor–crack opening strain relationship directly, the Shear retention factor (ρ_{ck}) and Crack opening strain (ε_{nn}^{ck}) parameters must be used. Since the response is dominated by bending, it is controlled by the material behaviour normal to the crack planes. The material's shear behaviour in the plane of the cracks is not important. Consequently, the choice of shear retention has no significant influence on the results. In ABAQUS/Explicit the shear retention chosen is exhausted at the same value of the crack opening at which tension stiffening is exhausted [1].

This model considered ice behaviour to be predominantly governed by tensile cracking. As aforementioned, the model also assumed that the compressive behaviour is always linear elastic. This assumption was consistent with the observation of sample behaviour during the tensile test where the ice did not fail by crushing but rather separated by excessive tensile cracking due to bending. The basic ice properties were selected from the work of Michel [72] and brittle cracking parameters were assumed based on various literature and the final values were fixed after an admissible result was obtained. The final ice properties are given in Table 4.1. In this table the cracking failure stress is a value of maximum tensile strength of ice, which is about 1.4 MPa [83]. Mode I fracture energy was calibrated from the mean values obtained by different authors (see Table 3.2). The fracture energy of ice depends on the ice type and is relatively insensitive to loading rate, with less variation ascribable to grain size and temperature [8]. The methods for measurement of the fracture energy of ice and interface fracture energy of ice have been described in Appendix B and Appendix C respectively.

Table 4.1: Ice mechanical and brittle cracking properties used in the FE model.

Ice properties	**Values**
Density	897 (kg/m^3)
Elasticity modulus	9000 (MPa)
Poisson ratio	0.31
Cracking failure stress	1.4 (MPa)
Mode I fracture energy	7.11E-4, 2e-3 (N/mm)
Post-cracking shear behaviour model	Power law with 1.0 power factor

As cohesive material constitutive law described in detail in Section 3.4, the elastic properties of the interface material are defined using uncoupled traction-separation behaviour (for details see Section 3.4.2). The available traction-separation model in ABAQUS assumes:

1) Linear elastic behaviour (initially):

For using cohesive elements to model bonded interfaces, ABAQUS offers an elasticity definition that can be written directly in terms of the nominal tractions and the nominal strains. The nominal traction stress vector t, consists of three components (two components in two-dimensional problems) t_n, t_s, and (in three-dimensional problems) t_t, which represent the normal (along the local 3-direction in three dimensions and along the local 2-direction in two dimensions) and the two shear tractions (along the local 1- and 2-directions in three dimensions and along the local 1-direction in two dimensions), respectively. The corresponding separations are denoted by δ_n, δ_s and δ_t. Considering the original thickness of the cohesive element T_0, the nominal strains can be defined as:

$$\varepsilon_n = \frac{\delta_n}{T_0}, \varepsilon_s = \frac{\delta_s}{T_0}, \varepsilon_t = \frac{\delta_t}{T_0} \tag{4.5}$$

In the local element directions the stress-strain relations for uncoupled behaviour are as follows:

$$t = \begin{Bmatrix} t_n \\ t_s \\ t_t \end{Bmatrix} = \begin{bmatrix} K_{nn} & & \\ & K_{ss} & \\ & & K_{tt} \end{bmatrix} \begin{Bmatrix} \varepsilon_n \\ \varepsilon_s \\ \varepsilon_t \end{Bmatrix} = K\varepsilon \tag{4.6}$$

The quantities t_n, t_s , and t_t represent the nominal tractions in the normal and the two local shear directions, respectively, while the quantities ε_n, ε_s, and ε_t represent the corresponding nominal strains [1].

2) Initiation of damage:

As the name 'material damage initiation capability' implies, damage initiation refers to the beginning of the degradation of the response of a material point. The process of degradation begins when the stresses and/or strains satisfy certain damage initiation criterion that has been specified. Several damage initiation criteria are available and are used with cohesive elements to define damage initiation based on a maximum nominal stress or strain or a quadratic nominal stress or strain criterion. In our numerical model, a damage initiation based on the quadratic traction-interaction criterion for cohesive elements is chosen [1].

3) *Evolution of damage*:

The damage evolution capability is used with cohesive elements to define the fracture energy or displacement as a function of the mode mix of the deformation fields. Damage evolution law describes the rate at which the material stiffness is degraded once the corresponding initiation criterion is reached.

As described before, damage evolution can be defined based on the energy that is dissipated as a result of the damage process, which is also called the fracture energy. The fracture energy is equal to the area under the traction-separation curve (Figure 3.15). The fracture energy can be specified as a material property and either a linear or an exponential softening behaviour can be used. ABAQUS ensures that the area under the linear or the exponential damaged response is equal to the fracture energy.

The dependence of the fracture energy on the mode mix can be specified either directly in tabular form or can be defined based on a power law fracture criterion (power law form was used in our numerical model).

The power law criterion expresses that mixed-mode failure is governed by a power law interaction of the energies required to cause failure in the individual (normal and two shears) modes. It is given by:

$$\left\{\frac{G_n}{G_n^C}\right\}^{\alpha}+\left\{\frac{G_s}{G_s^C}\right\}^{\alpha}+\left\{\frac{G_t}{G_t^C}\right\}^{\alpha}=1 \tag{4.7}$$

with the mixed-mode fracture energy $G^C = G_n + G_S + G_t$ when the above condition is satisfied. In the above equation the quantities G_n, G_s, and G_t refer to the work done by the traction and its conjugate relative displacement in the normal, the first, and the second shear directions, respectively. Also, G_n^C, G_s^C, and G_t^C, are the quantities which refer to the critical fracture energies required to cause failure in the normal, the first, and the second shear directions, respectively [1].

Interface parameters

In ABAQUS, two options must be used to define cohesive material. The DAMAGE EVOLUTION option must be used in conjunction with the DAMAGE INITIATION option. The DAMAGE EVOLUTION option is used to provide material properties that define the evolution of damage leading to eventual failure. A mixed-mode, energy-based damage evolution law was used to define the evolution of damage (damage propagation) in terms of the energy required for failure (fracture energy) after the initiation of damage. The value of fracture energy G_f from Table 3.2 for the Ice/Al interfaces is 1.0 N/m. So, the normal mode fracture energy is $G_{IC} = 1.0E-3$ N/mm. The shear mode fracture energy for failure in the first and second shear directions G_{IIC} and G_{IIIC} was calibrated to

be 2 times G_{IC}. The DAMAGE INITIATION option is used to provide material properties that define the initiation of damage. The quadratic traction-interaction failure criterion was chosen for damage initiation. We only have the shear strength of the interface (adhesive shear strength of ice on aluminum surface is 1.52 MPa) [17], and not the peel strength (Peel strength is the average load per unit width of bond line required to separate bonded materials where the angle of separation is 180-degrees). The stress state inside the adhesive layer is always biaxial (shear-dominated). So, a value of peel strength some percentages (48 %) less than the shear strength was calibrated to be a good assumed value. The relevant cohesive material data are summarized in Table 4.2.

Table 4.2: Cohesive material properties used in the FE model for Ice/Al interfaces.

Abacus option	**Interface properties**	**Values**
Elastic type = traction	Cohesive layer modulus (penalty stiffness) in all 3 directions, K_{nn}, K_{ss}, K_{tt}	1.0E6 (N/mm^3)
Damage initiation, Criterion = quads	Ultimate strength in tensile, T	0.8 (N/mm^2)
	Ultimate strength in mode II, S	0.8 (N/mm^2)
	Ultimate strength in mode III, N	0.8 (N/mm^2)
Damage evolution, Type = energy	Normal mode fracture, G_{IC}	1.0 E-3 (N/mm)
	Shear mode fracture, G_{IIC}	2.0E-3 (N/mm)
	Shear mode fracture, G_{IIIC}	2.0E-3 (N/mm)

4.2.4.3 Solution techniques

Three-dimensional nonlinear FE modeling and analysis of an ice-coated beam was carried out in this part of study using the ABAQUS/Explicit solver because it has a brittle cracking model which is most suitable for modeling the tensile cracking of brittle materials. As aforementioned, the brittle cracking model is designed for applications in which the behaviour is dominated by tensile cracking. The model also allows automatic

removal of zero stress elements after cracking so the excessive distortion of that element and subsequent premature termination of the simulation can be avoided. In the preliminary development of the FE model, several material properties, particularly the ice cracking parameters, were tried to determine a suitable combination that produced acceptable results. The initial values of the cohesive material properties were chosen with trial and error based on several reported studies. The correctness of the FE model was checked by comparing the analysis results with the test data. Once the correct brittle cracking material properties and element size were obtained, the models were expanded to study the behaviour of interface with using cohesive material behaviour.

Because ABAQUS/Explicit is a dynamic analysis program, and in this case a quasi-static solution is desired, the model was loaded slowly enough to eliminate any significant inertia effect. There are two ways to obtain a quasi-static solution with an explicit dynamic procedure: to increase the loading rates and to perform mass scaling. Using the first technique, loading rate can be increased incrementally until it is judged that any further increase in loading rate would no longer result in a quasi-static solution. In the second technique, the material density is increased artificially, which leads to an increase of the stable time increment. One approach to determining the range to which the loading rate can be increased is to study the natural frequencies of the structure using ABAQUS/Standard module. In a static or quasi-static analysis the lowest eigenmode of a structure usually dominates the response. After the frequency and the corresponding time period of the lowest mode was obtained, the time required to obtain a quasi-static response can be estimated by a factor of 5 to10 times the period of the lowest eigenmode [1]. The load was applied by specifying a displacement value at the aluminium bottom

fibre nodes where the actual line load was acting. The displacement was increased linearly using a smooth amplitude function over a time step period of five times longer than the natural period of the structure. The natural period was obtained by performing eigenvalue frequency analysis, which is available in the ABAQUS/standard module equal to 328.40 Hz, which corresponds to a time period of 0.305 ms. An analysis time of 15 ms was found to be sufficient to ensure quasi-static loading. This was done to ensure that the quasi-static results were obtained. Longer loading periods can reduce dynamic effects but may increase analysis time significantly. An optimum analysis period was obtained after several trials.

Before any result was accepted, for all subsequent analyses the kinetic energy was compared with internal energy of the whole model throughout the analysis period to give a general indication whether quasi-static solution was obtained. The quasi-static response must be ensured by keeping the kinetic energy below 5 % of the internal energy at any instance during analysis and this was done by making adjustments (mass scaling factor and loading period). Mass scaling was done by increasing the density of the material by a factor of 100. The mass scaling used does not affect the results significantly; therefore, all subsequent analyses were performed using mass scaling.

The same boundary and symmetric conditions that used in the earlier analysis were used for all subsequent analyses. The interaction between the ice and the aluminium can only be modeled with 8-node three-dimensional cohesive elements (COH3D8). The ice beam and aluminium plate also were modeled with 8-node linear brick, and reduced

integration elements (C3D8R). The number of elements and degrees of freedom for each model are shown in Table 4.3.

Table 4.3: The number of elements and nodes for three models.

Model	Number of elements			Number of nodes	Degree of freedom
	ice	Al.	Coh.		
2 mm	1002	1944	252	4487	13461
5 mm	2616	1944	264	6433	19299
10 mm	2208	1392	288	5355	16065

The loading was a displacement boundary condition imposed on the node at the side face of the aluminium plate. From the experimental results, it can be obtained that each displacement of 0.073 mm, 0.075 mm and 0.074 mm (for the models with 2 mm, 5 mm and 10 mm of ice respectively) imposes equal concentrated load which used in ABAQUS/standard analysis. For accuracy and efficiency, quasi-static analyses require the application of loading to be as smooth as possible to facilitate solution convergence. Sudden loading causes stress waves, which can induce noisy or inaccurate solutions. The smooth step was used to create smooth loading amplitude. Using only the initial and final data points, a displacement loading with smooth step can be applied and the intervening motion will be smooth [1].

The interface between the ice and aluminium was modeled by using a cohesive layer with zero thickness that shares nodes along the interface. The technique used to embed a cohesive layer with zero thickness was the embedding orphan mesh into a finite element by sharing nodes and building separate cohesive elements with zero thickness and then tied to surrounding finite elements. Using this technique, an orphan mesh was generated from the ice part, then a layer of cohesive element with zero thickness was

inserted into this mesh part, the cohesive element sharing node with the finite ice element on one side, and connected to the aluminium finite element on the other side. For each three thicknesses of ice, the analysis was performed by varying the displacement load. For each result, internal and kinetic energies of the whole model were plotted. The axial normal stress (S_{xx}) distributions along the monitored path for each model are shown in Figures 4.23 (a), 4.23 (b) and 4.23 (c).

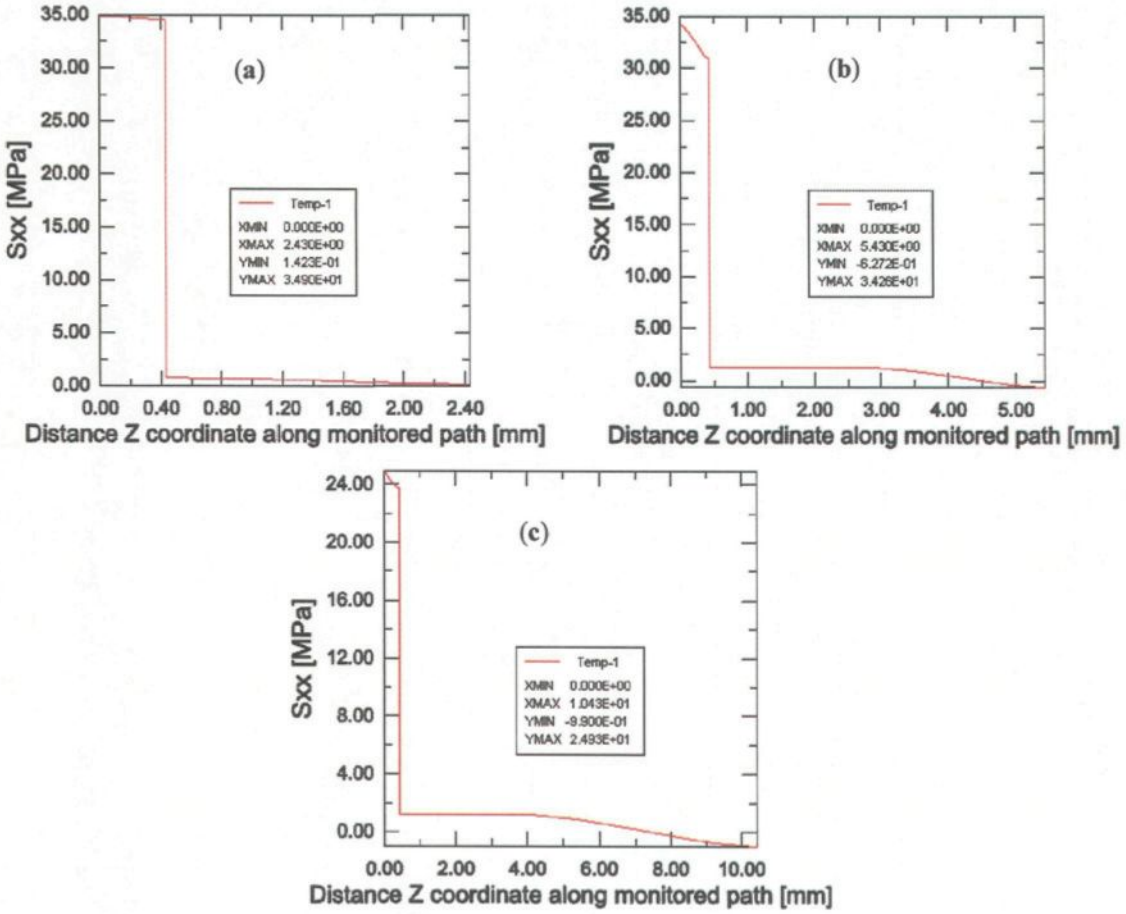

Figure 4.23: Axial stress distribution along the monitored path for different thickness of ice. a) 2 mm, b) 5 mm and c)10 mm.

As we expected, for the model with 2 mm of ice, delamination was not observed, and for the model with 5mm of ice a little delamination was observed. In the case of 10

mm of ice the model exhibited progressive delamination. A deformed plot of the finite element model for deformed models is shown in Figures 4.24 and 4.25.

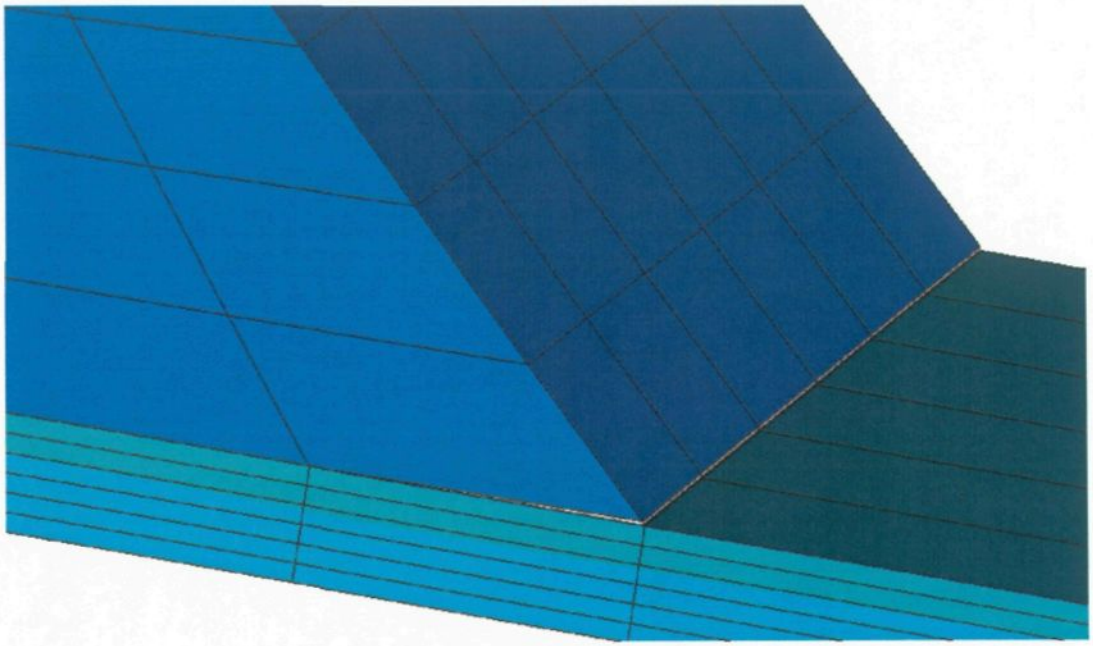

Figure 4.24: Deformed plot of model (5 mm).

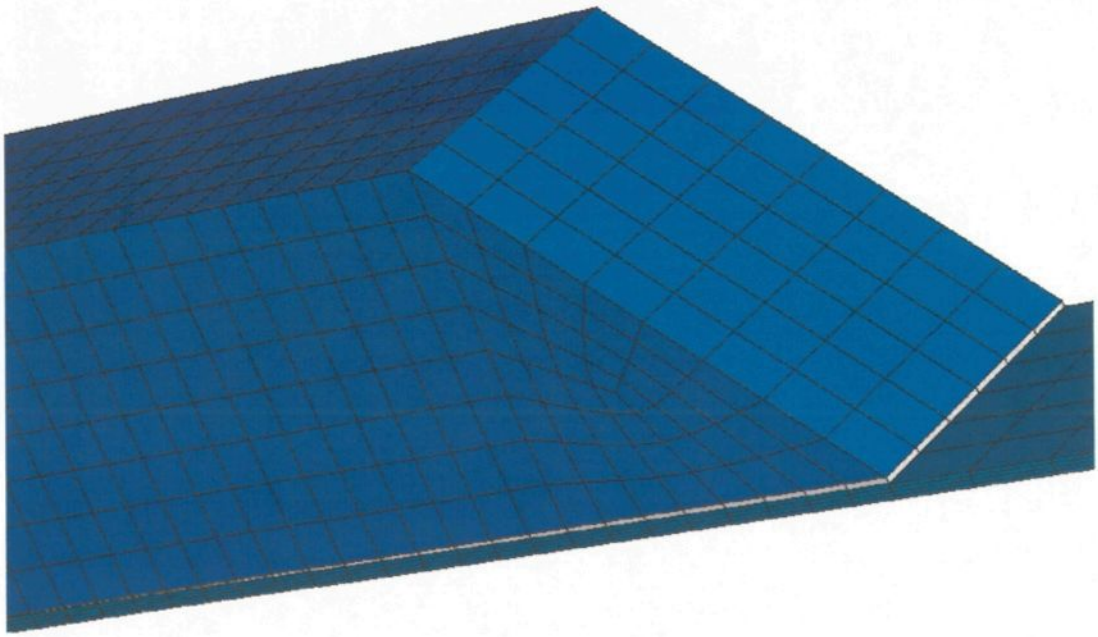

Figure 4.25: Deformed plot of model (10 mm).

Also, the longitudinal shear stress (S_{xz}) graph and a contour plot of shear stress (S_{xz}) through the thickness of ice for this case are shown in Figures 4.26 to 4.28 for each thickness of ice. As these figures show, the maximum shear stress in contour plots (appears in red in the figures) occurs at the onset of delamination growth. It is believed that these longitudinal shear stresses have a significant influence on the development of cracks once they reach a certain depth.

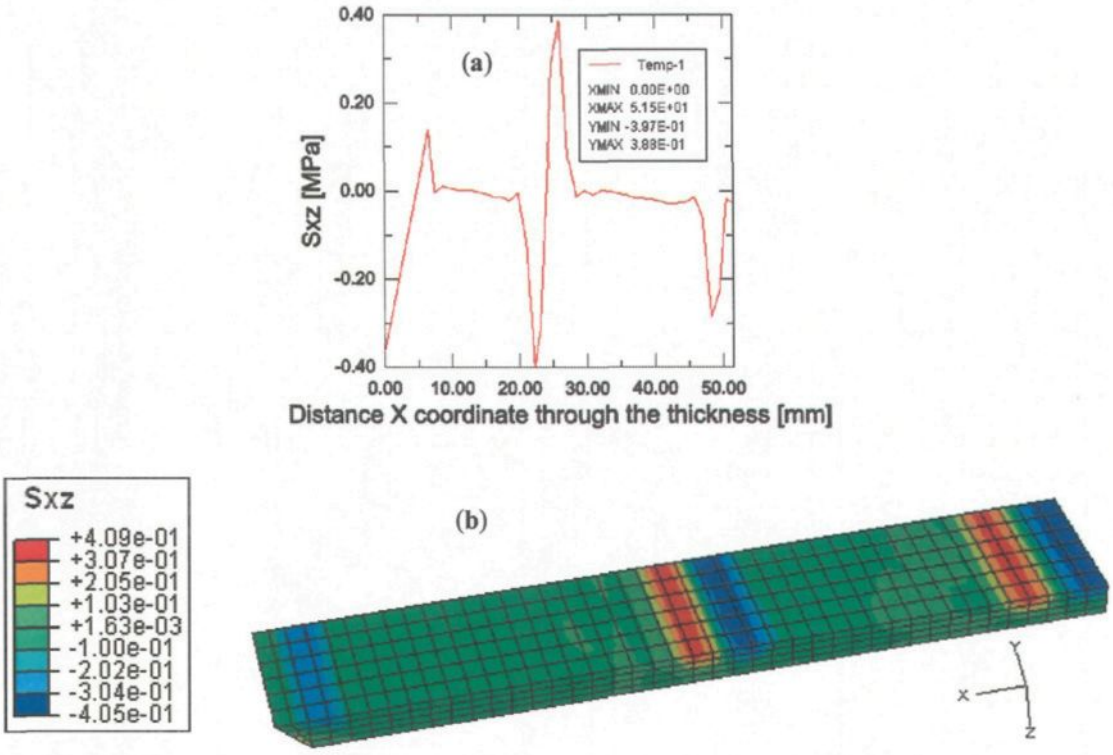

Figure 4.26: Longitudinal shear stress (S_{xz}) through the thickness of ice (2 mm). a) Shear stress (S_{xz}) graph. b) Contour plot showing the shear stress (S_{xz}).

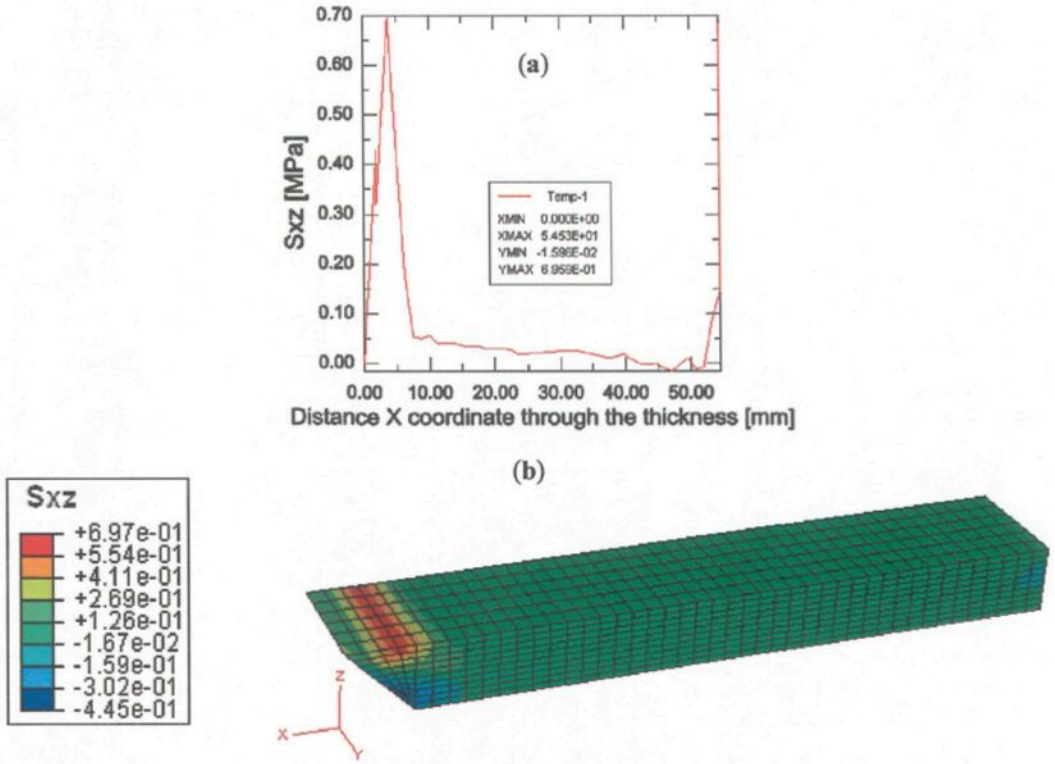

Figure 4.27: Longitudinal shear stress (S_{xz}) through the thickness of ice (5 mm). a) Shear stress (S_{xz}) graph. b) Contour plot showing the shear stress (S_{xz}).

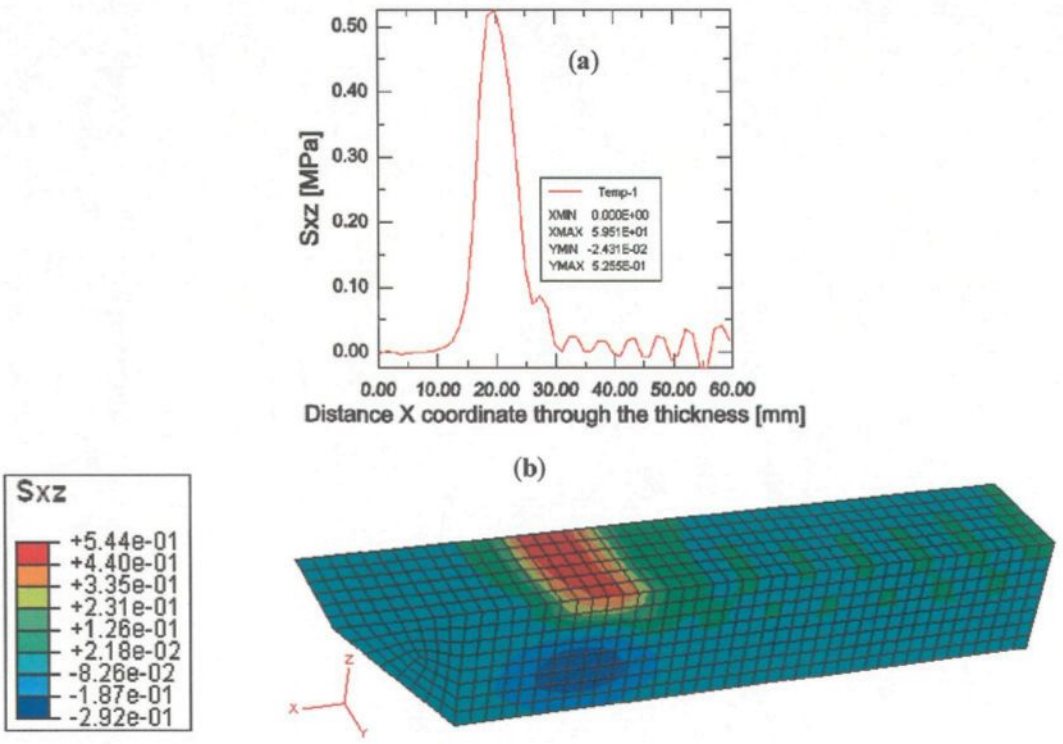

Figure 4.28: Longitudinal shear stress (S_{xz}) through the thickness of ice (10 mm). a) Shear stress (S_{xz}) graph. b) Contour plot showing the shear stress (S_{xz}).

As aforementioned, the quasi-static response was assured by keeping the kinetic energy level below 5% of the internal energy level. However, because ABAQUS/Explicit is a dynamic analysis program, oscillating response was inevitable even in the quasi-static solution. The quasi-static results were generally obtained when the time step periods were longer by 5 or more times than the model natural period. The results were then smoothed, using the smoothing function available in ABAQUS, in order to eliminate the oscillation effect. So, as a strategy for evaluating the results, we need to determine whether or not the solution is close enough to being quasi-static to be acceptable. One good approach is to compare the kinetic energy history to the internal energy history. To indicate an acceptable quasi-static solution, the kinetic energy of the model should be no greater than a few percent of the internal energy (typically 5% to 10%). Figure 4.29 shows the ratio of kinetic energy to internal energy is quite small and appears to be acceptable.

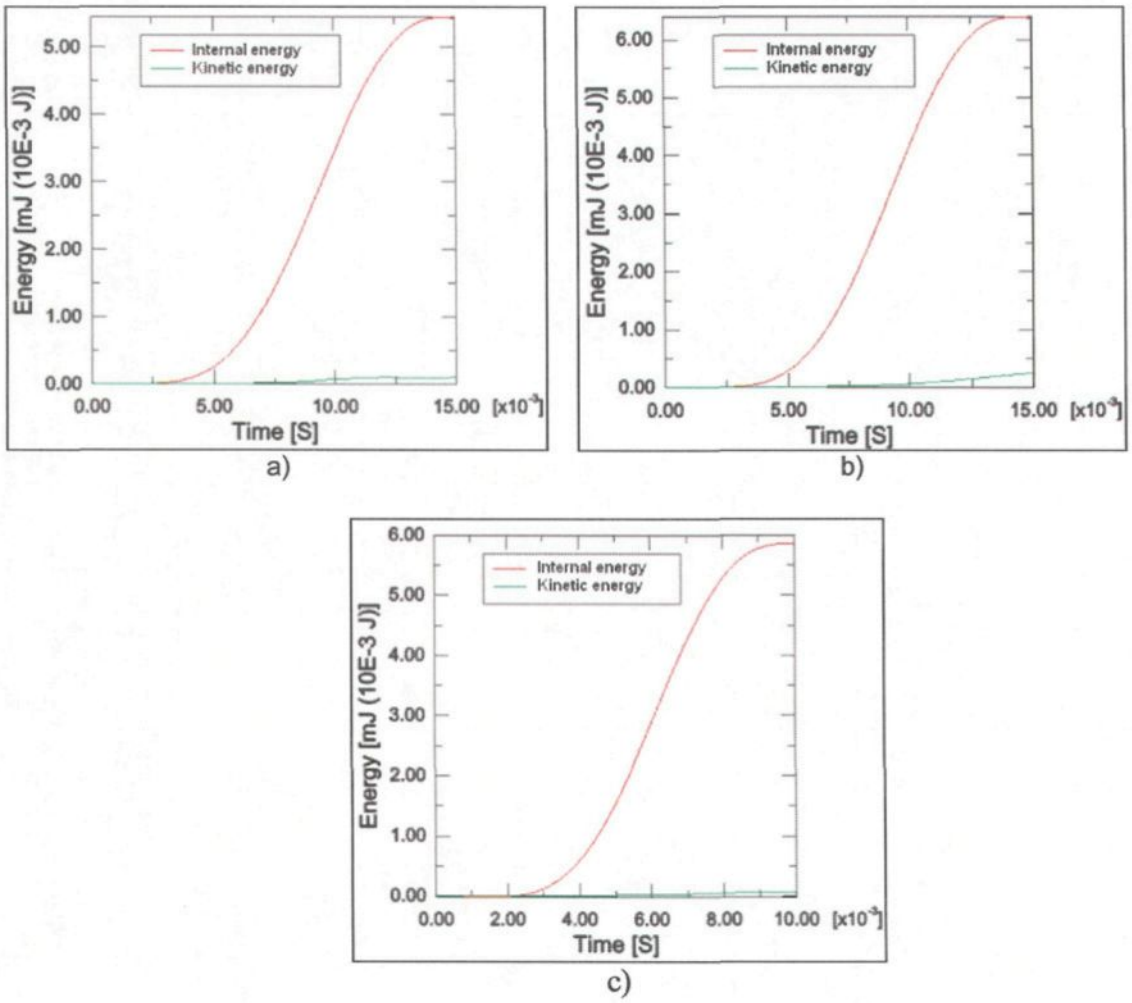

Figure 4.29: Time history of kinetic and internal energies of the model a) 2 mm of ice, b) 5 mm of ice and c) 10 mm of ice.

4.3 Results and discussion

For the case of ice with 2 mm from the experimental test the value of ε_{xx} is 0.000529 (see Figure 2.8). According to Hook's law, the obtained value of normal stress is: $\sigma_{xx} = E_{al}\varepsilon_{xx} = 70000\times\ 0.000529 = 37.03$ MPa. Also, at mid-length over the thickness of the model, the value of normal stress σ_{xx} from the theoretical model, linear FEM, geometrical nonlinear model and completed model (brittle cracking, cohesive material and geometrical nonlinearity) is 43.27, 43.30, 33.16 and 34.90 MPa, respectively (see

Figures 3.4 (a), 4.8, 4.19 (a) and 4.23 (a)). To compare the results of the experimental tests with theoretical model and FEM models, these results are shown in Table 4.4.

Table 4.4: Comparative results along the monitored path.

Thickness (mm)	Force (N)	Normal stress σ_{xx} at bottom face in Al (MPa)				
		Experimental	Theoretical	FEM (linear)	FEM (nl.geom.)	FEM (Brit./coh)
2	343.35	37.03	43.27	43.30	33.16	34.90
5	329.20	35.21	32.44	32.47	30.46	34.26
10	297.63	26.25	22.27	22.34	22.00	24.93

Also, the longitudinal shear stress (S_{xz}) results are summarized in Table 4.5. These results will be compared with the average value of shear stress for ice/Al equal to 0.47 ± 0.06 MPa from AMIL's centrifuge ice adhesion reduction tests [48].

Table 4.5: Longitudinal shear stress (S_{xz}).

Thickness (mm)	Force (N)	Longitudinal shear stress (S_{xz}) through the ice (MPa)			
		Theoretical	FEM (linear)	FEM (nl.geom.)	FEM (Brit./coh)
2	343.35	4.53	2.08	5.07	0.41
5	329.20	4.16	1.90	4.10	0.69
10	297.63	3.62	1.77	2.73	0.54

The results from Table 4.4 show that the results from the theoretical model (linear elastic model) are the same as the results from the linear numerical model. However, they are different from experimental results. Also, the results from the nonlinear models approach those of the experimental results. It has also been found that with increasing the thickness of ice the maximum value of σ_{xx} decreases. It can be proved by considering that with increasing the thickness of the ice the values of area (A), moment of inertia (I),

applied bending moment (M) and distance from the natural axis (y) increase. By substituting these values into the equation $\sigma_x = \frac{P}{A} - \frac{My}{I}$ the maximum value of normal stress decreases.

Differences between the linear FEM model and the experimental results can be explained by the fact that the adherence and the cohesion between the ice and substrate as well as the nonlinear behaviour of ice have not been expressed with linear FEM model. Therefore, as already pointed out, to obtain good results in a better and more realistic model, material nonlinear analyzing with the cohesive material approach was used. The results showed that:

1. The brittle cracking model in ABAQUS/Explicit can be used for modeling tensile ice cracking in ice-aluminium structures.
2. The cohesive material model in ABAQUS/Explicit can be used for modeling ice-aluminium interface.

Also, the results from Table 4.5 show that the values of shear stress from the model using brittle cracking and cohesive material is approximately the same value that was obtained from centrifuge ice adhesion reduction test in AMIL laboratory.

CHAPTER 5

CONCLUSIONS AND RECOMMENDATIONS

CHAPTER 5

CONCLUSIONS AND RECOMMENDATIONS

5.1 Summary and conclusions

Icing on structural surfaces is a subject of great interest in such problems as icing of electrical transmission cables, highways and bridges, constructions, off-shore structures, aircrafts and helicopters. Removal of ice coatings from these structures (de-icing) is necessary for their safe and reliable operations. Therefore, the exigency of the de-icing and anti-icing research filed seemed necessary. Consequently, the present study, carried out within the framework of the AMIL laboratory at the University of Quebec at Chicoutimi, aims to develop a three-dimensional model of ice/aluminium interface in order to determine the mechanical interactions of the interface between ice and aluminium. A number of tensile tests based on different thicknesses of ice at high strain rate were carried out in order to obtain the initial model parameters and to validate the performance of the model. Ice is a material which is very sensitive to loading rate, temperature, and other factors such as grain size, porosity and crystalline orientation. For this reason, ice is a material for which mechanical properties are still currently under investigation.

Experimental tests were performed under monotonic loading conditions in tension, to evaluate the de-icing mechanisms between the ice and substrate. Under the testing

conditions (high strain rate), the fracture mode was a mixture of adhesive and cohesive fractures, with the adhesive fracture dominant for ice thickness equal to 10 mm and the cohesive fracture dominant for ice thickness equal to 2 mm.

The damage mechanisms in ice/aluminium constructions under uniaxial loading conditions have been investigated using experimental and numerical approaches. Numerical finite element models have been created and executed and both geometric (large deformation) and material nonlinearities (brittle cracking) were included in the models and the cohesive material approach was used to define the interface between ice and aluminium. Firstly, linear and geometrically nonlinear simulations were performed. Then, using brittle cracking and cohesive material approach, results were found to be in good agreement with the experimental data.

The brittle cracking constitutive model has two key parameters to define cracking and postcracking properties: the failure stress (σ_{tu}^{I}) and mode I fracture energy (G_f^I). A new criterion for the simulation of both the initiation and propagation of fractures under combined normal and shear stresses using cohesive material was used for modeling the ice/aluminium interface. Zero-thickness cohesive elements were placed between the ice and the aluminium surface and they opened in response to the tensile loading. As an advantage of using the cohesive material approach, the onset of damage and the growth of delamination can be simulated without previous knowledge of the location, the size, and the direction of propagation of the delamination. The cohesive constitutive model has two key parameters that characterize the nonlinear response: the material toughness which equals the cohesive fracture energy, which is the external energy supply required to create and fully break a unit surface area of cohesive crack G_f, and the tensile strength

which is the stress at which the crack is created σ_c. Specified values for these key parameters, coupled with the shape for the traction–separation curve, define the separation attained at the peak stress δ_c, through Eq. (3.26).

The results from the model with 2 mm of ice showed that during simulation the stress levels are always below the values of stresses for damage initiation for the cohesive elements, which is why the elements never fail to investigate the onset of failure and delamination cannot be observed. For the two other models (5 mm and 10 mm), the stress levels exceeded the values of stresses for damage initiation for the cohesive elements and the delamination as observed in the experiments was simulated. This approach showed that the location and orientation of the initial transverse crack in the interface are dependent on the stress distribution in the critical area near the ice tip. A fracture mechanics approach was used to determine the potential for delamination growth from the initial transverse crack.

The results suggest that once a crack has initiated in the interface, a delamination will form and grow in an unstable manner between the cohesive layer and the top surface of the aluminium. A delamination for ice/aluminium interface for the model with 2 mm of ice requires more energy to initiate than was used for possible damage initiation for two other models.

The good agreement between the experimental and numerical results indicates that the proposed approach can capture the onset of delamination in an interface where the exact location of an initial crack may be difficult to determine a priori. It is concluded that the approach proposed here can be used in the failure prediction of ice-substrate structures when bending is the leading failure mechanism. Results from the finite element

simulations correlated reasonably well with the analogous experimental measurements performed using ice/aluminium specimens. The insights afforded by validated simulation allow the conclusions that the delamination damage form can significantly degrade an interface/structure's performance.

5.2 Recommendations and future works

Since using cohesive material theory to determine the interface between ice and aluminium was the first work in this domain, some recommendations are presented in order to improve mechanical parameters and numerical models. Further work is necessary to accurately model the effects of the parameters used to bond the adhesive (ice) and aluminium surface. In this work we considered that the mechanical properties of interface for different thickness of ice are the same, while the works of Wei et *al* [101] show that the fracture energy G_f increases monotonically when the relative upper beam thickness $h_{ice}/h_{substrate}$ increases. Some recommendations involving the present model may be listed as follows:

1. Develop an objective model for interface regardless the thickness of material.
2. Use this method to determine ice interface on various substrates like polymer materials and other metals.
3. It is also proposed that a new model be created using:
    a. Torsion tests to cylindrical specimens;
    b. Flexion tests; to ensure the objectively of the model.
4. Perform sensitivity analysis of parameters.

REFERENCES

References:

[01] ABAQUS V6.5 Users Manual.

[02] Aliyu, A.A. and Daniel, I.M. (1985); "Effects of strain rate on delamination fracture toughness of graphite/epoxy", ASTM STP **876**: 336–348.

[03] Anderson, T. L. (1995); "Fracture mechanics", CRC Press, p 88.

[04] Andersson, L.O., Lever, J.H., Mulherin, N.D. and Rand, J.H. (1991); "Proceedings of the 10th international conference on offshore mechanics and arctic engineering", Starvanger, Alaska, edited by Ayorinde, O.A., Sinha, N.K., Nixon, W.A., and Sodhi, D.S. (American society of mechanical engineers), **5**: 215.

[05] Andrews, E.H, Pingsheng He and Vlachos. C. (1982); "Adhesion of epoxy resin to glass", Proceedings of the royal society of London series A, mathematical and physical sciences, **381** (1781): 345-360.

[06] Andrews, E.H., and Lockington, N.A. (1983); "The cohesive and adhesive strength of ice", Journal of material science, **18** (55): 1455-1465.

[07] Andrews, R.M. (1985); "Measurement of the fracture toughness of glacier ice", Journal of glaciology, **31**: 171-176.

[08] Anstis, G.R., Chantikul, P., Lawn, B.R., and Marshall, D.B. (1981); "A critical evaluation of indentation techniques for measuring fracture toughness", Journal of the American ceramic society, **64**: 533-538.

[09] Archer, P., and Gupta, V. (1998); "Measurement and control of Ice adhesion to aluminum 6061 alloy," Journal of the mechanics and physics of solids, **46** (10):1745-1771.

[10] Barenblatt, G.I. (1963); "The mathematical theory of equilibrium cracks in brittle fracture", Advances in applied mechanics, **7**: 55.

[11] Barron, J. (1992); "Investigators sift for clues to crash at La Guardia", New York Times 24 March.

[12] Bathe, K. J. (1982); "Finite element procedures in engineering analysis", Prentice-Hall, Englewood Cliffs, 735 pp.

[13] Bažant, Z.P., and Planas, J. (1998); "Fracture and size effect in concrete and other quasi brittle materials", p 616.

[14] Beer, G. (1985); "An isoparametric joint/interface element for the finite element analysis," International Journal for numerical methods in engineering, **21**: 585–600.

[15] Bentley, D.L., Dempsey, J.P., Sodhi, D.S., and Wei, Y. (1989); "Fracture toughness of columnar freshwater ice from large scale DCB tests", Cold regions science and technology, **17**: 7-20.

[16] Blackburn C, Laforte C, Laforte JL. (2000); "Apparatus for measuring the adhesion force of a thin ice sheet on a substrate", In proceeding of the 9th international workshop on atmospheric icing of structures, Chester, UK.

[17] Boluk, Y. (1996); "Adhesion of freezing precipitates to aircraft surfaces", Transportation development. centre, TP 12860E, November.

[18] Camanho, P.P. and Dávila, C.G. (2002); "Mixed-Mode decohesion elements for the simulation of delamination in composite materials", NASATM- 2002-211737, Hampton VA.

[19] Camanho, P.P., Dávila, C.G., and Ambur, D.R. (2001); "Numerical simulation of delamination growth in composite materials", NASA-TP-211041. p 8.

[20] Carlsson, L. A, Gillespie, J. W., Jr., and Pipes, R. B. (1986); "On the analysis and design of the end notched flexure specimen for mode II testing", Journal of composite materials, **20**: 594-604.

[21] Carlos G. Davila and Pedro P. Camanho, (2001); "Decohesion elements using two and three-parameter mixed-mode criteria", AHS International structures specialists meeting, Williamsburg, Virginia, October 30-November 1, 2001.

[22] Charalambides, P.G., Lund, J., Evans, A.G., and McMeeking, R.M. (1989); "A test specimen for determining the fracture resistance of bimaterial interfaces", Journal of applied mechanics, **56** (1): 77-82.

[23] Currier, J.H., and Schulson, E.M. (1982); "The tensile strength of ice as a function of grain size", Acta metall., **30**: 1511–1514.

[24] Daniel Marceau, Mario FaFard, (1993) "Modélisation du contact bidimensionnel et axisymétrique en grands déplacements relatifs, et son application à l'étude du comportement des têtes d'ancrage mono-toron. Rapport GCT-93-09 Université Laval.

[25] Dempsey, J.P., DeFranco, S.J., Adamson, R.M., and Mulmule, S.V. (1999); "Scale effects on the in-situ tensile strength and fracture of ice. Part I: Large grained freshwater ice at Spray Lakes Reservoir", International journal of fracture, **95**: 325–345.

[26] Dempsey, J.P., DeFranco, S.J., Adamson, R.M., and Mulmule, S.V. (1999); "Scale effects on the in-situ tensile strength and fracture of ice. Part II: First-year sea ice at Resolute", International journal of fracture, **95**: 347–366.

[27] Döbert, C., Mahnken, R., and Stein, E. (2000); "Numerical simulation of interface debonding with a combined damage/friction constitutive model", Computational mechanics, **25**: 456-467.

[28] Druez, J. and Mccomber, P. (1989); Transactions of the Canadian society for mechanical engineering, **13**: 59.

[29] Dudgale, D.S. (1960); "Yielding of steel sheets containing slits", Journal of mechanics and physics of solids, **8**: 100-104.

[30] Evans, A.G., Ruhle, M., Dagleigh, B.J., and Charalambides, P.G. (1990); Metallurgical and materials transactions, 21A, 2419.

[31] Faraday, M. (1859); "On regelation, and on the conservation of force", Philosophical magazine, **17**: 162–9.

[32] Fischer, M.P., Alley, R.B., and Engelder, T. (1995); "Fracture toughness of ice and firn determined from the modified ring test", Journal of glaciology, **41**:383-394.

[33] Foundation engineering company of Canada (1949); "Model study of the Bromptonville ice jam", Internal report.

[34] Gold, L.W. (1963); "Crack formation in ice plates by thermal shock", Canadian journal of physics, **41**: 1712.

[35] Gold, L.W. (1988); "On the elasticity of ice plates", Canadian journal of civil engineering, **15**: 1080-1084.

[36] Goodman, D.J. (1980); "Critical stress intensity factor (KIc) measurements at high loading rates for polycrystalline ice", Physics and mechanics of ice (Edited by P. Tryde), Copenhagen, 129–146.

[37] Goodman, D.J., and Tabor, D. (1978); "Fracture toughness of ice: a preliminary account of some new experiments", Journal of glaciology, **21**(85): 651–660.

[38] Goodwin, E.J., Mozer, J.D., DiGioia, A.M. Jr., Power, B.A. (1982); "Predicting ice and snow loads for transmission lines", Proceedings of the first international workshop on atmospheric icing of structures, Hanover, USA, 267–273.

[39] Goyal, V.K., Johnson, E.R., Dávila, C.G. (2004); "Irreversible constitutive law for modeling the delamination process using interfacial surface discontinuities," Journal of composite structures, **65**: 289-305.

[40] Gupta, V., Yuan, J. and Pronin, A. (1994); "Recent developments in the laser spallation technique to measure the interface strength and its relationship to interface toughness with applications to metal/ceramic, ceramic/ceramic and ceramic/polymer interfaces", Journal of adhesion science and technology, **8**(6): 713-747.

[41] Haldar, A., Pon, C., Kastelein, M., and McComber, P. (1998); "Validation of ice accretion models for freezing precipitation using field data," Report CEA Contract No 331 T 992 (A-D), 166.

[42] Hawkes, I., and Mellor, M. (1972); "Deformation and fracture of ice under uniaxial stress", Journal of glaciology, **11**(61): 103–131.

[43] Haynes, F.D. (1978); "Effect of temperature on the strength of snow-ice", Department of the army, Cold regions research and engineering laboratory, Corps of engineers, CRREL Report 78-27.

[44] Hilleborg, A., Modeer, M. and Petersson, P. E. (1976); "Analysis of crack formation and crack growth in concrete by means of fracture mechanics and finite elements," Cement and concrete research, **6**: 773–782.

[45] Hobbs, P.V. (1974); "Ice physics" Clarendon press, Oxford.

[46] Hooke, R.L., et al. (1980); "Mechanical properties of polycrystalline ice", Cold regions science and technology, **3**: 263-275.

[47] Howard, S.J, Phillipps, A.J., and Clyne, T.W. (1993); "The interpretation of data from four-point bend testing to measure interfacial fracture toughness", Composites, **24**: 103-112.

[48] http://www.uqac.ca/amil/. (Anti-icing materials international laboratory, AMIL).

[49] Hutchinson, J.W., Mear, M. and Rice, J.R. (1987); "Crack paralleling an interface between dissimilar media", Journal of applied mechanics, **54**: 828-832.

[50] Idem, (1988); Journal of offshore mechanics and arctic engineering, **110**: 192.

[51] James, R. Reeder and John H. Crews Jr. (1990); "Mixed-mode bending method for delamination testing", AIAA Journal, Vol. 28, No. 7.

[52] Jellinek, H., (1967); "Liquid-like (transition) layer on ice," Journal of colloid and interface science, **25**: 192-205.

[53] Jellinek, H.H.G. (1958); "The influence of imperfections on the strength of ice", Proceedings of the physical society, **71**: 797-814.

[54] Jones, K.F. (1998); "A simple model for freezing rain ice loads," Atmospheric research, **46**: 87–97.

[55] Kanninen, M.F. (1973); "An augmented double cantilever beam model for studying crack propagation and arrest", International Journal of fracture, **9**: 83-92.

[56] Kenneth H. Huebner and Earl A. Thornton, (1995); "The finite element. method for engineers", 3rd Edition, Wiley & Sons, New York.

[57] Krueger, R., and T.K., O'Brien. (2001); "A shell/3D modeling technique for the analysis of delaminated composite laminates", Composites-Part A **32**: 25-44.

[58] Laflamme, J.N., Laforte, J.L., Allaire, M.A. (2002); "De-icing techniques before, during and following ice storms", Rapport No T003700-3303, The Canadian electricity consortium.

[59] Laforte, C., Laforte, J.L., and Carrier, J.C. (2002); "How a solid coating can reduce the adhesion of ice on a structure", Proceedings of the international

workshop on atmospheric icing of structures (IWAIS), 6.

[60] Laforte, J.L., Allaire, M.A., and Asselln, D. (1998); "State-of-art on power line de-icing", Atmospheric research, **46**: 143-158.

[61] Laforte, J.L., Allaire, M.A., Asselin, D. (1994) ; "État de l'art du déglaçage des conducteures et des câbles aériens", Grope de recherche en ingénierie de l'environnement atmosphérique. Université du Québec À Chicoutimi, Hydro-Québec, rapport HQ-04-01, ,207.

[62] Laforte., C. (2003); "Experimental tests document", AMIL laboratory.

[63] Landy, M., and Freiberger, A. (1967); "Studies of ice adhesion", Journal of colloid and interface science, **25**(2): 231–244.

[64] Lee, R.W., and Schulson, E.M. (1988); "The strength and ductility of ice under tension", Journal of offshore mechanics and arctic engineering, **110**: 187-191.

[65] Li, J., and Sen, J.K. (2000); "Analysis of frame-to-skin joint pull-off tests and prediction of the delamination failure, 42nd AIAA/ASME/ASCE/AHS/ASC structures", Structural dynamics and materials conference (Seattle, WA, U.S.A.).

[66] Liu, H.W., and Miller, K.J. (1979); "Fracture toughness of fresh-water ice", Journal of glaciology, **22**(86): 135–143.

[67] Lozowski, E.P., Stallabrass, J.R., and Hearty, P.F. (1983); "The icing of an unheated, nonrotating cylinder- Part I: A simulation model", Journal of climate and applied meteorology, **22**: 2053-2062.

[68] Lu, M.L, Oliver, P., Popplewell, N., Shah, A.H. (1999); "Predicting extreme loads on a power line from freezing rainstorms", International society of offshore and polar engineers, **2**: 594.

[69] Makkonen, L. (1984); "Modelling of ice on wires", Journal of climate and applied meteorology, **23**: 929-939.

[70] Makkonen, L. (1998); "Modeling power line icing in freezing precipitation", Atmospheric research, **46**: 131-142.

[71] Makkonen, L., and Lehmus, E. (1988); "Proceedings of 9th international conference on port and ocean engineering under arctic conditions", Fairbanks, Alaska, edited by. Sackinger, W.M., and Jefferies, M.O., (Geophysical institute, university of Alaska Fairbanks), **1**: 45.

[72] Michel, B., (1978); "Ice mechanics", Les Presses de l'Universite Laval, Quebec, Canada.

[73] Nixon, W.A., and Schulson, E.M. (1987); "A micromechanical view of the fracture toughness of ice", Journal de physique, **48**: 313-319.

[74] Petrovic, J.J. (2003); "Review mechanical properties of ice and snow", Journal of material science, **38**: 1–6.

[75] Poots, G., and Skelton, P.L.I. (1994); "Simple models for wet-snow accretion on transmission lines: snow load and liquid water content", International journal of heat and fluid flow, **15**: 411-417.

[76] Quezdou, M.B., Chudnovsky, A., and MOET, A. (1988); Journal of adhesion, **25**: 169.

[77] Raraty, L.E., and Tabor, D. (1958); "The adhesion and strength properties of ice", Proceedings of the royal society of London, **245A**: 184-201.

[78] Rice, J. R., and Sih, G. C., (1965); "Plane problems of cracks in dissimilar media", Journal of applied mechanics, **32**: 418-423.

[79] Rice, J.R. (1988); "Elastic fracture mechanics concepts for interfacial cracks", Journal of applied mechanics, **55**: 98-103.

[80] Rice, J.R. (1968); "A path independent integral and the approximate analysis of strain concentration by notches and cracks", Journal of applied mechanics, **35**: 379-386.

[81] Rots, J.G., Blaauwendraad, J. (1989); "Crack models for concrete: discrete or smeared? fixed, multi-directional or rotating? ", Heron, **34** (1): 1-59.

[82] Russel, A.J. (1982); "On the measurement of mode II interlaminar fracture energies", Victoria, B. C. Material report, 82-0.

[83] Schulson, E.M. (1999); "The structure and mechanical behaviour of ice", Journal of the minerals, metals, materials society, **51**: 21-27.

[84] Schulson, E.M., Baker, I., Robertson, C.D., Bolon, R.B., and Harnimon, R.J. (1989); "Fractography of ice", Journal of materials science letters, **8**: 1193–1194.

[85] Schulson, E.M., Lim, P.N., and Lee, R.W. (1984); "A brittle to ductile transition in ice under tension", Philosophical magazine, A **49**(3): 353–363.

[86] Schulson, EM. (1987); "The fracture of ice 1h", Journal de physique, C1-207–C1-220.

[87] Schulson, EM. (2001); "Brittle failure of ice", Engineering fracture mechanics, **68** (17-18): 1840-1843.

[88] Segurado J, LLorca J. (2004); "A new three-dimensional interface finite element to simulate fracture in composites", International journal of solids and structures, **41**: 2977–93.

[89] Shao, J. and Lister, P.J. (1996); "Real-Time road ice prediction and its improvement in accuracy through a self-learning process", Snow removal and ice control technology, Proceedings of the fourth international symposium, Reno, Nevada, August 11-16.

[90] Shvayshteyn, Z.I. (1959); "Laboratory for studying ice and testing models of icebreakers and ice-strengthened vessels", Problemi Arktiki, No. 2.

[91] Sinha, N.K., Timco, G.W., and Frederking, R. (1987); "Recent advances in ice mechanics in Canada", Applied mechanics review, **40**(9): 1214–1231.

[92] Sonwalkar, N., Sunder S. Shyam, and Sharma, S.K. (1993); "Ice/Solid adhesion analysis using low-temperature Raman microprobe shear apparatus", Applied spectroscopy, **47**(10): 1585-1593.

[93] Sundin, E., and Makkonen, L. (1998); "Ice loads on a lattice tower estimated by weather station data", Journal of applied meteorology, **37**(5): 523-529.

[94] Suo, Z., and Hutchinson, J. W. (1989); "Sandwich test specimens for measuring interface toughness", Journal of materials science and engineering, **A107**: 135–143.

[95] Swedlow, Jerold L. (1965); "On Griffith's theory of fracture", International Journal of fracture, **1**: 210–221.

[96] Tryde Per, (1979); "Physics and mechanics of ice symposium Copenhagen", Technical University of Denmark, p138.

[97] Uchida, T., and Kusumoto, S. (1999); JSME International journal series A – solid mechanics and materials, **42**: 601.

[98] Ugural, A.C. (1991); "Mechanics of materials".

[99] Wang, J.S., and Anderson, P.M. (1991); "Fracture behaviour of embrittled FCC metal bicrystals", Acta. Metall. Mater. **39**: 779-792.

[100] Weber, L.J., and Nixon, W.A. (1996); "Fracture toughness of freshwater ice - Part I: Experimental technique and results", Journal of offshore mechanics and arctic engineering, **118**: 135-140.

[101] Wei, Y., Adamson, R.M, and Dempsey, J.P. (1996); "Ice/metal interfaces: fracture energy and fractography", Journal of materials science, **31**: 943-947.

[102] Weibull, W. (1939); "A statistical theory of the strength of materials", Ingenioersvetenskapsakad, Handl, **151**: 1-45.

[103] Wu, H.C., Chang, K.J., Schwarz, J. (1976); "Fracture in the compression of columnar-grained ice", Engineering fractures mechanics, **8** (2): 365-372.

[104] Xian, X., Chu, M.L., Scavuzzo, R.J., and Srivatsan, T. S. (1989); Journal of materials science letters, **8**: 1205.

[105] Zienkiewicz, O. C. and Taylor, R. L. (1989); "The finite element method. 4th edition" McGraw-Hill, London.

APPENDIX

APPENDIX A *Calculation of strain energy release rate components*

A.1 Mixed- mode bending test

The loadings applied to bilinear components are typically resolved into interlaminar tension and shear stresses at discontinuities that create mixed-mode I, II and III delaminations. To characterize the onset and growth of these delaminations, the total strain energy release rate G_T, the mode I component due to interlaminar tension G_I, the mode II component due to interlaminar sliding shear G_{II}, and the mode III component G_{III}, due to interlaminar scissoring shear, as shown in Figure A.1, need to be calculated.

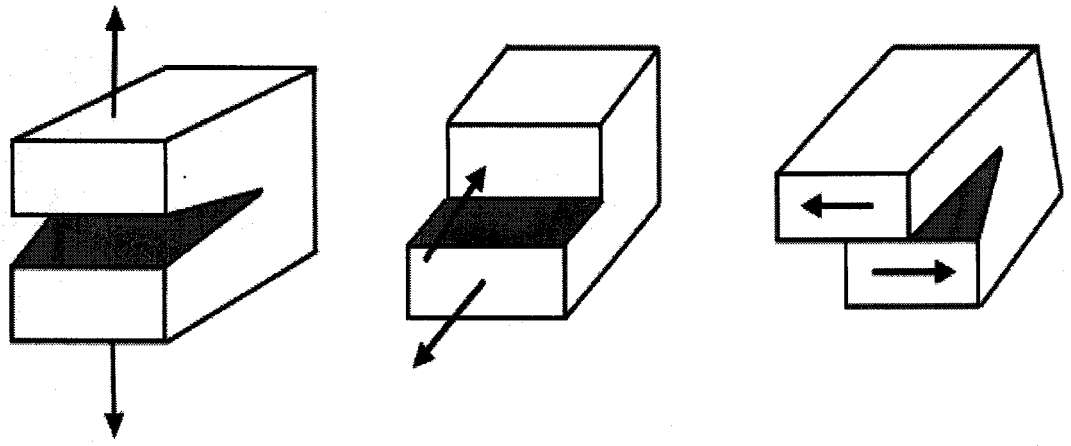

Interlaminar tension Mode I | Interlaminar sliding shear Mode II | Interlaminar scissoring shear Mode III

Figure A.1: Fracture modes.

The mixed-mode bending (MMB) test is analyzed using beam theory to calculate the mode I and mode II components of strain energy release rate, G_I and G_{II} respectively. The specimen is loaded until the delamination grows. Measured load and

delamination length can then be substituted into strain energy release rate equations to calculate the delamination toughness. The mixed-mode bending (MMB) test simply combines the mode I for a double cantilever beam (DCB) and the mode II for end notch flexure (ENF) tests. This is achieved by adding an opening-mode load to a mid-span loaded ENF specimen, as shown in Figure A.2 (a). This additional load separates the arms of the split unidirectional laminate as in a DCB test. The relative magnitudes of the two applied loads determine the mixed-mode ratio at the delamination front. By applying these two loads through a lever and hinge apparatus as shown in Figure A.2 (b), the test can be conducted by applying a single load. The loading position c determines the relative magnitude of the two resulting loads on the specimen and, therefore, determines the mixed mode delamination ratio. Pure mode II loading occurs when the applied load is directly above the beam mid-span (c = 0). Pure mode I loading can be achieved by removing the beam and pulling up on the hinge.

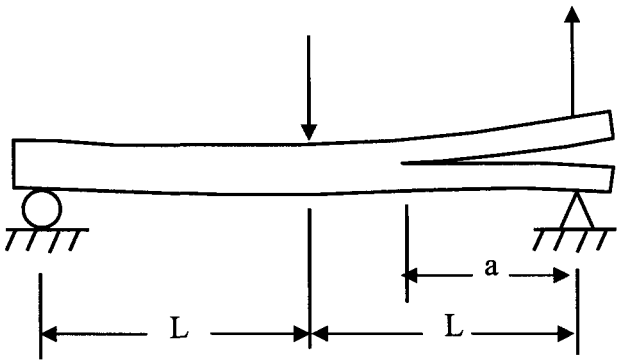

(a) Test specimen and loading.

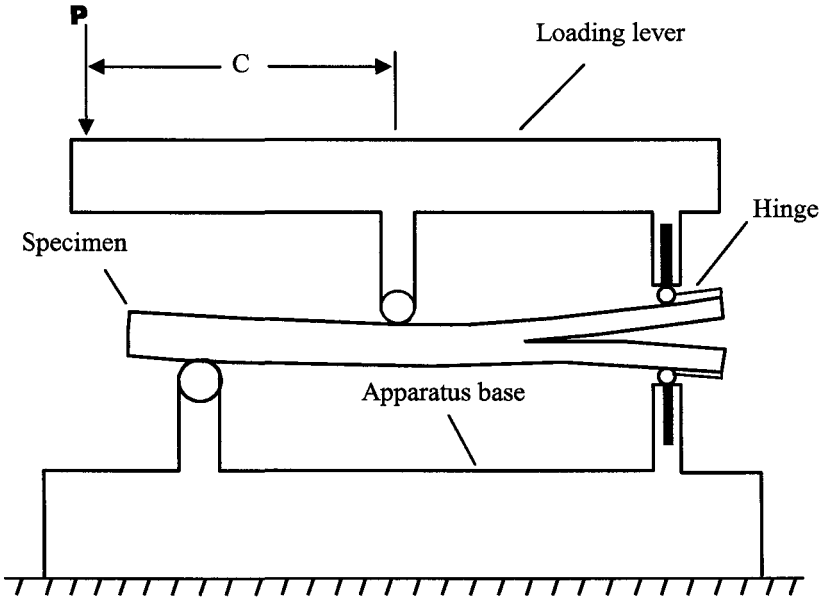

(b) Schematic diagram of apparatus.

Figure A.2: Mixed-mode bending specimen and test apparatus.

A.2 Beam Theory Analysis

This section presents strain energy release rate equations based on beam theory. The MMB loading can be represented by a superposition of simple mode I and mode II loadings, equivalent to those used with DCB and ENF tests respectively. Thus, strain energy release rate equations from the literature on DCB and ENF tests could be combined to obtain the desired equations for the MMB test. Figure A.3 (a) shows the

MMB loading expressed in terms of the applied load P, the loading lever length c, and the specimen half-span L.

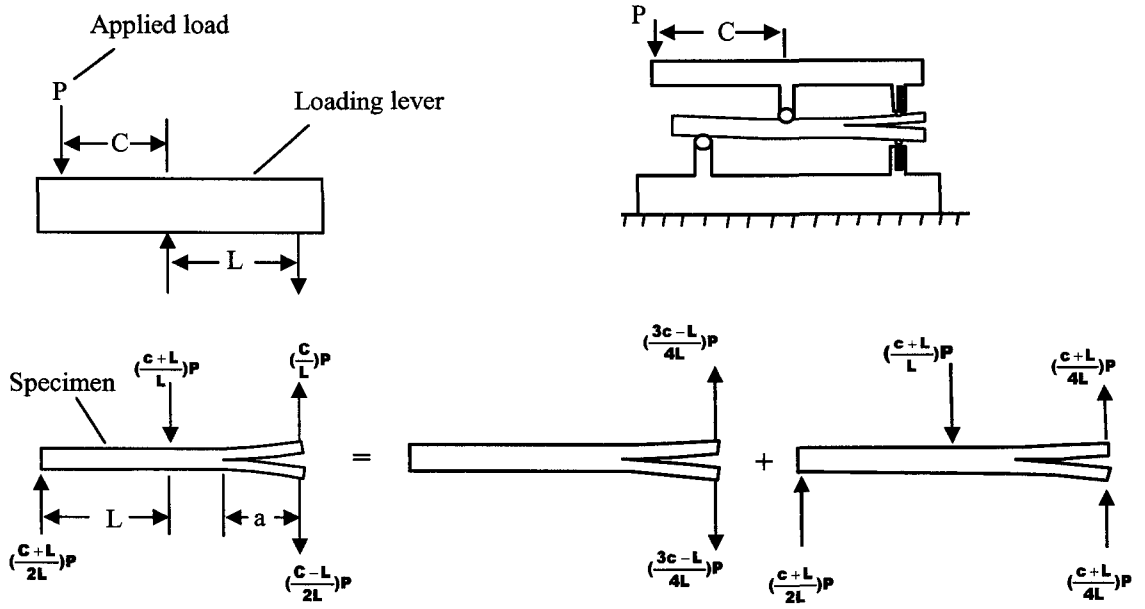

(a) MMB specimen loading. **(b) Mode I loading.** **(c) Mode II loading.**

Figure A.3: Superposition analysis of loading on MMB specimen.

As shown in figure A.3 (b), the mode I component of this loading is:

$$P_I = \left(\frac{3c - L}{4L}\right)P$$

Simple beam theory analysis of the DCB specimen leads to

$$G_I = \frac{12a^2 P_I^{\,2}}{b^2 h^3 E_{11}} \tag{A.1}$$

where b is specimen width and h is half-thickness. Substituting for P_I leads to the following equation for G_I :

$$G_I = \frac{3a^2P^2}{4b^2h^3L^2E_{11}}(3c-L)^2 \tag{A.2}$$

Figure A.3 (c) shows the mode II portion of the MMB loading. Note that the right-end loading has been divided equally between the two equal-stiffness arms of the specimen. This is equivalent to the conventional loading of the ENF test. For the ENF test, the mode II bending load as shown in Figure A.3 (c) is:

$$P_{II} = \left(\frac{c+L}{L}\right)P$$

The following equation for G_{II} of the ENF test was presented by Russell [2].

$$G_{II} = \frac{9a^2P_{II}^{\ 2}}{16b^2h^3E_{11}} \tag{A.3}$$

Substituting for P_{II}, the corresponding equation for G_{II} of the MMB test is:

$$G_{II} = \frac{9a^2P^2}{16b^2h^3L^2E_{11}}(c+L)^2 \tag{A.4}$$

By dividing Equation (A.2) by Equation (A.4), the G_I/G_{II} ratio for the MMB test can be expressed as:

$$\frac{G_I}{G_{II}} = \frac{4}{3}\left[\frac{(3c-L)}{(c+L)}\right]^2 \qquad c \geq \frac{L}{3} \tag{A.5}$$

Notice that G_I/G_{II} is only a function of load position c and half-span length L. The G_I/G_{II} ratio is zero for $c = L/3$, and Equation (A.5) is invalid for smaller c values because this model does not account for contact between the two arms of the specimen. The total strain energy release rate for the MMB test is obtained by adding Equations (A.2) and (A.4):

$$G = \frac{3a^2P^2}{16b^2h^3L^2E_{11}}\left[4(3c-L)^2 + 3(c+L)^2\right] \tag{A.6}$$

Also, an improved beam theory equation for the DCB test has been introduced by Kanninen [15]. He recognized that simple beam theory did not properly model the interaction between the two arms of the DCB specimen. The two arms are not fixed against rotation at the delamination tip as assumed in simple beam theory. Instead, they rotate slightly due to the elastic support that they provide one another. To account for this, Kanninen assumed that each arm was a beam supported by an elastic foundation. His analysis of an isotropic DCB specimen was extended to an orthotropic DCB specimen by replacing E with E_{11} and E_{22}.

$$G_I = \frac{12P_I^2}{b^2 h^3 E_{11}}\left[a^2 + \frac{2a}{\lambda} + \frac{1}{\lambda^2}\right] \tag{A.7}$$

where $\lambda = \left(\frac{3k}{bh^3 E_{11}}\right)^{\frac{1}{4}}$ and $k = \frac{2bE_{22}}{h}$.

The beam theory equations for strain energy release rate can be further improved by accounting for the shear deformation energy associated with bending. Adding the shear deformation component of strain energy release rate [16] to Equation (A.7) leads to the following modified beam theory equation for G_I in the MMB test.

$$G_I = \frac{3P^2(3c-L)^2}{4b^2 h^3 L^2 E_{11}}\left[a^2 + \frac{2a}{\lambda} + \frac{1}{\lambda^2} + \frac{h^2 E_{11}}{10G_{13}}\right] \tag{A.8}$$

Similarly, adding the shear deformation term from [17] to Equation (A.4) results in a modified beam theory equation for G_{II} in the MMB test.

$$G_{II} = \frac{9P^2(c+L)^2}{16b^2 h^3 L^2 E_{11}}\left[a^2 + \frac{0.2h^2 E_{11}}{G_{13}}\right] \tag{A.9}$$

Assuming the unidirectional specimens are transversely isotropic, the shear modulus G_{13} in these two Equations can be replaced by G_{12}.

APPENDIX *B. Measurement of the fracture energy of ice*

B.1 Introduction

Fracture mechanics assesses the resistance of a material to brittle fracture by a parameter known as fracture energy. In order to measure the fracture energy of ice, two experimental techniques have been used by Goodman and Tabor: fracture of pre-notched rectangular specimens in three- and four-point bending.

B.2 Three- and four-point bending test

The fracture toughness of ice is very low. Therefore, it is possible to use a small, inexpensive rig completely contained within a small deep freeze to measure the fracture toughness. The arrangement that was used by Goodman is shown in Figure B.1.

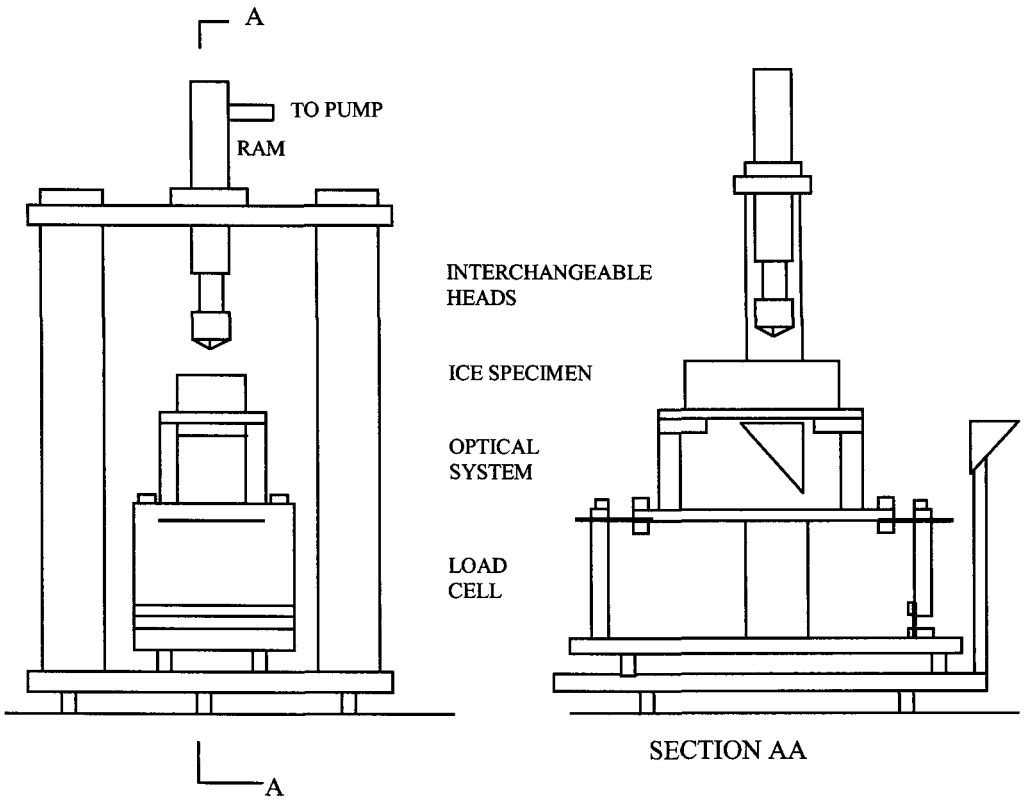

Figure B.1: The Goodman's fracture test rig set up and loading arrangement for three and four-point bending tests.

The Goodman specimens were grown in a water-filled tank inside a deep freeze (air temperature -10°C). Then the specimens from the tank were melted down to a bar shape, and, midway along one side, a slot was melted with a thin copper plate to about half the thickness of the bar. At the end of the slot a very sharp crack was formed by pushing a razor blade into the ice. The ice block is put into the small deep-freeze unit containing the loading rig and allowed to equilibrate. Oil from a hand pump is driven into the ram to force the indenter into the ice block. The ram heads can be interchanged to give various loading arrangements (three- and four-point bending, Vickers Diamond Pyramid, or other shaped indenters). The magnitude of the force is measured with a load cell beneath the ice block. The loading arrangement is shown in Figure B.2.

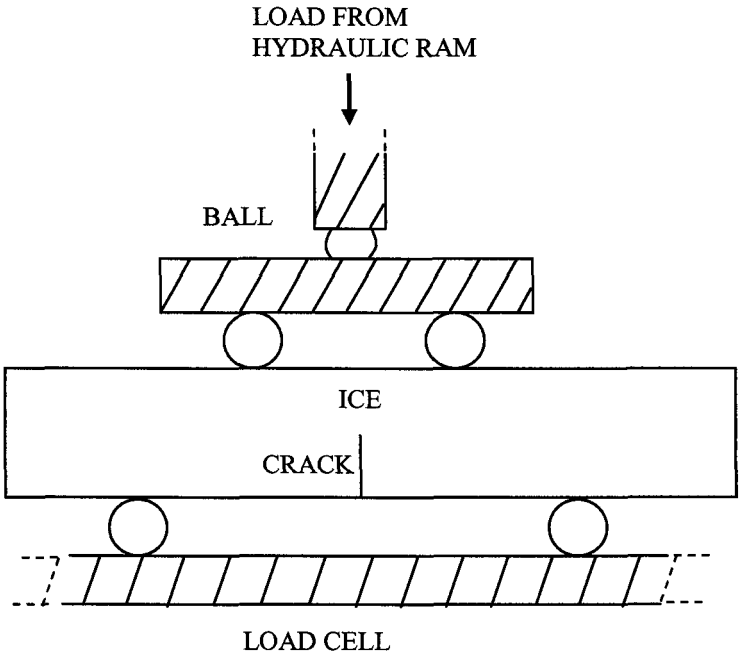

Figure B.2: The loading arrangement for the four-point bending tests. In the three-point bending test a single loading cylinder (giving line contact) is applied on the upper surface immediately above the crack.

For the case of four-point bending for a specimen with the dimensions shown in Figure B.3, and thickness b, the critical stress intensity factor K_{IC} is given by [11]:

$$K_{IC} = \frac{3P(l_1 - l_2)a^{\frac{1}{2}}}{2bh^2} \text{f(a/h)} \tag{B.1}$$

where f(a/h) is:

$$\text{f(a/h)} = 1.99 - 2.47\,(\text{a/h}) + 12.97\,(\text{a/h})^2 - 23.17\,(\text{a/h})^3 + 24.80\,(\text{a/h})^4$$

The quantities K and G are related by the expressions:

in plane stress

$$G = \frac{K_{Ic}^{\ 2}}{E}, \tag{B.2}$$

and in plane strain

$$G = K_{Ic}^{\ 2}\left(\frac{1-\upsilon^2}{E}\right) \tag{B.3}$$

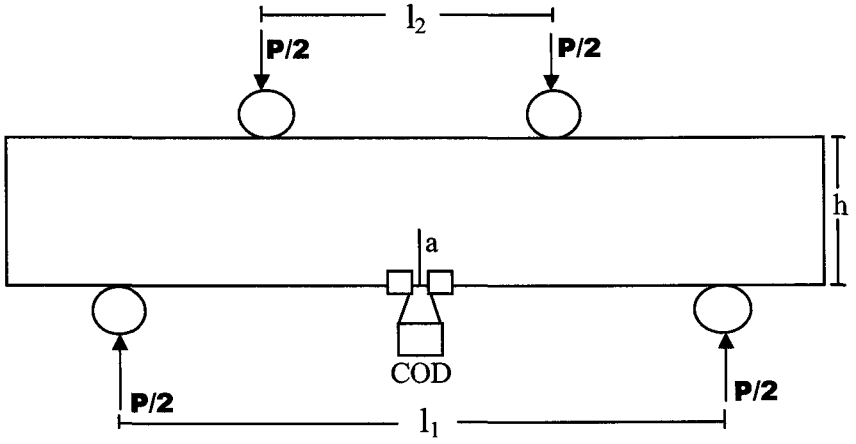

Figure B.3: The four-point bending test geometry.

APPENDIX C *Measurement of the interface fracture energy of ice*

Charalambides et al [28] developed a four-point bending delamination specimen (see Figure C.1) in order to determine the critical energy release rate at the bimaterial interface. This method has the advantage of being easy to use to simulate icing on the surface of structures on the simple sample geometry. On the base of Euler-Bernoulli beam theory, the critical interface fracture energy G_f, is [96]:

$$G_f = \frac{M_f^2(1-\upsilon_2^2)}{2E_2}\left(\frac{1}{I_2}-\frac{\lambda}{I_c}\right) \tag{C.1}$$

where

$$\lambda = \frac{E_2\left(1-\upsilon_1^2\right)}{E_1\left(1-\upsilon_2^2\right)},\quad M_f = \frac{Pl}{2b},\quad I_2 = \frac{h_2^3}{12} \tag{C.2}$$

The bending moment M_f exists along the sample cross section. And I denotes the moment of inertia, the subscripts 1 and 2 refer to the ice and substrate materials respectively, and subscript c refers to the composite beam. It should be noted that this approach is valid when the crack length must be significantly larger than the thickness of the upper layer.

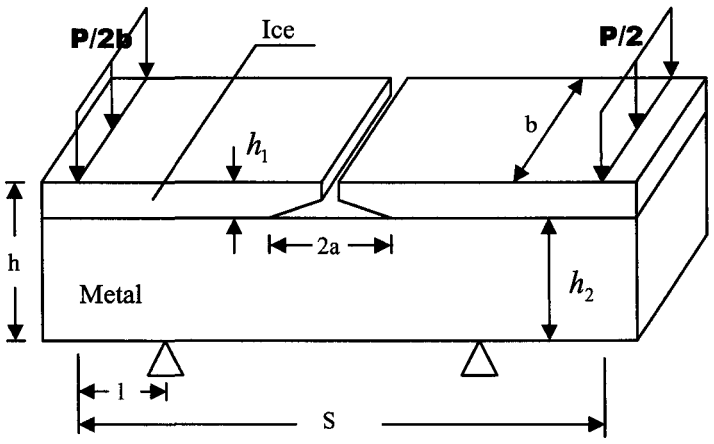

Figure C.1: Four-point bending specimen geometry and loading configuration.

APPENDIX D Experimental protocol for tensile test

D.1 Materials:

1. Strain Gauge Instrumentation, Model 3800, Wide-Range Strain Indicator, Measurements Group, #036939
2. Strain indicator, Measurements Group model P3500, #034157
3. Press ATS, Applied Test Systems, inc., 15 A, 60 Hz, A860896-6-87
4. PCB 486 G computer (program Cold room)
5. Computer, DAT 143288, #046206 (Data Acquisition)
6. Cordless drill battery DEWALT, DW953, Type 1, 12 V, #34310
7. Dewalt battery 12 V, DW9072
8. Mastercraft torque wrench #58-8655-8
9. Controller of precipitation, Gralab 645, #045255
10. Danby refrigerator, D1707 W, #06663181
11. Digital micrometer, Mitutoyo Corporation, code number 500-322, model CD-8″, #7068156
12. Room temperature with frosting precipitation
13. Demineralized water

D.2 Procedures:

- Preparation of the standard samples according to standard ASTM D638-02a (aluminium).
- Adjust the temperature of the cold room with drizzle glazing at -10° C.
- In the cold room, place the sample perfectly centered in the clips.

- Leave the aluminium plate at the selected temperature (–10 °C) in the cold room for at least 30 minutes before starting the ice-making process.
- Put the signal of the strain indicator at zero.
- Put the steel blocks (the grips) and screw each side in Z with the drilling machine and at the end with the torque wrench (to make sure that it is regulated with 200 lbf).
- Make a pre-stretching of approximately +120 $\mu\varepsilon$ H14 for aluminium plate at a low speed.
- Put in the mould before icing to permit the accumulation of ice only on the sample's surface.
- Begin precipitations using the test conditions provided in Table D.1. The precipitation time depends on the desired thickness of ice (about 25 minutes for 5 mm). Check the thickness during the precipitation.
- When the aluminium sample is covered with the desired thickness of ice, stop the precipitation and remove the 2 perforated panels (mould).
- Keep each specimen at the ice-making temperature for one hour before starting the test process.
- During this time, start the software Quicklog to store the analytical signal to a computer data file using a computer data acquisition.
- Write down the pre-stretching of each strain indicator.
- Measure the length and thickness of ice using a micrometer and note on the test sheet.
- Put the signal of the two-strain indicator to zero.

- Select the desired speed for tensile test on the extremity of the press (1 to 10) and then on the external module (L-M-H).
- When everything is ready for the test, start the acquisition by pressing the on button DOWN of the control module of the press machine by checking well on the strain indicator. Carry out the stretching up to 5000 $\mu\varepsilon$ for aluminium 2024 T3. This value should correspond to the maximum deformation of aluminium in elastic regime.
- Save the data for data analysis and to determine the stress-strain graphs.
- Take the photograph of the sample with a digital camera and write down the observations (de-icing, separation, place of the cracks, etc).

Table D.1: The experimental conditions of ice samples.

Parameters	**Units**	**Type -quantity**
Type of precipitations	___	Rain glaze
Water temperature, T_w	°C	$\cong 4$
Air temperature, T_a	°C	-10.0 ± 0.5
Type of water	___	Deionized
Jet edge	___	11001
Time of spray nozzle	sec	For opening = 0.4 For stopping = 0.9
Ventilator	Hz	40
Intensity of precipitations	mm/h	18